POLITECNICO

MILANO 1863

SCUOLA DI INGEGNERIA INDUSTRIALE
E DELL'INFORMAZIONE

Large Eddy Simulations of a Lean Premixed Swirl-stabilized Combustor

TESI DI LAUREA MAGISTRALE IN
ENERGY ENGINEERING - INGEGNERIA ENERGETICA

Author: **Giacomo Abbasciano**

Student ID: 990252
Advisor: Prof. Dr. Giacomo Bruno Azzurro Persico
Co-advisors: Prof. Dr. Ivan Langella
Academic Year: 2022-23

Abstract

Hydrogen, with its high energy density and carbon-free combustion, is a promising clean energy carrier for power generation and potential use in aeronautics. Stabilizing hydrogen flames in ultra-lean premixed conditions, exploiting its wide flammability range, can suppress nitric oxides (NO_x) formation linked to high flame temperatures via the Zel'dovich mechanism. Swirled combustors are commonly used to rapidly mix and stabilize lean premixed flames, particularly in low-velocity regions associated with the central recirculation zone. The high reactivity and diffusivity of hydrogen pose challenges such as flashback and flame instabilities. To address this, axial air injection (AAI) can be employed to increase axial momentum within the combustor, effectively controlling flame positioning and preventing flashback. In the present work, large eddy simulations (LES) with flamelets based thermochemistry and presumed probability density function (PDF) to represent the flame-turbulence interaction, are used to investigate the flow field and emissions within the swirled technically premixed laboratory combustor with AAI at TU Delft. The objective of the present work is to assess the ability of the in-house developed LES model to predict the correct flow field and pollutant emissions in the swirled flow configuration, in order to facilitate future investigation of hydrogen-enriched flames. The study is organized as follows. First, a non-reactive case with only oxidizer as working fluid is analyzed to validate the model against in-house experimental data, and to achieve further insight on the flow features and its dependence on the swirl number at the inlet of the mixing tube. The analysis is then extended to a non-reactive CH_4/air to understand how density variation affects flow features. Finally, a reactive CH_4/air is simulated to evaluate the LES closure and an innovative NO_x emission prediction method. Results show a notable agreement between the predicted and the measured flow fields for the non-reacting validation cases. Both experimental and numerical analysis reveals how fuel/oxidizer mixing plays a predominant role in flame stabilization, temperature and emissions. The inclusion of a transport equation is observed to dramatically enhance the prediction of NO_x compared to the look-up table approach. Additionally, the local equivalence ratio variations on the flame front predicted by the model are observed to influence the local temperature, acceleration pattern of the flow field, flame stabilization location

and NO_x emissions. Further understanding of these behaviours are explored from the numerical side and compared with the experimental data in the present work.

Keywords: Large Eddy Simulation, OpenFOAM, lean-premixed, swirl-stabilized combustor, low-NO_x, flamelet model.

Abstract in lingua italiana

L'idrogeno, con la sua alta densità energetica e la sua combustione priva di carbonio, è un promettente vettore di energia pulita per la generazione di energia e per un potenziale utilizzo in aeronautica. La stabilizzazione delle fiamme di idrogeno in condizioni di premiscelazione ultra magra, sfruttando il suo ampio intervallo di infiammabilità, può sopprimere la formazione di ossidi di azoto (NO_x) legata alle alte temperature di fiamma attraverso il meccanismo di Zel'dovich. I combustori con swirler sono comunemente utilizzati per miscelare rapidamente e stabilizzare le fiamme premiscelate magre, in particolare nelle regioni a bassa velocità della zona di ricircolo centrale. L'elevata reattività e diffusività dell'idrogeno pone problemi quali il flashback e altre instabilità di fiamma. Per risolvere questo problema, si può ricorrere all'iniezione assiale di aria (AAI) per aumentare la componente assiale della quantità di moto all'interno del combustore, controllando efficacemente il posizionamento della fiamma e prevenendo il ritorno di fiamma. Nel presente lavoro, Large Eddy Simulations (LES) con termochimica basata su flamelets e funzione di densità di probabilità (PDF) presunta per rappresentare l'interazione fiamma-turbolenza, sono utilizzate per studiare il campo di moto e le emissioni all'interno del combustore di laboratorio premiscelato con AAI presso TU Delft. L'obiettivo del presente lavoro è quello di valutare la capacità del modello LES, sviluppato internamente, di prevedere il campo di flusso corretto e le emissioni inquinanti nella configurazione di flusso swirlato, al fine di facilitare le future indagini sulle fiamme arricchite di idrogeno. Lo studio è organizzato come segue. In primo luogo, viene analizzato un caso non reattivo con solo ossidante come fluido di lavoro per convalidare il modello rispetto ai dati sperimentali Particle Image Velocimetry (PIV) interni e per ottenere ulteriori informazioni sulle caratteristiche del campo di moto e sulla sua dipendenza dal numero di Swirl all'ingresso del tubo di miscelazione. L'analisi viene poi estesa a un caso $CH_4/aria$ non reattivo per capire come la variazione della densità influisca sulle caratteristiche del campo di moto. Infine, viene simulato un caso $CH_4/aria$ reattivo per valutare la chiusura della LES e un innovativo metodo di previsione delle emissioni di NO_x. I risultati mostrano un notevole accordo tra i campi di moto simulati e misurati per i casi non reattivi. L'analisi sperimentale e numerica rivela come la miscelazione combustibile/ossidante giochi un ruolo predomi-

nante nella stabilizzazione della fiamma, nella temperatura e nelle emissioni. Si osserva che la risoluzione di un'equazione di trasporto migliora notevolmente la previsione di NO_x rispetto all'approccio tabulare. Inoltre, si osserva che le variazioni locali del rapporto di equivalenza sul fronte di fiamma previste dal modello influenzano la temperatura locale, il campo di accelerazione, la posizione di stabilizzazione della fiamma e le emissioni di NO_x. La comprensione di questi comportamenti viene approfondita dal punto di vista numerico e confrontata con i dati sperimentali nel presente lavoro.

Parole chiave: Large Eddy Simulation, OpenFOAM, lean-premixed, swirl-stabilized combustor, low-NO_x, flamelet model.

Contents

1 | Introduction

1.1. Relevance and challenges of hydrogen combustion

At present, aviation accounts for approximately 3% of the world's CO_2 emissions. The European Aviation industry is devoted to attaining net-zero CO_2 emissions for all flights within and leaving Europe by 2050. Hydrogen combustion is the most promising method for powering long-distance flights due to its high energy density, minimal carbon emissions, and potential for production from water electrolysis using renewable energy [1]. Nevertheless, the comparatively high flame temperature may significantly raise the production of nitric oxides (NOx). Using premixed lean-burn technology and taking advantage of hydrogen's wide range of combustibility to stabilize the flame in highly lean conditions can significantly reduce this [2, 3]. However, there are further design issues due to the high reactivity and diffusivity of hydrogen and the potential for extra instabilities in lean premixed combustion [4]. Additionally, safety precautions against flashback suggest that contemporary lean-burn gas turbine combustors function in partially premixed regimes, where potential fuel and oxidizer inhomogeneities provide additional difficulties for emissions and flame stability [5–7]. Because hydrogen is more reactive than other species, adding it to a lean-burn device would unavoidably increase flame speed and raise the risk of flashback, which is damaging for the apparatus. Moreover, the dynamic response of the flame to acoustic perturbations is greatly affected by the addition of hydrogen, as demonstrated by [8].Thus, in order to prevent unintentional flame spread, thorough research must be done before introducing hydrogen to these systems. In lean premixed swirl stabilized systems, flashback can occur through thermoacoustic instabilities, through the boundary layer of surrounding walls, or at the jet core when the flame speed exceeds the reactant speed. Flashback can also occur through a process called combustion-induced vortex breakdown (CIVB) [9]. Typical remedies for the last two routes involve either increasing the bulk air velocity or decreasing the swirl intensity.But doing so may also lead to higher pressure losses and poor mixing, which would raise emissions [7]. An approach for preventing the flame from propagating upstream is to use axial air injection, which

may be applied directly in the jet core or in the boundary layer [10, 11]. It was also discovered that this type of injection was effective in keeping NOx levels low [12]. While NOx was shown to rise considerably in this instance, other studies have experimented with axial fuel injection instead of air injection to reduce flashback [13, 14]. It is still unknown how the axial injection affects mixing and emissions despite these studies. Instabilities in mixing can also be linked to variations in heat release, and thus acceleration pattern of the flow field which can result in further instability or flashbacks.

1.2.   APPU Project

The major reduction of aviation's environmental impact is the primary objective of the EU Flight Path 2050 Goals. The negative effect of aviation on the climate needs to be addressed quickly, even though significant changes in aircraft configuration are not likely to occur until the second half of this century. By introducing energy mix into aviation and improving aircraft efficiency through the inclusion of novel boundary layer ingestion (BLI) technology to the workhorse of aviation, the A320, the APPU (Advanced Propulsion and Power Unit) project seeks to considerably decrease local air pollution while also significantly reducing the worldwide repercussions of aviation. This will substantially decrease risks and the time to market introduction. The proposed APPU is an innovative technology that substitutes the existing APU (Auxiliary Power Unit) with a multifunctional state-of-the-art gas turbine powered by hydrogen and powering a variable pitch open rotor propulsion system at the fuselage's aft end in a BLI configuration. Preliminary tests show that by combining BLI with hydrogen combustion, the CO_2 emissions for a typical 2000km trip may be decreased by roughly 20%, while the LTO (i.e. Landing and Take-Off) pollutants emissions can be cut down by around 50% [15].

Figure 1.1: APPU project poster [15].

1.3.   Contribution of this work

The objective of this study is to support the advancement of a lean hydrogen premixed swirl-stabilized combustor with axial air injection and reduced NOx and carbon emissions for the APPU project. This will be achieved by validating a reactive and non-reactive Large Eddy Simulation (LES) model. The purpose of this study is to investigate the turbulent swirling flow characteristics, temperature field, flame stabilization, and NO emissions in a laboratory-scale, swirl-stabilized combustor at TU Delft through the use of numerical simulations. The combustor is comprised of an axial swirler that releases the mixture into a mixing tube. Within this tube, fuel is introduced and blended with air prior to entering the combustion chamber. The numerical results have been supported and validated through Particle Image Velocimetry (PIV) measurements, which were performed on both reacting and non-reacting cases involving a CH_4/air mixture. The study conducts a preliminary investigation of emissions by employing an improved method for forecasting the NO concentration field [16]. This method is included into the Large Eddy Simulation model, which is paired with a reduced chemistry approach using complex thermochemistry tabulation, namely the flamelet model. The effects of smaller unresolved sub-grid scale (SGS) motion are modeled using the LES approach, which involves applying a filtering process to the Navier-Stokes equations in order to resolve only the larger scales of turbulence [17]. In contrast to Reynolds-averaged Navier Stokes (RANS) and Direct Numerical Simulations (DNS) approaches, the Large Eddy Simulation method offers the advantage of accurately predicting unsteady reacting flow characteristics while maintaining a reasonable computational expenditure. This makes LES a suitable tool for analyzing the intricate turbulent flow field, characterized by swirling and recirculation, within the combustor. Additionally, LES enables accurate prediction of the mixing process across various length scales and time scales. In the literature, a comprehensive overview of several combustion models has been presented by Vervisch [18]. These models aim to accurately simulate the complicated interactions between turbulence, diffusion, and reactions at the subgrid-scale level. In this study, the Flamelet Model (FM) is employed to represent the unresolved sub-grid scale turbulence-flame interaction. The FM incorporates a presumed beta probability density function (PDF) and utilizes a look-up table methodology, as described in previous works [19, 20]. The reduced chemistry approach of the flamelet mode is employed together with detailed chemistry schemes (GRI-Mech 3.0) to adequately account for the sub-grid scale phenomena. The Pope Criterion is employed to assess the appropriate level of mesh refinement in accordance with the LES filter employed. The objective of this study is to validate the performance of the proposed LES model coupled with the flamelet approach. Additionally, the accuracy of the implemented

emission estimation is tested and validated for a complex turbulent swirling flow, specifically within the TUDelft combustor. The findings from this investigation will serve as a foundation for future research on the effects of hydrogen addition. Regarding methane, no flashback happens during lean-burn swirling combustion, therefore no axial air injection is used when operating the apparatus. In order to verify the accuracy of the numerical model and to further enhance our understanding of the underlying properties of the cold flow within the combustor, first simulations are conducted on this combustor in both fueled and unfueled non-reacting conditions. Next, the outcomes are contrasted with the in-house Particle Image Velocimetry. Subsequently, the study is expanded to encompass the reactive full methane condition, therefore verifying the LES model by comparison with PIV data. Additionally, predicted NO emissions are compared with experimental results for validation purposes. This work is organised as follows: in chapter 2 the theoretical background on working equation set and computational approaches for turbulent combustion is introduced, providing the adopted simplifying equations. In chapter 3 the turbulence and combustion modeling is presented in order to address the closure of subgrid scale terms in the multicomponent reactive filtered Navier Stokes equations (LES approach). In chapter 4, the characterization of swirling flows and combustion instabilities is presented, giving a better insight on what is going on inside the combustion chamber. Moreover, nitrix oxides formation mechanisms are explained. Ultimately, a general introduction to hydrogen's differential diffusion and the relevance of its modeling is provided. Chapter 5 deals with the numerical details adopted to perform the LESs of this work. Finally, results are shown and discussed in chapter 6, and a recap of the conclusions with a description of the future works is offered in chapter 7.

2 | Theoretical Background

2.1. Balance equations

A material volume V(t) is a volume with mass M and always made of the same set of material points. The basic set of balance equations comprises the classical Navier-Stokes, species and energy transport equations, and can be derived by applying Reynold's transport theorem and the Divergence theorem to the conservation laws for a material volume V(t). These instantaneous local balance equations, under the assumptions of continuous and homogeneous fluid, are [21, 22]:

Mass:

$$\frac{\partial \rho}{\partial t} + div(\rho \boldsymbol{u}) = 0, \tag{2.1}$$

Momentum:

$$\frac{\partial \rho \boldsymbol{u}}{\partial t} + div(\rho \boldsymbol{u}\boldsymbol{u}) - \rho \boldsymbol{f} + \nabla p - div(\underline{\boldsymbol{\tau}}) = \boldsymbol{0}, \tag{2.2}$$

Species:

$$\frac{\partial \rho Y_k}{\partial t} + div(\rho \boldsymbol{u} Y_k) + div(\rho Y_k \boldsymbol{V_k}) = \dot{\omega}_k, \tag{2.3}$$

Energy equation (sensible enthalpy form):

$$\begin{aligned}
\frac{\partial \rho h^s}{\partial t} + div(\rho \boldsymbol{u} h^s) = \left(\frac{\partial p}{\partial t} + \boldsymbol{u} \cdot \nabla p \right) - div(\boldsymbol{q}) + \Phi + \\
+ \sum_{k=1}^{N} \rho Y_k \boldsymbol{V_k} \cdot \boldsymbol{f_k} + \sum_{k=1}^{N} h_{f,k}^0 div(\rho Y_k \boldsymbol{V_k}) - \sum_{k=1}^{N} h_{f,k}^0 \dot{\omega}_k.
\end{aligned} \tag{2.4}$$

where k=1,...,N, N is the number of species, and ρ is the density of the mixture.

In particular, in the present work, the energy equation is solved in the total enthalpy h form (i.e. sensible + formation: $h = h^s + \sum_{k=1}^{N} \Delta h_{f,k}^o Y_k$), which is expressed in equation (2.5):

$$\rho \frac{Dh}{Dt} = \frac{\partial \rho h}{\partial t} + div\left(\rho \mathbf{u} h\right) = \frac{Dp}{Dt} - div(\boldsymbol{q}) + \phi + \rho \sum_{k=1}^{N} Y_k \boldsymbol{f_k} \boldsymbol{V_k} \tag{2.5}$$

where $\frac{D}{Dt} = \frac{\partial}{\partial t} + \mathbf{u} \cdot \nabla$ is the substantial derivative.

The various formulations of the energy equation are illustrated in detail in [23].

The following list explains the terms that appear in the above-mentioned equations:

- $\boldsymbol{f}$ are the body forces per unit mass: $\boldsymbol{f} = \sum_{k=1}^{N} Y_k \boldsymbol{f_k}$.

- The stress tensor $\underline{\underline{T}}$ is divided into its isotropic and deviatoric components:
  $\underline{\underline{T}} = -p\underline{\underline{I}} + \underline{\underline{\tau}}$

  where $\underline{\underline{I}}$ is the identity tensor, p is the pressure and $\underline{\underline{\tau}}$ is the viscous stress tensor (which elements are the viscous stresses τ_{ij}), that can be expressed, assuming that the fluid is Newtonian, as follows:
  $\underline{\underline{\tau}} = 2\mu_m \underline{\underline{S}} + \left(k - \frac{2}{3}\mu_m\right) div(\boldsymbol{u})\underline{\underline{I}}$

  $\underline{\underline{S}}$ is the strain-rate tensor $\underline{\underline{S}} = \frac{1}{2}(\nabla \boldsymbol{u} + [\nabla \boldsymbol{u}]^T)$, μ_m is a suitable mixture averaged dynamic viscosity and k is the bulk viscosity. The equation of a non-reacting system's momentum also holds for multicomponent reacting mixture because chemical reactions do not create momentum. The constitutive relation for Newtonian fluids is still valid but a suitable mixture averaged viscosity μ_m is needed. This can be computed using the Wilke formula which is valid for diluted polar and non-polar gases [21]:

$$\mu_m = \sum_{k=1}^{N} \frac{X_k \mu_k}{\sum_{j=1}^{N} X_j \phi_{kj}} \tag{2.6}$$

  where $\phi_{kj} = \frac{1}{\sqrt{8}}\left(1 + \frac{M_k}{M_j}\right)^{-1/2} \left[1 + \left(\frac{\mu_k}{\mu_j}\right)^{1/2} \left(\frac{M_j}{M_k}\right)^{1/4}\right]^2$

- $\boldsymbol{V_k}$ is the diffusion velocity of the species k. It is defined as $\boldsymbol{V_k} \doteq \boldsymbol{v_k} - \boldsymbol{u}$, where $\boldsymbol{v_k}$ is the local velocity of the species k and $\boldsymbol{u}$ is the mass average local velocity of the mixture (defined as $\boldsymbol{u} \doteq \sum_{k=1}^{N} Y_k \boldsymbol{v_k}$) . A property of the diffusion velocity, that

comes from the mass conservation, is the following:

$$\sum_{k=1}^{N} Y_k \boldsymbol{V}_k = \boldsymbol{0} \tag{2.7}$$

- $\dot{\omega}_k$ is the net rate of production (or 'reaction rate') of the species k per unit of volume, that is the source term that needs to be taken into account because of the occurrence of chemical reactions, that conserve the mass but not each species. Nevertheless, the conservation of mass implies the following:

$$\dot{\omega} = \sum_{k=1}^{N} \dot{\omega}_k = 0 \tag{2.8}$$

The reaction rate of the $k-th$ species $\dot{\omega}_k$ can be expressed as:

$$\dot{\omega} = \sum_{i=1}^{L} (\nu''_{k,i} - \nu'_{k,i}) A_i T^{n_i} e^{E_i/(RT)} \prod_{j=1}^{N} [M_j]^{\nu'_{j,i}} [kg/m^3 s] \tag{2.9}$$

where L is the number of reactions that occur, paying attention that direct and reverse reactions count as two different reactions for what concerns the number L. $\nu'_{k,i}$ and $\nu''_{k,i}$ are the stoichiometric coefficient of the species k of, respectively, the reactants and the products of the reaction i. M_j is the symbol of the $j-th$ species. A_i is the pre-exponential factor of Arrhenius kinetic, and in this mass basis expression it is needed to be taken into account also the molecular weight W_k of the $k-th$ species. n_i is the global order of the $i-th$ chemical reaction, E_i is the activation energy of the $i-th$ chemical reaction.

- $\boldsymbol{q}$ is the generalized heat flux:

$$\boldsymbol{q} = -\lambda_m \nabla T + \rho \sum_{k=1}^{N} h_k(T) Y_k \boldsymbol{V}_i + RT \sum_{i=1}^{N} \sum_{j=1}^{N} \frac{X_j D_i^T}{M_i D_{ij}} (\boldsymbol{V}_i - \boldsymbol{V}_j) + \boldsymbol{q}_r \tag{2.10}$$

where $-\lambda_m \nabla T$ represents the well-known conduction heat transfer in the presence of a temperature gradient (Fourier's law). The thermal conductivity λ_m is a mixture averaged property and, as for the viscosity, it can be calculated from the thermal conductivity of pure species. Several methods can be implemented, such as the Wilke formulas and Mathur's empirical formula [24]. The second term, $\rho \sum_{k=1}^{N} h_k(T) Y_k \boldsymbol{V}_i$, is the heat transfer through mass diffusion due to the different enthalpy (i.e. total enthalpy, that is sensible plus chemical) content of the various species. The third

term, $RT \sum_{i=1}^{N} \sum_{j=1}^{N} \frac{X_j D_i^T}{M_i D_{ij}} (\boldsymbol{V}_i - \boldsymbol{V}_j)$, represent the Dufour effect, that takes into account the heat transfer due to concentration gradients. The fourth and last term, $\boldsymbol{q}_r$, is the radiative heat transfer and it is an integral function accounting for the radiation effect in all directions. It depends on the gas temperature as well as the molecular structure because the efficiency of molecular radiation absorption and emission is sensitive to the wavelength of the radiation. This last term is important for flames with heavy soot loading because, in such cases, the radiative heat loss can be so substantial that the flame temperature is significantly reduced.

- $\boldsymbol{\Phi}$ is the dissipation function and represents the dissipation of mechanical energy into heat due to viscous stresses. This term comes, together with $-p\,div(\boldsymbol{u})$ in the derivation of the energy equation, from the double dot-product between the stress tensor and the gradient of the velocity field $\underline{\underline{\boldsymbol{T}}} : \nabla \boldsymbol{u}$. Highlighting the two contributions: $\underline{\underline{\boldsymbol{T}}} : \nabla \boldsymbol{u} = -p\underline{\underline{\boldsymbol{I}}} : \nabla \boldsymbol{u} + \underline{\underline{\boldsymbol{\tau}}} : \nabla \boldsymbol{u}$, where $-p\underline{\underline{\boldsymbol{I}}} : \nabla \boldsymbol{u}$ represent the reversible work of the surface forces acting on the boundaries of the control volume V(t) and $\underline{\underline{\boldsymbol{\Phi}}} = \underline{\underline{\boldsymbol{\tau}}} : \nabla \boldsymbol{u}$ is the viscous dissipation term, or the irreversible work of the surface forces (i.e. of the viscous stresses) acting on the boundaries of the control volume V(t). The reversible work did not survive as was taken out of the energy equation by applying the local conservation of mass.

- $\sum_{k=1}^{N} h_{f,k}^0 \dot{\omega}_k$ is the heat release term due to the chemical reaction that occurs in the system. It is negative for exothermic reactions.

2.1.1. Diffusion velocities: full equations and approximations

Considering equations (2.1) and (2.3), they are N+1 balance equations, that will close the N+1 unknowns $\{\rho, Y_k\}$. One must be aware only N-1 of the N species equations are linearly independent: the mass fraction of the species not accounted for by the above system is given by the following constraint: $\sum_{k=1}^{N} Y_k = 1$. The determination of the further 3N unknown given by the components of $\boldsymbol{V}_k$ for each species has now to be addressed. There are exact methods and several approximated methods, that are briefly going to be shown [23].

The diffusion velocities $\boldsymbol{V}_k$ are obtained by solving the system [23]:

$$\nabla X_p = \sum_{k=1}^{N} \frac{X_p X_k}{D_{pk}} (\boldsymbol{V}_k - \boldsymbol{V}_p) + (Y_p - X_p)\frac{\nabla p}{p} + \sum_{k=1}^{N} \frac{X_p X_k}{\rho D_{pk}} \left(\frac{D_k^T}{Y_k} - \frac{D_p^T}{Y_p} \right) \frac{\nabla T}{T} +$$
$$+ \frac{\rho}{p} \sum_{k=1}^{N} Y_p Y_k (\boldsymbol{f}_p - \boldsymbol{f}_k) \quad \text{for } p = \{1, 2, ..., N\} \tag{2.11}$$

where $D_{pk} = D_{kp}$ is the binary mass diffusion coefficient of species p into species k and X_k is the molar fraction of species k: $X_k = Y_k W/W_k$.

The following is a description of the terms of the right-hand-side of the equation, which contributes to the ∇X_p:

- $\sum_{k=1}^{N} \dfrac{X_p X_k}{D_{pk}}(\boldsymbol{V}_k - \boldsymbol{V}_p)$ represents the difference between diffusion velocities.

- $(Y_p - X_p)\dfrac{\nabla p}{p}$ takes into account the pressure gradient term.

- $\sum_{k=1}^{N} \dfrac{X_p X_k}{\rho D_{pk}} \left(\dfrac{D_k^T}{Y_k} - \dfrac{D_p^T}{Y_p} \right) \dfrac{\nabla T}{T}$ is the contribution to the mass diffusion given by the temperature gradients, and it is called Soret diffusion.

- $\dfrac{\rho}{p} \sum_{k=1}^{N} Y_p Y_k (\boldsymbol{f}_p - \boldsymbol{f}_k)$ takes into account the difference between the body forces acting on each species.

The system provides concentration gradients in terms of diffusion velocities. The diffusion velocity $\boldsymbol{V}_k$ is given implicitly and depends on all the diffusion velocities and all the concentrations. This aspect adds complexity to the numerical solution of the balance equations, for this reason, two simplifications are common: Fick's law, for theoretical and analytical flame studies, which is an exact, though simplified, approach; and the Hirschfelder and Curtiss approximation, used in most numerical tools.

If pressure gradients are small (i.e. $\nabla p/p << 1$), volume forces are neglected (i.e. $\boldsymbol{f}_k \simeq 0$), and the Soret effect is considered to be negligible (which is not always true when dealing with combustion, however, it is often neglected for simplicity [23]), system (2.11) can be solved exactly in two cases: first if the mixture contains only two species (i.e. $N = 2$), leading to Fick's law for binary mixture; second is multispecies diffusion ($N > 2$) with all the binary diffusion coefficients are equal ($D_{jk} = D$), leading again to Fick's law.

Method 1 - Fick's law of binary diffusion ($N = 2$)

If $N = 2$, the system (2.11) reduces to a scalar equation where the unknowns are the two diffusion velocities $\boldsymbol{V}_1$ and $\boldsymbol{V}_2$:

$$\nabla X_1 = \frac{X_1 X_2}{D_1 2}(V_2 - V_1) \tag{2.12}$$

The equation (2.12) leads, through some substitutions, to Fick's Law:

$$\boldsymbol{V}_1 = -D_{12}\nabla[ln(Y_1)]$$
$$\boldsymbol{V}_2 = -D_{21}\nabla[ln(Y_2)] \tag{2.13}$$

In a binary mixture, Fick's law of ordinary diffusion states, indeed, that the diffusion mass flux of a given species, $\rho Y_k \boldsymbol{V}_k$, is proportional to its concentration gradient.

This expression is exact and, since the kinetic theory of gases allows us to state $pD \simeq const$ [21] and the constraints $Y_1 \boldsymbol{V}_1 + Y_2 \boldsymbol{V}_2 = \boldsymbol{0}$ and $Y_1 + Y_2 = 1$ imply that $D_{12} = D_{21} \doteq D$, then the species balance equation (2.3) would be simplified as follows:

$$\frac{\partial \rho Y_k}{\partial t} + div(\rho \boldsymbol{u} Y_k) + \rho D \underbrace{div(\nabla Y_k)}_{\nabla^2 Y_k} = \dot{\omega}_k \quad \text{for } k = \{1, 2\} \tag{2.14}$$

Method 2 - Multicomp. diffusion in gases ($N > 2, D_{jk} = D$)

If the mixture of gases is multicomponent (i.e. $N > 2$) and $D_{jk=D}$ then the system (2.11) reduces to:

$$X_p \boldsymbol{V_p} = X_p \sum_{k=1}^{N} X_k \boldsymbol{V}_k - D\nabla X_p \quad \text{for } p = \{1, 2, ..., N\} \tag{2.15}$$

that is an exact expression. These equations can be rearranged and, through some substitutions, it can be derived that they correspond again to Fick's law:

$$\boldsymbol{V}_p = -D\nabla[ln(Y_p)] \tag{2.16}$$

Most flame theories assume that all species have identical diffusion coefficients so that Fick's law is a common choice in theoretical flame studies. As soon as a more detailed description of transport is required (i.e. to describe complex kinetics), Fick's law can not

be used and in most codes the rigorous inversion of system (2.11) in a multispecies gas is often replaced by the Hirschfelder and Curtiss approximation, which is the best first-order approximation to the exact resolution of the system [23].

Approximated method - Hirschfelder and Curtiss approximation

The Hirschfelder and Curtiss approximation consists of the following expression:

$$\boldsymbol{V}_k X_k = -D_k \nabla X_k \quad \text{with } D_k = \frac{1 - Y_k}{\sum_{j \neq k} X_j / D_{jk}} \tag{2.17}$$

The coefficient D_k is not a binary diffusion but an equivalent diffusion coefficient of species k into the rest of the mixture. This approximation leads to simplify the species' equation (2.3) as follows:

$$\frac{\partial \rho Y_k}{\partial t} + div(\rho \boldsymbol{u} Y_k) = div\left(\rho D \frac{W_k}{W} \nabla X_k\right) + \dot{\omega}_k \tag{2.18}$$

where W is the average molar mass of the local mixture.

The Hirschfelder and Curtiss approximation does not ensure mass conservation, and a correction velocity is therefore required to correct for this, as further explained in [23].

2.1.2. Simplifying assumptions of the balance equations

With regard to non-reacting problems, combustion adds complexity because species react and their rate of reaction $\dot{\omega}_k$ must be modeled, species and heat coefficients change within the solution, and transport coefficients are species-dependent. This complexity necessitates a number of simplifying assumptions. [19]. In this section the simplifying assumptions that are going to be used in this work, and their effect on the governing equations, are shown [18, 19, 23]:

- For subsonic flow the Φ term can be neglected, being the dissipation function much smaller than the heat release

- $\boldsymbol{q}_r$ is generally neglected, although it is relevant for certain applications with sooty flames.

- $\boldsymbol{f}_k$ are generally neglected

- Dofour effect and Soret effect are generally not taken into account, the former is in fact typically negligible in most combustion problems whereas the latter is typically neglected for simplicity.

- In low-speed subsonic flow (deflagrations) the low Mach approximation can be made ($Ma << 1$): this implies that $\nabla p \simeq 0$ hence both the momentum and energy equation result to be simplified. In comparison to their compressible counterparts, LES, DNS, and RANS simulations can use greater time steps thanks to this approximation. As a result, more complex kinetics can be used, which can improve predictions of the flame and its interactions with turbulence. On the other hand, in exchange, the acoustics are ignored. The interest in this work is for deflagration flames, where the pressure is nearly constant throughout the flame and the speed of the flame front s_L (i.e., the speed with which it advances into the reactants field) is substantially slower than the speed of sound. In the energy equation, but not the momentum equation, the effects of pressure variations can therefore be disregarded. Despite the low Mach number, the density is not constant because of the strong heat release across the flame: low Mach approximation eliminates the dependency of density on pressure $\rho(T, p, \boldsymbol{X}) = \rho(T, \boldsymbol{X})$. This means that a non-reactive mono-component case will result to be incompressible.

- The diffusion velocities can be modeled using the Hirschfelder approximation, thus one can write $\boldsymbol{V}_k X_k = -D_k \nabla X_k$, where D_k is related to the thermal diffusivity D_{th} through the Lewis number of species k: $Le_k D_k = D_{th}$ where D_{th} is the thermal diffusivity defined as $D_{th} = \dfrac{\lambda_m}{\rho c_p}$, c_p is the averaged specific heat at a constant pressure of the mixture ($c_p = \sum_{k=1}^{N} c_{p,k} Y_k$).

- The assumption of $Le_k = 1$ for all the $k - th$ species is generally made to simplify turbulent flame modeling, especially in premixed flames when species mass fractions and temperature are assumed to be equivalent variables. Nevertheless, thermo-diffusive instabilities occur in premixed systems when the Lewis number is lower than unity (e.g. for hydrogen). One direct consequence of these instabilities is an increase in the premixed flame area and in the reaction rate [18].

- The fluid mixture is considered to be Newtonian, with zero bulk viscosity [22], that allows to express $\underline{\underline{\boldsymbol{\tau}}}$ as:

$$\underline{\underline{\boldsymbol{\tau}}} = 2\mu_m \left(\underline{\underline{\boldsymbol{S}}} - \frac{1}{3} div(\boldsymbol{u}) \underline{\underline{\boldsymbol{I}}} \right).$$

- It is assumed the validity of the equation of state of the ideal gas, since the temperatures with which the combustion deals are much higher than double the critical temperature of the mixture of reactants and products.

- absence of external heat sources.

2.1.3. Working equation set

The set of balance equations, under the above-mentioned simplifying assumptions, become:

Mass:

$$\frac{\partial \rho}{\partial t} + div(\rho \boldsymbol{u}) = 0, \tag{2.19}$$

Momentum:

$$\frac{\partial \rho \boldsymbol{u}}{\partial t} + div(\rho \boldsymbol{u}\boldsymbol{u}) + \nabla(p) - div(\underline{\underline{\tau}}) = \boldsymbol{0}, \tag{2.20}$$

Species:

$$\underbrace{\frac{\partial \rho Y_k}{\partial t}}_{\text{accumulation}} + div \left(\underbrace{\rho \boldsymbol{u} Y_k}_{\text{avvection}} + \underbrace{\rho \boldsymbol{V_k} Y_k}_{\text{diffusion}} \right) = \underbrace{\dot{\omega}_k}_{\text{source term}}, \tag{2.21}$$

Energy equation (sensible enthalpy form):

$$\underbrace{\frac{\partial \rho h^s}{\partial t}}_{\text{accumulation}} + div(\underbrace{\rho \boldsymbol{u} h^s}_{\text{avvection}} \underbrace{- \lambda_m \nabla T + \rho \sum_{k=1}^{N} h_k^s Y_k \boldsymbol{V_k}}_{\text{diffusion}}) = \underbrace{- \sum_{k=1}^{N} h_{f,k}^0 \dot{\omega}_k}_{\text{source term}}. \tag{2.22}$$

Equation of state:

$$p = \rho R T \sum_{k=1}^{N} Y_k W_k \tag{2.23}$$

where $R = 8.3145[kJ/kmolK]$ is the universal gas constant and $W = \sum_{k=1}^{N} X_k W_k = \frac{Y_k}{W_k}$ is the molecular weight of the mixture. It can further be derived that $Le_k = 1$ would simplify the energy equation together with assumptions of Fick's law and $D_{ij} = D$:

$$\underbrace{\frac{\partial \rho h^s}{\partial t}}_{\text{accumulation}} + div(\underbrace{\rho h^s \boldsymbol{u}}_{\text{avvection}} \underbrace{- \rho D \nabla h^s}_{\text{diffusion}}) = \underbrace{- \sum_{k=1}^{N} h_{f,k}^0 \dot{\omega}_k}_{\text{source term}} \tag{2.24}$$

An analogous simplification can be derived using the Hirschfelder and Curtiss approximation together with the correction velocity, in order to respect the conservation of mass [19].

The simplification of the energy equation (2.5) in the form of total enthalpy h is analogous.

2.2.   Interaction between flames and turbulence

The laminar flame mode is replaced by a regime where turbulence and combustion interact when flow entering a flame front is turbulent. The principal issues with turbulent combustion include [23]:

- There are numerous temporal and length scales involved in turbulent combustion. This complexity eventually leads to a classification of various regimes that result from an effort to describe the flame's behavior (see Borghi diagram). The structure and description of turbulence, which is the most complex phenomenon in non-reacting fluid mechanics, are still up for debate.

- Even for the burning of simple hydrocarbons, a detailed account of chemical mechanisms in laminar flames may necessitate hundreds of species and thousands of reactions, creating significant numerical challenges (e.g. stiffness of the reaction rate, coming from high difference in rate of reactions between species; very high number of (species) transport equations to solve, etc.). (e.g. stiffness when dealing with the reaction rate [23]).

- The two-way interaction of chemistry and turbulence leads to turbulent combustion. Due to the significant flow accelerations caused by heat release through the flame front and the significant changes in kinematic viscosity brought on by temperature changes, turbulence is altered by combustion when a flame interacts with a turbulent flow. "Flame-generated turbulence" is one type of turbulence that can be produced by this mechanism. "Relaminarization brought on by combustion" is another. On the other hand, turbulence modifies the structure of the flame, which can either improve the chemical reaction or, in rare circumstances (e.g. flame quenching), entirely stop it.

2.2.1.   Elementary description of turbulence

In order to understand what turbulence is and how it works, this subsection provides a basic description of the phenomenon [23].

Turbulence may be characterized by fluctuations of all local properties, and occurs for sufficiently large Reynolds numbers, depending on the system geometry. Any property f is split into mean, $\overline{f}$, and fluctuating, f', contributions:

$$f = \overline{f} + f'$$

(2.25)

The averaging process is usually defined as an ensemble average (i.e. average of a large number of realizations at the same instant of the same flow field). For steady mean flow fields, this average is replaced by time averages over a sufficiently long period t:

$\overline{f} = \frac{1}{t} \int_0^t f(t') dt'$.

The root mean square of the fluctuations f' and the mean value $\overline{f}$ are used to calculate the turbulence intensity I, which is used to describe the turbulence strength: $\overline{f}$: $I = \sqrt{\overline{f'^2}}/\overline{f}$. In a turbulent flow, for instance, the local velocity could differ by tens of percent from the temporal mean value.

Turbulent combustion, however, cannot be fully described by turbulence intensity. How the turbulence energy is distributed among the various length scales in the flow field and which length scales have sufficient energy to interact with the flame front are significant matters. Turbulent fluctuations are associated with different scales ranging from the largest, the integral length scale l_t, to the smallest one, the Kolmogorov length scale η_k. The former is usually close to the characteristic size of the flow.

A Reynolds number of the generical turbulent length scale r, $Re(r)$, is defined for each length scale [23]:

$$Re(r) \doteq \frac{u'(r)r}{\nu} \tag{2.26}$$

where $u'(r)$ is the characteristic velocity of the motion of size r and ν is the flow kinematic viscosity. The literature can simply be consulted for more complex formulations.

The Kolmogorov cascade is how the energy of the large scales moves to the smaller scales in homogeneous isotropic turbulence. The energy flux from one scale to another (caused by non-linear terms $u_i u_j$ of the N-S equations) is constant along scales and is given by the dissipation ϵ of the kinetic energy k. This dissipation ϵ is estimated as the ratio of the kinetic energy of an eddy of size r, $k = u'^2(r)$, divided by the characteristic time scale of an eddy of size r, $r/u'(r)$:

$$\epsilon = \frac{u'^2(r)}{r/u'(r)} = \frac{u'(r)^3}{r} \tag{2.27}$$

Along the cascade, $Re(r)$ decreases from $Re(r = l_t) \doteq Re_t$ to values near unity $Re(r = \eta_k) \doteq Re_k$ where inertia and viscous forces are balanced. The Kolmogorov scale η_k, which is governed by viscosity and the kinetic energy dissipation rate ϵ of the turbulent flow, is determined by this limit. The integral and Kolmogorov scale can be roughly estimated as follows:

$$\frac{l_t}{\eta_k} = \frac{u'^3/\epsilon}{(\nu^3/\epsilon)^{1/4}} = Re_t^{3/4} \tag{2.28}$$

where $\eta_k = (\nu^3/\epsilon)^{1/4}$ can be derived forcing $Re_k = 1$.

Assumptions and approximations that are going to be made are that turbulence is supposed to behave everywhere like isotropic homogeneous turbulence. In addition, turbulence is characterized through its rms velocity u' (and v', w') and its integral scale l_t.

2.3. Computational approaches for turbulent combustion

There are three levels of computation that can be used to describe turbulent combustion processes using computational fluid dynamics (CFD) [23]:

- The instantaneous flow field in a turbulent flame cannot be calculated, hence Reynolds Averaged Navier Stokes (or RANS) simulations have historically been the first method. For all quantities, RANS equations provide a solution for their temporal means. By averaging the balance equations, one can get the balance equations for Reynolds or Favre (i.e., mass-weighted) temporal-averaged values. Closure rules are needed for the averaged equations, which call for the use of a turbulence model to handle flow dynamics (i.e., to "close" the Reynolds stress tensor) and a turbulent combustion model for describing chemical species conversion and heat release (i.e. to "close" the reaction rate).

- Large Eddy Simulations (LES) correspond to the second level. While the effects of the smallest scales are modeled using subgrid closure rules, the turbulent large scales are explicitly calculated. The balance equations for LES are derived by filtering the balance equations, which is equivalent to applying a low pass filter to them, as it will be further detailed later. This allows for the varying "treatments" that different length scales receive. LES calculates the instantaneous position of a large scale resolved flame front, yet a subgrid model is still needed to account for the impact of small turbulent scales (i.e. sub-grid scales) on combustion. Note that in the case of turbulent combustion, the flame is always a subgrid phenomenon since its thickness is always smaller than the minimum size of the mesh. With the current computational power, a finer grid would need an excessive amount of time for the simulation to produce useful findings. Thus, only low-frequency variations of the quantities (e.g. temperature) would be captured by LES.

- The full balance equations are solved in Direct Numerical Simulations (DNS), the third level of combustion simulations, without the use of any model for turbulent motions. All turbulence scales are explicitly calculated, and their impact on com-

bustion is captured. The temperature would be predicted by DNS in the same way that it would be measured experimentally by a high-resolution sensor.

By construction, LES is expected to tend toward DNS when the cut-off length scale (i.e. the LES filter size) goes to zero. For what concerns RANS, only mean flow fields are resolved: no turbulent motion is explicitly captured.

Figure 2.1, taken from [23], shows a comparison of what the time-evolution of a resolved quantity looks like, with the three above-mentioned approaches:
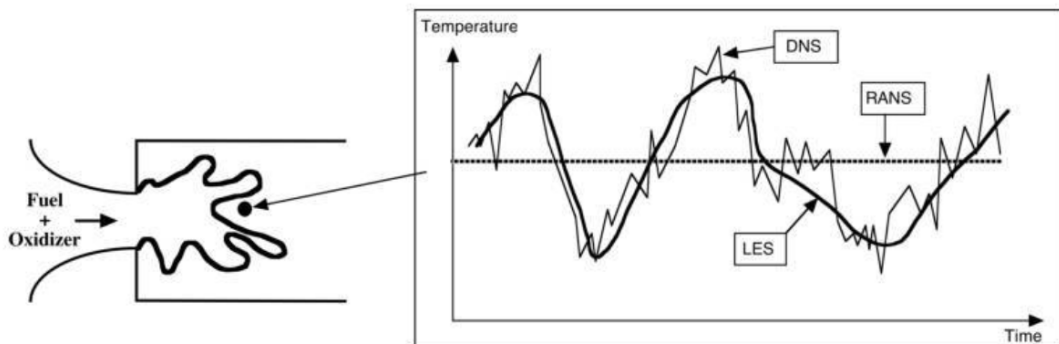
Figure 2.1: Time evolutions of local temperature computed with RANS, LES, DNS in a turbulent flame brush.

2.3.1. Comparison between RANS, LES, and DNS

The most computationally demanding method is DNS, which can only be used with reduced geometries and very low Reynolds values because of the enormous computer power and fine grids needed. LES can be used to deal with greater Reynolds numbers and can work with coarser grids (only larger scales need to be resolved), but it calls for subgrid-scale models. These physical subgrid models have a direct impact on the computation quality and the accuracy of the outcomes. RANS is widely employed in modern engineering practice because it is less resource-intensive, but its validity is constrained by the closure models defining turbulence and combustion.

Because DNS must resolve the inner instantaneous structure of the flame front and describe the smallest scales contained in the flow field, it requires a very different grid size than RANS. The fronts of hydrocarbon/air flames have a thickness on the order of 0.1 mm, necessitating the use of a mesh with a size of the order of microns for DNS. In opposition, RANS codes never resolve the inner structure of the flame and provide average flowfields with scales that are much larger than the instantaneous flame thickness. Hence, RANS consider an average flame front that extends over a larger region. Only mean turbulence characteristics and average statistical position of the front are resolved by RANS

codes. Because of the modest gradients, the mesh can be relatively coarse for RANS. In contrast, for LES, a fine grid and a non-dissipative numerical approach are required to capture the small motions. A typical LES computation can cost somewhere between 100 and 1000 times more than a RANS computation.

In this thesis, the LES approach is utilized because DNS has unaffordable computing cost and RANS has a low accuracy. LES is far more accurate than RANS, but still uses a lot less computing power than a DNS technique, which takes a lot of processing power. In fact, compared to the averaged field provided by the RANS code, the instantaneous flame surface derived with LES has significantly more turbulent scales. LES field exhibits much more unsteady structures: in terms of physics, the LES captures more turbulent activity, which is essential to recognize the formation of turbulent structures such as Vortex Breakdown, Precessing Vortex Core, and recirculation zones, that are of the utmost importance for the stabilization and for enhancing the emissions of a flame. Most reacting flows, indeed, exhibit large-scale coherent structures, that are also linked to when combustion instabilities occur (e.g. PVC). The interaction of the hydrodynamic flow field, acoustic waves, and heat release is what causes these instabilities. LES has shown to be an effective method for making low-computational cost predictions about the development of these instabilities.

2.3.2.   RANS - Reynolds-Averaged Navier Stokes equations

The instantaneous balancing equations can only be fully numerically solved (i.e., DNS) in extremely simple circumstances when there aren't a lot of different time and length scales present in the flow. In order to solve this challenge, a further step is added by averaging the balance equations to only describe the mean flow field (local fluctuations and turbulent structures are integrated in mean quantities and these structures no longer require to be described in the simulation).

Reynolds-averaging

Each quantity f is split into a mean $\overline{f}$ and a deviation from the mean denoted by f':

$$f = \overline{f} + f' \quad \text{with } \overline{f} \doteq \frac{1}{t}\int_0^t f(t')dt' \text{ and } \overline{f'} = 0 \tag{2.29}$$

Then, the previous working set of equations (2.19), (2.20), (2.21), (2.22), may be averaged this way to derive transport equations for the mean quantity $\overline{f}$. This technique, called Reynolds averaging [18], is widely used in non-reacting fluid mechanics and leads to

unclosed correlations such as $\overline{\boldsymbol{u}'f'}$ that are unknown and must be modeled. Averaging the mass balance equation (2.19) leads to:

$$\frac{\partial \overline{\rho}}{\partial t} + div(\overline{\rho \boldsymbol{u}}) = \frac{\partial \overline{\rho}}{\partial t} + div(\overline{\rho}\,\overline{\boldsymbol{u}} + \overline{\rho'\boldsymbol{u}'}) = 0 \tag{2.30}$$

Similarly, the momentum, species and energy balance equations can be derived.

Favre-averaging

Because of the thermal heat release, density fluctuations are observed in turbulent flames, and Reynolds averaging causes some additional problems (i.e. the appearance of $\overline{\rho}'\boldsymbol{u}'$ terms). To avoid the explicit modeling of such correlations, a Favre (i.e. mass-weighted) average $\tilde{f}$ is introduced and any quantity is then decomposed into:

$$f = \tilde{f} + f'' \quad \text{with } \tilde{f} \doteq \frac{\overline{\rho f}}{\overline{\rho}} \text{ and } \widetilde{f''} = \widetilde{f - \tilde{f}} = \frac{\overline{\rho(f - \tilde{f})}}{\overline{\rho}} = 0 \tag{2.31}$$

where $\overline{f}$ is the Reynolds-averaging. Thus, for flows with constant density, the Favre averaged mass, momentum, species, and energy equations are formally equivalent to the Reynolds averaged equations. However, Favre averaging is only a mathematical formalism because there isn't a simple relationship between $\tilde{f}$ and $\overline{f}$ (a relationship like this would require knowledge of the correlations between density fluctuations $\overline{\rho'f'}$, which remains hidden in Favre averaging: $\overline{\rho}\tilde{f} = \overline{\rho}\overline{f} + \overline{\rho'f'}$). Due to the fact that most experimental approaches produce Reynolds averaged data $\overline{f}$, comparisons between numerical simulations providing averaged quantities $\tilde{f}$ and experimental results are not straightforward and differences between $\tilde{f}$ and $\overline{f}$ may be significant.

Favre-averaged balance equations

The averaged equations can be derived, as in [23], Favre-averaging the working equation set (2.19), (2.20), (2.21), (2.22), and (2.23):

Mass

$$\frac{\partial \overline{\rho}}{\partial t} + div(\overline{\rho}\tilde{\boldsymbol{u}}) = 0 \tag{2.32}$$

Momentum

$$\frac{\partial \overline{\rho}\tilde{\boldsymbol{u}}}{\partial t} + div(\overline{\rho}\tilde{\boldsymbol{u}}\tilde{\boldsymbol{u}}) + \nabla\overline{p} - div(\underline{\overline{\boldsymbol{\tau}}} - \overline{\rho}\underbrace{\widetilde{\boldsymbol{u}''\boldsymbol{u}''}}_{(1)}) = 0 \tag{2.33}$$

Species

$$\frac{\partial \overline{\rho} \tilde{Y}_k}{\partial t} + div(\overline{\rho} \tilde{\boldsymbol{u}} \tilde{Y}_k) + div(\underbrace{\overline{\rho \boldsymbol{V}_k Y_k}}_{(2)} + \overline{\rho} \underbrace{\widetilde{\boldsymbol{u}'' Y_k''}}_{(3)}) = \underbrace{\overline{\dot{\omega}_k}}_{(4)} \tag{2.34}$$

Energy equation (sensible enthalpy form):

$$\frac{\partial \overline{\rho} \tilde{h}_s}{\partial t} + div(\overline{\rho} \tilde{\boldsymbol{u}} \tilde{h}_s) = \underbrace{\overline{\dot{\omega}_T}}_{\simeq(4)} + div(\underbrace{\overline{\lambda_m \nabla T}}_{(5)} - \overline{\rho} \underbrace{\widetilde{\boldsymbol{u}'' h_s''}}_{(6)}) - div \left(\underbrace{\overline{\rho \sum_{k=1}^{N} \boldsymbol{V}_k Y_k h_k^s}}_{(7)} \right) \tag{2.35}$$

where $\dot{\omega}_T \doteq -\sum_{k=1}^{N} h_{f,k}^0 \dot{\omega}_k$, hence $\overline{\dot{\omega}_T} \doteq -\sum_{k=1}^{N} h_{f,k}^0 \overline{\dot{\omega}_k}$

Equation of state

$$\overline{p} = \frac{\overline{\rho} R \tilde{T}}{\tilde{W}} \tag{2.36}$$

In RANS, operating the time-averaging leads to additional unclosed terms that need to be modeled. The objective of turbulent combustion modeling is to propose closures for the unknown quantities appearing in the averaged balance equations, that are enumerated in the equations (2.32) (2.33) (2.34) (2.35), such as:

- Reynolds stresses $\left(\widetilde{u_i'' u_j''} \right)$ (1). The turbulence model provides an approximation for this term. The closure may be done directly or by deriving balance equations for these Reynolds stresses (e.g. Zero-equation model, One-equation model, the two-equation $k - \epsilon$ model rewritten in terms of Favre averaging These models could be easily retrieved from literature [25]). However, the majority of combustion works rely on turbulence modeling created for non-reacting flows, such as $k - \epsilon$ which is simply rewritten in terms of Favre-averaging, and heat release effects on the Reynolds stresses are typically not explicitly included.

- Species $(\widetilde{u_j'' Y_k})$ (3) and enthalpy $(\widetilde{u_j'' h_s''})$ (6) turbulent fluxes. These fluxes are usually closed using a classical gradient transport assumption [19]:

$$\overline{\rho \widetilde{u_i'' Y_k''}} = -\frac{\nu_T}{Sc_{k,t}} \frac{\partial \tilde{Y}_k}{\partial x_i}, \tag{2.37}$$

where $Sc_{k,t}$ is a turbulent Schmidt number for species k and ν_T is the turbulent viscosity (subgrid scale viscosity) calculated with the selected turbulence model. Nonetheless, theory and experiments have demonstrated that in some turbulent

premixed flames, the gradient assumption is incorrect: counter-gradient turbulent transport [26] (i.e., in the opposite direction from that predicted by the equation (2.37)) can be recognized.

- Species $\left(\overline{\rho \boldsymbol{V_k} Y_k}\right)$ (2) and enthalpy $\left(\overline{\rho \sum_{k=1}^{N} \boldsymbol{V}_k Y_k h_k^s}\right)$ (7) laminar diffusive fluxes. Assuming a sufficiently high turbulence level (i.e. high Reynolds number), these molecular terms are typically ignored against turbulent transport. These terms may also be kept by adding a laminar diffusivity to the turbulent viscosity ν_T of equation (2.37). For example, species laminar diffusion fluxes could also be modeled with the gradient assumption:

$$\overline{\rho \boldsymbol{V}_{k,i} Y_k} = -\overline{\rho D_k \frac{\partial Y_k}{\partial x_i}} \simeq -\overline{\rho}\, \overline{D}_k \frac{\partial \tilde{Y}_k}{\partial x_i} \tag{2.38}$$

where $i = \{1, 2, 3\}$ are the three spatial directions; $\overline{D}_k$ is, again, a mean species molecular diffusion coefficient. Also the laminar heat diffusion flux (5) in the energy equation (2.35) is generally rewritten as:

$$\overline{\lambda_m \frac{\partial T}{\partial x_i}} = \overline{\lambda}_m \frac{\partial \tilde{T}}{\partial x_i} \tag{2.39}$$

where λ_m is, again, a mean thermal diffusivity.

- Species chemical reaction rates $\overline{\dot{\omega}_k}$ (4). Turbulent combustion modeling focuses on the closure of these mean burning rates.

2.3.3. LES - Large Eddy Simulation

Large Eddy Simulation (LES) aims to explicitly compute the largest flow structures (i.e. structures larger than the computational mesh size), while modeling the effects of the smaller ones. Although models are required for the complex coupling between micromixing and chemical reactions occurring at unresolved scales, LES has some appealing characteristics. In turbulent flows, big structures are typically governed by the system's geometry. Smaller scales, on the other hand, have more common characteristics. In light of this, turbulence models might be more effective when they are only required to explain the smallest structures. Furthermore, the majority of the global flame properties are controlled by turbulent mixing. Instead of averaging, LES simulates unsteady large-scale mixing (between fuel and oxidizer in non-premixed burners or among fresh and burnt gases in premixed flames). Additionally, most reacting flows show large-scale coherent structures

[27], which are particularly noticeable when combustion instabilities take place. These instabilities are the result of the interaction between acoustic waves, heat release, and the hydrodynamic flow field. They should be avoided because they cause large heat transfers, noise variations of the system's main properties, and in some extreme cases, the device's destruction. To predict the onset of these instabilities and subsequently enhance passive or active control systems, LES may be a potent tool [28].

Reynolds-filtering

In LES, relevant quantities f are either filtered in the physical space (weighted averaging in a certain volume) or in the spectral space (components greater than a given cut-off frequency are suppressed, which is the effect of applying the low pass filter mathematical operator to the instantaneous equations). The (Reynolds) filtering operation is defined as [18]:

$$\overline{f}(\boldsymbol{x}) = \int f(\boldsymbol{x}^*)F(\boldsymbol{x} - \boldsymbol{x}^*)d\boldsymbol{x}^* \tag{2.40}$$

where F is the LES filter.

The usual LES filters are:

- A cut-off filter in the spectral space:

$$\overline{F}(k) = \begin{cases} 1 & \text{if } k \leq \pi/\Delta \\ 0 & \text{otherwise} \end{cases} \tag{2.41}$$

  where k represents a frequency. This filter preserves the length scales greater than the cut-off length scale 2Δ and suppresses all the length scales smaller than the cut-off length scale 2Δ.

- A box filter in the physical space:

$$F(\boldsymbol{x}) = F(x_1, x_2, x_3) = \begin{cases} 1/\Delta^3 & \text{if } |x_i| \leq \Delta/2, i = 1, 2, 3 \\ 0 & \text{otherwise} \end{cases} \tag{2.42}$$

  where (x_1, x_2, x_3) are the spatial coordinates of the location $\boldsymbol{x}$. This filter corresponds to an averaging of the quantity f over a box (volume) of size Δ.

- A Gaussian filter in the physical space:

$$F(\boldsymbol{x}) = F(x_1, x_2, x_3) = \left(\frac{6}{\pi\Delta^2}\right)^{3/2} exp\left[-\frac{6}{\Delta^2}(x_1^2 + x_2^2 + x_3^2)\right] \tag{2.43}$$

All these filters are normalized:

$$\int_{-\infty}^{+\infty} \int_{-\infty}^{+\infty} \int_{-\infty}^{+\infty} F(x_1, x_2, x_3)dx_1 dx_2 dx_3 = 1 \tag{2.44}$$

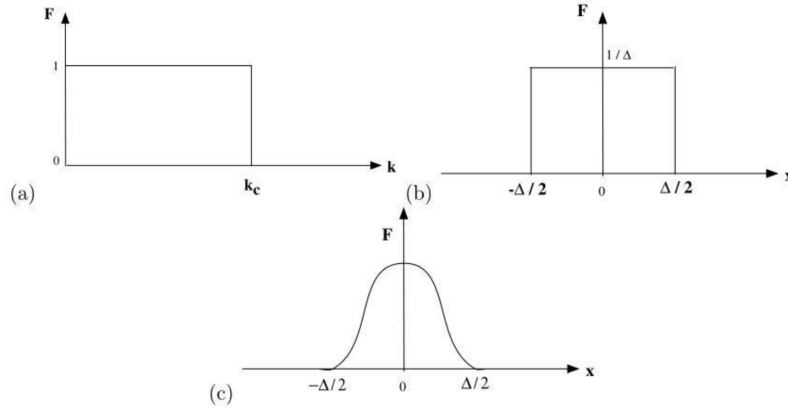The following figure 2.2, taken from [23], shows the above-mentioned filters:

Figure 2.2: Common spatial filters used in large eddy simulations. (a) cut-off filter in spectral space; (b) box filter in physical space; (c) Gaussian filter in physical space.

where $\overline{f}$ is the Reynolds-filtering.

Favre-filtering

In combustion, the mass-weighted Favre-filtering is used instead of the Reynolds-filtering because of the varying density due to the heat release (the reason is analogous to Favre-averaging in RANS instead of Reynolds-averaging):

$$\overline{\rho}\tilde{f}(\boldsymbol{x}) = \int \rho f(\boldsymbol{x}^*) F(\boldsymbol{x} - \boldsymbol{x}^*)d\boldsymbol{x}^* \tag{2.45}$$

Thus:

$$\tilde{f}(\boldsymbol{x}) = \frac{\int \rho f(\boldsymbol{x}^*) F(\boldsymbol{x} - \boldsymbol{x}^*)d\boldsymbol{x}^*}{\overline{\rho}} \tag{2.46}$$

The balance equations for the filtered values $\overline{f}$ or $\tilde{f}$ can be derived from filtering the balance equations. For the Reynolds-filtering, any quantity f may be decomposed into a filtered component $\overline{f}$, which is resolved in the numerical simulation, and $f' = f - \overline{f}$, corresponding to the unresolved part of the quantity f (i.e. the subgrid-scale part, due to the unresolved flow motions): $f = \overline{f} + f'$.. For the Favre-filtering, any quantity f may

be decomposed into a filtered component $\tilde{f}$, which is resolved in the numerical simulation, and $f'' = f - \tilde{f}$, corresponding to the unresolved part of the quantity f (i.e. the subgrid-scale part, due to the unresolved flow motions): $f = \tilde{f} + f''$. The filtering should be carefully conducted: in disagreement with classical Reynolds averaging, $\overline{f'}$ may be non-zero. In addition to $\overline{f'} \neq 0$ it holds: $\overline{\overline{f}} \neq \overline{f}$; $\quad \tilde{\tilde{f}} \neq \tilde{f}$; $\quad \widetilde{f''} \neq 0$. Finally, the derivation of balance equations for the filtered quantities $\overline{f}$ or $\tilde{f}$ requires the exchange of filtering and differentiation operators. This exchange is theoretically valid only under restrictive assumptions and is wrong, for example, when the filter's size varies. Note that the mesh size is dependent on the spatial position, and the filter size is correlated to that size. In [29], this issue has been thoroughly examined. Nonetheless, in most simulations, the uncertainties brought on by this operator exchange are typically ignored and are presumed to be taken into account in subgrid-scale modeling [19].

Favre-filtered balance equations

The Favre-filtered equations can be derived, as in [23], Favre-filtering the working equation set (2.19), (2.20), (2.21), (2.22), and (2.23) with a spatial filter:

Mass

$$\frac{\partial \overline{\rho}}{\partial t} + div(\overline{\rho}\tilde{\boldsymbol{u}}) = 0 \tag{2.47}$$

Momentum

$$\frac{\partial \overline{\rho}\tilde{\boldsymbol{u}}}{\partial t} + div(\overline{\rho}\tilde{\boldsymbol{u}}\tilde{\boldsymbol{u}}) + \nabla\overline{p} - div(\underline{\overline{\boldsymbol{\tau}}} - \overline{\rho}\underbrace{(\widetilde{\boldsymbol{u}\boldsymbol{u}} - \tilde{\boldsymbol{u}}\tilde{\boldsymbol{u}})}_{(1)}) = 0 \tag{2.48}$$

Species

$$\frac{\partial \overline{\rho}\tilde{Y}_k}{\partial t} + div(\overline{\rho}\tilde{\boldsymbol{u}}\tilde{Y}_k) = div\left[\underbrace{\overline{\rho\boldsymbol{V_k}Y_k}}_{(2)} - \overline{\rho}\underbrace{\left(\widetilde{\boldsymbol{u}Y_k} - \tilde{\boldsymbol{u}}\tilde{Y}_k\right)}_{(3)}\right] + \underbrace{\overline{\dot{\omega}_k}}_{(4)} \tag{2.49}$$

Energy equation (sensible enthalpy form):

$$\frac{\partial \overline{\rho}\tilde{h}_s}{\partial t} + div(\overline{\rho}\tilde{\boldsymbol{u}}\tilde{h}_s) = \underbrace{\overline{\dot{\omega}_T}}_{\simeq(4)} + div\left[\underbrace{\overline{\lambda_m\nabla T}}_{(5)} - \overline{\rho}\underbrace{\left(\widetilde{\boldsymbol{u}h_s} - \tilde{\boldsymbol{u}}\tilde{h}_s\right)}_{(6)}\right] - div\left(\underbrace{\overline{\rho\sum_{k=1}^{N}\boldsymbol{V}_kY_kh_k^s}}_{(7)}\right) \tag{2.50}$$

where $\dot{\omega}_T \doteq -\sum_{k=1}^{N} h_{f,k}^0 \dot{\omega}_k$, hence $\overline{\dot{\omega}_T} \doteq -\sum_{k=1}^{N} h_{f,k}^0 \overline{\dot{\omega}_k}$

Equation of state

$$\overline{p} = \frac{\overline{\rho} R \tilde{T}}{\tilde{W}} \tag{2.51}$$

In LES, operating the filtering leads to unclosed terms that need to be modeled. The objective of turbulent combustion modeling is to propose closures for the unknown quantities appearing in the filtered balance equations, that are enumerated in the equations (2.47) (2.48) (2.49) (2.50), such as:

- Unresolved Reynolds stresses $(\widetilde{u_i u_j} - \tilde{u}_i \tilde{u}_j)$ (1). The closure requires a subgrid-scale turbulence model (in the simulations of the present work the Zero-equation subgrid turbulent model is used).

- Unresolved species $(\widetilde{u_j Y_k} - \tilde{u}_j \tilde{Y}_k)$ (3) and enthalpy $(\widetilde{u_j h_s} - \tilde{u}_j \tilde{h}_s)$ (6) fluxes.

- Filtered species $\left(\overline{\rho \boldsymbol{V_k} Y_k}\right)$ (2) and enthalpy $\left(\overline{\rho \sum_{k=1}^{N} \boldsymbol{V}_k Y_k h_k^s}\right)$ (7) laminar diffusive fluxes, and filtered laminar heat diffusion flux $(\overline{\lambda_m \nabla T})$ (5). As in RANS, these molecular fluxes may be either neglected or modeled through a simple gradient assumption.

- Filtered species chemical reaction rates $\overline{\dot{\omega}_k}$ (4). Turbulent combustion modeling focuses on the closure of these mean burning rates.

These filtered balance equations (2.47), (2.48), (2.49), (2.50), combined with subgrid-scale models, may be numerically solved to simulate the unsteady (i.e. time-dependent) behavior of the filtered fields. Unresolved scales still have an impact on the filtered values through the unclosed terms that appear in the Favre-filtered equations, however, compared to DNS, some of the information contained in the subgrid (unresolved) scales is lost and should be modeled. Either using RANS or LES, combustion occurs at the unresolved scales of the computations.

3 | Modeling approach

The closure for the laminar diffusive fluxes (2), (5), (7) of equations (2.49) and (2.50) in this work is done using the classical gradient assumption [19]:

$$\overline{\rho \boldsymbol{V}_{k,i} Y_k} = -\overline{\rho} \overline{D}_k \frac{\partial \tilde{Y}_k}{\partial x_i} \quad \text{and} \quad \overline{\lambda_m \frac{\partial T}{\partial x_i}} = \overline{\lambda}_m \frac{\partial \tilde{T}}{\partial x_i} \tag{3.1}$$

Hence only the unresolved Reynolds stresses (1) of equation (2.48), the unresolved species (3) and enthalpy (6) fluxes, and the filtered reaction rate (4) of equations (2.49) and (2.50) must now be modeled. The modeling of (1),(3), and (6) is dealt with in the section 3.1, while the modeling of (4) is treated in section 3.3 after the necessary introduction of flame quantities that are going to be used.

3.1. Turbulence modeling

The objective of this section is to illustrate what are the main approaches, developed in non-reacting flows, to model the unresolved transport terms: Reynolds stresses $(\widetilde{u_i u_j} - \tilde{u}_i \tilde{u}_j)$ (1), scalar fluxes: $(\widetilde{u_j Y_k} - \tilde{u}_j \tilde{Y}_k)$ (3) and $(\widetilde{u_j h_s} - \tilde{u}_j \tilde{h}_s)$ (6).

3.1.1. Modeling of the unresolved Reynolds stresses

The most popular models are the Smagorinsky model, which expresses unresolved momentum fluxes according to the Bussinesq assumption; the Germano dynamic model, which estimates small scale dissipation from the knowledge of the resolved eddies, the Eddy diffusivity models and the One-equation model, which is used in the code that is used for the simulations of this work. Detailed analysis of the turbulence models can be found in [25].

One-equation model

The One-equation eddy viscosity subgrid-scale (SGS) model uses the eddy viscosity approximation, which consists in modeling the subgrid-scale (viscous) stress tensor as follows [19]:

$$\overline{\rho}(\widetilde{\boldsymbol{uu}} - \tilde{\boldsymbol{u}}\tilde{\boldsymbol{u}}) = -2\nu_T \left(\widetilde{S}_{ij} - \frac{1}{3}\widetilde{S}_{kk}\delta_{ij} \right) \tag{3.2}$$

where ν_T is the subgrid-scale eddy viscosity (or residual viscosity), $\widetilde{S}_{ij} = \frac{1}{2}\left(\frac{\partial \widetilde{u}_i}{\partial x_j} + \frac{\partial \widetilde{u}_j}{\partial x_i} \right)$ is the Favre-filtered strain tensor (resolved strain tensor) and δ_{ij} is the Kronecker delta.

Due to the fact that the main directions of the residual tensor and the filtered strain are not aligned, Meneveau [30] demonstrated that this assumption was wrong. Eddy-viscosity models are therefore more dissipative than necessary since they frequently overestimate the residual stress. A summary of the various residual viscosity models reported in the literature can be found, for instance, in [25]. These models were initially created for flows that were incompressible, and they were later modified for flows that had varying densities (e.g. combustion)

The residual viscosity is modeled in this work as:

$$\nu_T = C_v k_r^{1/2} \Delta \tag{3.3}$$

where Δ is the LES-filter width, C_v is a model constant whose default value is $\simeq 0.1$ and k_r is the residual kinetic energy, defined as:

$$k_r \doteq \frac{1}{2}\left(\widetilde{u_i u_i} - \widetilde{u}_i \widetilde{u}_i \right) \tag{3.4}$$

for which a transport equation, further analyzed in [19], is solved:

$$\bar{\rho}\frac{Dk_r}{Dt} = \frac{\partial}{\partial x_j}\left(\widetilde{\mu}\frac{\partial k_r}{\partial x_j} \right) + \widetilde{u}_i \frac{\partial \tau_{ij}^R}{\partial x_j} - \frac{\partial f_j}{\partial x_j} - \varepsilon_k + \Pi \tag{3.5}$$

The main difference with the Zero-equation (eddy viscosity) model, e.g. Smagorinsky model in which the closure of k_r is algebraic and no transport equation is solved, is the resolution of a transport equation for k_r in order to account for the historic effect of k_r due to production, dissipation and diffusion. The main reason for developing the One-equation subgrid-scale models is to overcome the deficiency of local balance assumption between the subgrid-scale energy production and dissipation adopted in Zero-equation eddy viscosity models. Such a phenomenon may occur in high Reynolds number flows.

The transport equation (3.5) represents an enhancement of non-reacting flow's version in the case of combustion.

3.1.2. Modeling of the unresolved scalar transport

As in RANS, LES unresolved scalar fluxes are often described using a gradient assumption [19], and this work is no exception:

$$\widetilde{u_j Y_k} - \tilde{u}_j \tilde{Y}_k = -\frac{\nu_t}{Sc_k}\frac{\partial \tilde{Y}_k}{\partial x_i} \tag{3.6}$$

where Sc_k is a subgrid-scale Schmidt number. The subgrid-scale viscosity ν_t is estimated from the unresolved Reynolds stresses models (i.e. One-equation model in this work). Since the majority of transport is addressed at large scales and only a portion needs to be represented, the gradient hypothesis in LES is effective in the majority of cases [31]. Therefore, it is acceptable to use a gradient hypothesis [32].

3.2. Towards Combustion modeling

In this section, the elements needed to address the combustion modeling are going to be introduced.

3.2.1. Basic properties of premixed and non-premixed flames

Laminar premixed flames

Figure 3.1 depicts the structure of a laminar premixed flame. In a premixed flame, fresh gases (i.e. the fuel and the oxidizer) are combined at the molecular level prior to combustion. A thin reaction zone, whose thickness is the thermal flame thicknesses δ_l and whose typical values range from 0.1 to 1 $[mm]$, separates unburnt gases from burned gases (i.e. combustion products). There are various ways to define δ_l , but in general, one may state that it relates to a temperature jump of 98% of the difference between the temperature of fresh and completely burnt gases. The preheat and reaction zones exhibit a significant temperature gradient, and this gradient maintains the conductive thermal transfer from burnt gases to fresh gases, preheating the latter and aiding in their ignition (i.e. rising temperatures also accelerate reactions until the fresh mixture ignites). To keep the flame alive and unquenched, a strong temperature gradient is essential. Temperature ratios between burnt and fresh gases are typically between 5 and 7. Premixed flames also

have the ability to spread towards fresh gases; in the event of a deflagration, the laminar flame speed S_L (also known as S_L^0 when the flame is plane) measures how quickly the flame front spreads in a frame of reference fixed to the fresh gases. The local imbalance between chemical consumption and heat diffusion causes the flame front to spread. A laminar flame propagates at a pace of around $0.1 - 1[m/s]$, and depends on factors including the compositions of the fuel and oxidizer, fresh gases temperature, and other factors. For a simple one-step irreversible chemical scheme:

$$reactants \longmapsto products \tag{3.7}$$

Progress variable c, whose boundary conditions are $c = 0$ in the unburned gases and $c = 1$ in the fully burned ones, is used to describe the flame. Typically, a reduced mass fraction or reduced temperature is employed to define the progress variable:

$$c(\boldsymbol{x}, t) \doteq \frac{T - T_u}{T_b - T_u} \quad \text{o} \quad c(\boldsymbol{x}, t) \doteq \frac{Y_F - Y_F^u}{Y_F^b - Y_F^u} \tag{3.8}$$

where T and Y_F stand for the local temperature and fuel mass fraction, and u and b represent quantities that have been evaluated in the *unburnt* and *burnt* gases, respectively. In this work the definitions of the progress variable that are used are the following:

$$
\begin{cases}
c(\boldsymbol{x}, t) \doteq \dfrac{(Y_{CO_2} + Y_{CO}) - \overbrace{(Y_{CO_2} + Y_{CO})^u}^{=0}}{max\{(Y_{CO_2} + Y_{CO}) - (Y_{CO_2} + Y_{CO})^u\}} & \text{(3.9a)} \\[3ex]
c(\boldsymbol{x}, t) \doteq \dfrac{(Y_{CO_2} + Y_{CO} + Y_{H_2O}) - \overbrace{(Y_{CO_2} + Y_{CO} + Y_{H_2O})^u}^{=0}}{max\{(Y_{CO_2} + Y_{CO} + Y_{H_2O}) - (Y_{CO_2} + Y_{CO} + Y_{H_2O})^u\}} & \text{(3.9b)} \\[3ex]
c(\boldsymbol{x}, t) \doteq \dfrac{Y_{H_2O} - \overbrace{Y_{H_2O}^u}^{=0}}{max\{Y_{H_2O} - Y_{H_2O}^u\}} & \text{(3.9c)}
\end{cases}
$$

where (3.9a) is used for pure methane combustion, (3.9b) is used for hydrogen-methane blend combustion, and (3.9c) is used for pure hydrogen combustion.

The transport equation for the progress variable is, for unity Lewis number (i.e. same molecular and thermal diffusivities), without heat losses (i.e. adiabatic combustion, which

is the case of this work), assuming $D_{jk} = D$ for all species:

$$\underbrace{\frac{\partial \rho c}{\partial t}}_{\text{accumulation}} + \underbrace{div(\rho \boldsymbol{u} c)}_{\text{avvection}} = \underbrace{div(\rho D \nabla c)}_{\text{diffusion}} + \underbrace{\dot{\omega}_c}_{\text{source term}} \tag{3.10}$$

where $\dot{\omega}_c$ is the source term of the progress variable, a linear combination of $\dot{\omega}_k$ (if $c \doteq \sum_{k=1}^{N} \alpha_k Y_k$, where α_k are typically chosen such that c results to be monotonic function of x in a 1-D flame, then $\dot{\omega}_c = \sum_{k=1}^{N} \dot{\omega}_k$ [33]), and thus it is an unclosed term.

The transport equation (3.10) can be rearranged in a propagative form by including the displacement speed ω of the $iso - c$ surfaces (i.e. ω measures the displacement of a $iso - c$ surface relative to the flow) in order to demonstrate the contributions due to molecular diffusion normal (which may be expressed using Markstein's lengths [34]) and tangential to the $iso - c$ surface, as well as due to the reaction rate.
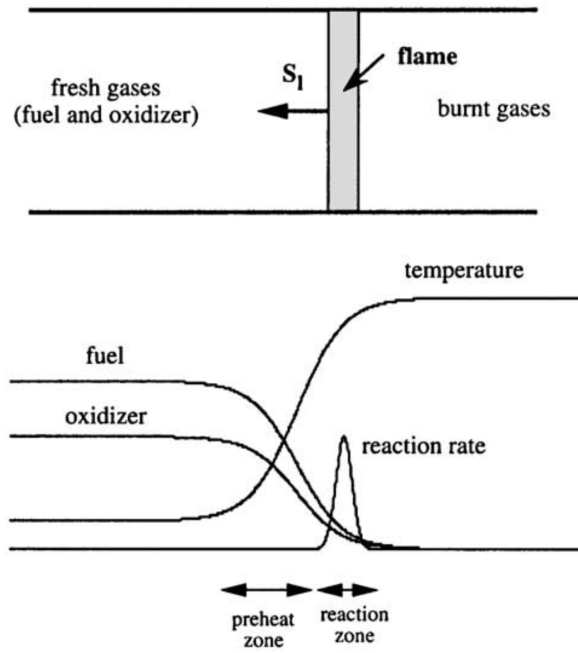
Figure 3.1: Laminar plane premixed flame and its steady chemical and thermodynamic quantities in the space. This figure is taken from [18].

Laminar diffusion flames

In laminar diffusion flames, fuel and oxidizer are separated and located on either side of the reaction zone, which is where the heat is released. The reactants' molecular diffusion toward the reaction zone controls the burning rate. Consequently, ratios between

characteristic times indicative of molecular diffusion and chemistry determine the structure of a steady diffusion flame. Contrary to premixed flames, diffusion flames do not benefit from a self-induced propagation mechanism (i.e. preheating zone) and are instead primarily mixing-controlled: in non-premixed combustion, the flame is located where the fuel and oxidizer mix in stoichiometric proportion. Additionally, a diffusion flame's thickness is not constant and varies according to the characteristics of the local flow. Figure 3.2 depicts a laminar diffusion flame's general structure.
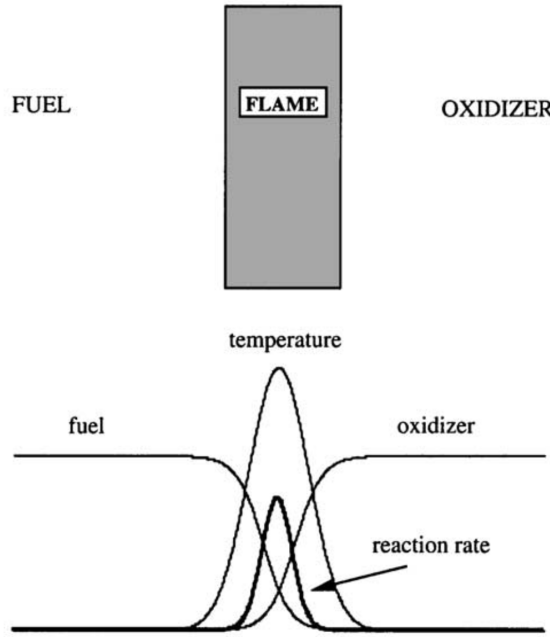
Figure 3.2: Laminar diffusion (i.e. non-premixed) flame and its steady chemical and thermodynamic quantities in the space. This figure is taken from [18].

Now the concept of mixture fraction, useful for the partially-premixed flames investigation of this work, is going to be introduced. Consider the irreversible single-step chemical reaction between fuel and oxidizer:

$$aF + bO \longrightarrow (a+b)P \tag{3.11}$$
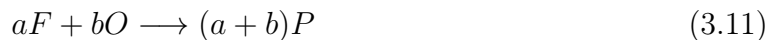
where $a = \nu_F W_F$ and $b = \nu_O W_O$ are mass stoichiometric coefficients. The balance equations of species, necessary to identify the properties of the flame together with the temperature equation, can be written as:

$$\frac{\partial \rho Y_F}{\partial t} + div(\rho \boldsymbol{u} Y_F) = div(\rho D_F \nabla Y_F) + \nu_F W_F \dot{\omega} \tag{3.12}$$

$$\frac{\partial \rho Y_O}{\partial t} + div(\rho \boldsymbol{u} Y_O) = div(\rho D_O \nabla Y_O) + \nu_O W_O \dot{\omega} \qquad (3.13)$$

where $\dot{\omega} \left[\frac{kmol_{reaction}}{s}\right]$ is the reaction rate, $\nu_k \left[\frac{kmol_k}{kmol_{reaction}}\right]$ is the stoichiometric coeffi-
cient of the species k of the reaction (ν_k is negative for reactants, which are consumed,
and positive for products, which are generated by the chemical reaction) and W_k is the
molar weight of the species k. Note that the (mass) reaction rate of the species k can be
expressed as $\dot{\omega}_k = \nu_k W_k \dot{\omega}$. The molecular diffusion is expressed using Fick's law.
Furthermore, assuming equal molecular diffusivities (i.e. $D_F = D_O \doteq D$), the existence
of a conserved scalar may be highlighted by subtracting to (3.12) multiplied by $1/a$ the
equation (3.13) multiplied by $1/b$:

$$\frac{\partial}{\partial t}\left(\rho\left[\frac{Y_F}{a} - \frac{Y_O}{b}\right]\right) + div\left(\rho\boldsymbol{u}\left[\frac{Y_F}{a} - \frac{Y_O}{b}\right] - \rho D\nabla\left[\frac{Y_F}{a} - \frac{Y_O}{b}\right]\right) = \underbrace{\left(\frac{\dot{\omega}_F}{a} - \frac{\dot{\omega}_O}{b}\right)}_{=0 \text{ being } \dot{\omega}_F = \dot{\omega}_O a/b}$$

$$(3.14)$$

where the quantity $\beta = \left[\frac{Y_F}{a} - \frac{Y_O}{b}\right]$ results to be the conserved scalar (also called 'passive
scalar') being that it respects the transport equation with no source term:

$$\frac{\partial \rho \beta}{\partial t} + div(\rho \boldsymbol{u} \beta - \rho D \nabla \beta) = 0 \qquad (3.15)$$

A commonly used conserved scalar, which then respects the transport equation with no
source term, is the mixture fraction which is defined normalizing $\beta = \left[\frac{Y_F}{a} - \frac{Y_O}{b}\right]$ using
values in the fuel and oxidizer streams:

$$Z(\boldsymbol{x}, t) = \frac{FAR_{st}\dfrac{Y_F}{Y_{F,o}} - \dfrac{Y_O}{Y_{O,o}} + 1}{FAR_{st} + 1} \qquad (3.16)$$

where $Y_{F,o}$ is the mass fraction of fuel in the fuel stream and, similarly, $Y_{O,o}$ is the oxidizer

mass fraction in the oxidizer stream. The $FAR_{st} \doteq a/b$ is the stoichiometric mass fuel to oxidizer ratio, defined as:

$$FAR_{st} = \frac{\text{stoichiometric mass of fuel}}{\text{mass of oxidizer}} = \frac{Y_{F,st}}{Y_O} = \frac{a}{b} \tag{3.17}$$

Another important quantity has to be defined, the equivalence ratio:

$$\phi \doteq \frac{FAR}{FAR_{st}} \tag{3.18}$$

where $FAR = \dfrac{Y_F}{Y_O}$ is the actual fuel to air ratio.

The mixture fraction evolves through the diffusive layer from zero (oxidizer) to one (fuel), and the diffusion flame is fully determined when $Z(\boldsymbol{x},t)$ and any one of $T(\boldsymbol{x},t), Y_F(\boldsymbol{x},t)$ or $Y_O(\boldsymbol{x},t)$ is known.

Being a passive scalar, the mixture fraction respects the following transport equation (with no source term):

$$\frac{\partial \rho Z}{\partial t} + div(\rho\boldsymbol{u}Z - \rho D \nabla Z) = 0 \tag{3.19}$$

The mixture fraction, represents the local amount of mass in the (infinitesimal) control volume which originates in the fuel stream. When dealing with diffusion flames where the fuel and oxidizer streams are initially divided, this conservative scalar is especially helpful. Unless the flame is partially premixed, a conservation equation for Z in the case of perfectly premixed combustion gives no information because the mixture fraction is uniform everywhere under the assumption that all species have the same diffusivities. The mixing fraction can be compared to the equivalency ratio, being the two quantities in a biunivocal relationship under certain assumptions.

In diffusion flames, the mixture fraction can be used to determine where the flame is located. The diffusion flame is resides on level surfaces inside the mixing domain where it is the fuel and oxygen are combined in stoichiometric proportion: the equation $Z(\boldsymbol{x},t) = Z_{st}$, where Z_st is the stoichiometric mixture fraction, identifies iso-Z surfaces where the flame resides. Z_{st} can be computed by setting $Y_F = Y_O = 0$ (since if they were to react to consume fuel and oxygen, only on the stoichiometric locations both fuel and oxygen will be consumed completely).

Partially premixed flames

Before the reaction takes place in non-premixed combustion, there may already be some partial premixing of the reactants. Alternately, it is possible for incomplete premixing to take place in premixed combustion before the mixture enters the combustion chamber. Situations like this are examples of so-called partially premixed flames. In these circumstances, the description should consider either the progress variable (appropriate for premixed flames) and the mixture fraction (suited for non-premixed flames), as is further detailed in the section on the Flamelet model. The combustion is said to occur under *lean* condition if $\phi < 1$, *stoichiometric* condition if $\phi = 1$, and *rich* condition if $\phi > 1$.

3.2.2. Scales and diagrams for turbulent combustion

Deriving models for turbulent combustion requires a physical approach because the filtered burning rate $\overline{\dot{\omega}_k}$ cannot be determined from a filtered Arrhenius law, according to [18]. Different length scales, velocities, and time scales are used to describe the turbulent flow field and chemical reactions in turbulent combustion. Comparing these scales is the primary method of the physical analysis. The turbulent flow is characterized by a Reynolds number that compares turbulent transport to viscous forces:

$$Re = \frac{u'l_t}{\nu} \tag{3.20}$$

where u' is the velocity rms, l_t is the turbulence integral length scale and ν the kinematic viscosity of the flow.

Note on u'. u' is related to the square root of the turbulent kinetic energy k, which is usually defined [23] as $k \doteq \frac{1}{2}\left(\overline{(u')^2} + \overline{(v')^2} + \overline{(w')^2}\right)$ where $u' = u - \overline{u}$, whose mean and variance are: $\overline{u'} = \frac{1}{T}\int_0^T u(t) - \overline{u}dt = 0$ and $\overline{(u')^2} = \frac{1}{T}\int_0^T (u(t) - \overline{u})^2 dt \geq 0$, similarly for v' and w'.

The Damköhler number compares the turbulent $(\tau_t = l_t/u')$ and the chemical (τ_c) time scales:

$$Da = \frac{\tau_t}{\tau_c} \tag{3.21}$$

In the limit of high Damköhler numbers $(Da >> 1)$, the chemical time is short compared to the turbulent time, corresponding to a thin reaction zone distorted and convected by the flow field. The internal structure of the flame is not strongly affected by turbulence and may be described as a laminar flame element called a 'flamelet' (from here the name

'Flamelet model'). The turbulent structures wrinkle and strain the flame surface.
On the other hand, a low Damköhler number ($Da << 1$) corresponds to a slow chemical reaction. Reactants and products are mixed by turbulent structures before reaction.

In turbulence, as long as quenching does not occur, most practical situations correspond to high or medium values of the Damköhler. Obviously, various chemical time scales may be encountered: fuel oxidation generally corresponds to short chemical time scales ($Da >> 1$) whereas pollutants production or destruction such as CO oxidation or NO formation are slower. These different time scales among different species are the reason for the stiffness problem when dealing with the reaction rate of different species: some are really slow (i.e. low reaction rates) whereas some are really fast (i.e. high reaction rates)

3.2.3. Turbulent premixed combustion diagram

In this paragraph it is analyzed the premixed turbulent combustion regimes [23] by comparing turbulence and chemical characteristic length and time scales. The outcome of the analysis is the combustion diagrams showing various regimes for different values of two dimensionless numbers: Damköhler and Karlovitz. In premixed flames, the chemical time scale can be expressed as $\tau_c = \delta_l/S_L$ where δ_l is the laminar flame thickness and S_L is the laminar flame speed; τ_c corresponds to the time required for the premixed flame to propagate over a distance equal to its own thickness.
Thus, the Damköhler results to be:

$$Da = \frac{l_t}{\delta l}\frac{S_L}{u'}. \tag{3.22}$$

The Karlovitz number Ka compares the chemical time scale with the time scale of the smallest turbulence scales (i.e. the Kolmogorov scales):

$$Ka = \frac{\tau_c}{\tau_k} = \frac{\delta_l}{l_t}\frac{u_k}{S_L} \tag{3.23}$$

where the Kolmogorov length scale l_k is $\left(l_k = \dfrac{\nu^3}{\epsilon}\right)^{1/4}$ and the velocity of the Kolmogorov structures u_k is given by $u_k = (\nu\epsilon)^{1/4}$ Rearranging the Karlovitz number, it can be noted that it also compares the flame and the Kolmogorov length scales according to: $Ka = \left(\dfrac{\delta_l}{l_t}\right)^2$. Some considerations based on the values of the couple (Da, Ka) are:

- For $Da >> 1$ the flame front is thin and its inner structure is not affected by

turbulence motions which only wrinkle the flame surface. This is called the 'flamelet regime' and occurs when the smallest turbulence scales (i.e. Kolmogorov scales) have a turbulent time τ_k larger than τ_c (i.e. turbulent motions are too slow to affect the flame structure). On the other hand, when $Da << 1$, the chemical time is larger than turbulent times and the overall reaction rate is therefore controlled by chemistry whereas reactants and products are mixed by turbulence motions. This limit case is the so-called 'perfectly stirred reactor'.

- The Karlovitz number is used to define the Klimov-Williams criterion, corresponding to $Ka = 1$. This criterion was first interpreted as the transition between the flamelet regime ($Ka < 1$) and the so-called 'distributed combustion regime', where the flame inner structure is strongly modified by turbulence motions. A recent analysis [35] has shown that for Karlovitz numbers larger than unity ($Ka > 1$), turbulent motions become able to affect the flame's inner structure but not necessarily the reaction zone, hence extending the validity of the flamelet regime (and consequently the validity of the flamelet model that is used for this work) to higher Karlovitz number's values (approximately $Ka = 100, 1000$).

The reaction zone, where heat is released, has a thickness δ_r much lower than the thermal thickness δ_l of the flame ($\delta_r \simeq 0.1\delta_l$).

Then, the following turbulent premixed flame regimes are proposed [18], not taking into account [35]:

- $Ka < 1$: *Flamelet regime*, fig.3.3a. The chemical time scale is shorter than any turbulent time scale and the flame thickness is smaller than the smallest turbulent scale. In this regime the flame front is thin, has an inner structure close to a laminar flame and is wrinkled by turbulence motions. Two subdivisions of this regime may be proposed depending on the velocity ratio u'/S_L:

    $(u'/S_L) < 1$ *wrinkled flame*. As u' may be viewed as the rotation speed of the larger turbulent motions (i.e. integral scale), turbulent structures are unable to wrinkle the flame surface up to flame front interactions. The laminar propagation is predominant and turbulence/combustion interactions remain limited

    $(u'/S_L) > 1$ *wrinkled flame with pockets*. In this situation, larger structures become able to induce flame front interactions leading to pockets of fresh and burnt gases (i.e. structures that are richer or leaner in fuel).

- $1 < Ka \leq 100$: *Thickened wrinkled flame*, fig.3.3b. In this case, turbulent motions are able to enter and modify (thicken) the flame preheat zone, but cannot modify

the reaction zone which remains thin and close to a wrinkled laminar reaction zone.

- $Ka > 100$ *Thickened flame regime or well-stirred reactor*, fig.3.3c. In this situation, preheat and reaction zones are strongly affected by turbulent motions and no laminar flame structure may be identified.

(a) flamelet regime.   (b) thickened wrinkled flame regime.

(c) thickened flame regime.
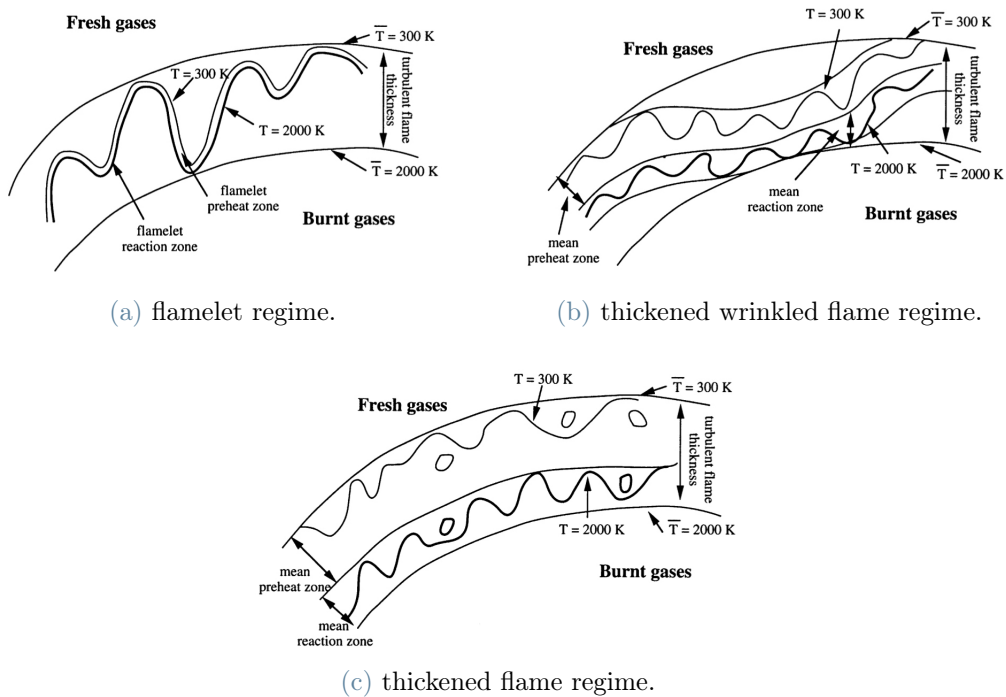
Figure 3.3: Turbulent premixed combustion regimes as identified by Borghi and Destriau [36]

These various regimes are generally displayed on a log-log diagram (u'/S_L *vs* l_t/δ_l), called 'Borghi diagram', which is shown in fig. 3.4:
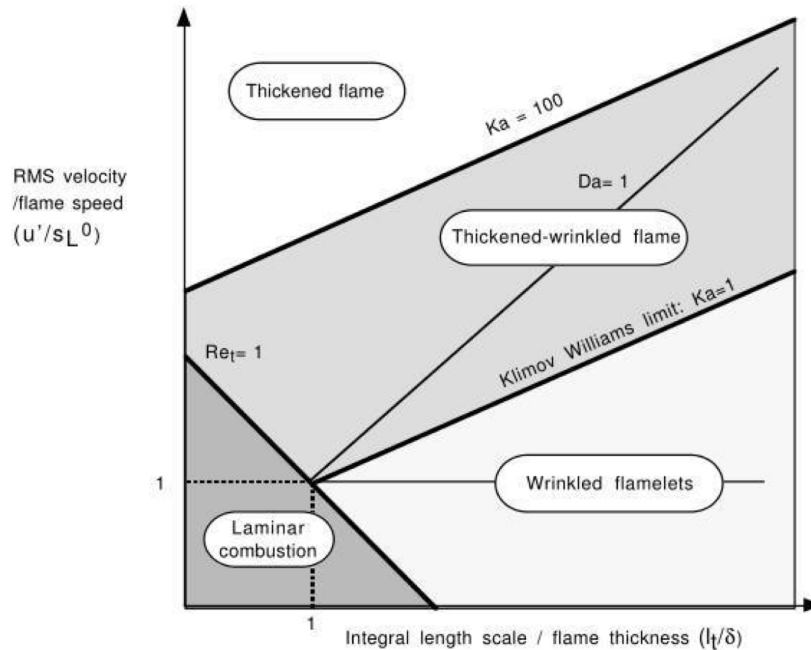
Figure 3.4: Borghi diagram (turbulent combustion diagram): combustion regimes are identified in terms of length (l_t/δ_l) and velocity (u'/S_L) ratios in a log-log diagram.

The list above, which is a rough classification of combustion regimes as a function of characteristic numbers, has been developed as a support to choose turbulent combustion models. Most practical applications correspond to flamelet or thickened wrinkled flame regimes. Nevertheless, as already mentioned with [35], such analyses are only qualitative and should be used with care, also because all these analyses are based on a single-step irreversible reaction (i.e. Reactants $\longmapsto$ Products) but in actual turbulent combustion a large number of chemical species and reactions are involved (several hundred species and several thousand reactions for most hydrocarbons/air mixture). These reactions may correspond to a large range of chemical time scales. For instance, it is reasonable to suppose that the oxidation of propane is fast in comparison to the turbulent time scale, yet the formation of CO_2 from CO is much slower and has a chemical time of the same order as turbulent times. Another crucial feature is that the analysis is based on the assumption that the turbulence is homogeneous and isotropic frozen (i.e. unaffected by heat release)

The flamelet

The [35] defines 'flamelets' in the following way: flamelet have two properties: (a) it is a wrinkled layer that contains both a preheat and a reaction region, and (b) its internal

structure is defined by a set of "state relations" that should similar to, but may not be exactly equal to, the state relations for a laminar flame (i.e. the internal structure of the flamelet contains profile of species mass fractions versus progress variable, called state relations or conditional mean profiles, that are similar to those of a laminar flame). Flamelet models are based on the assumption that the state relations computed for a strained, laminar flame can be used to compute the properties of a turbulent flame (that is seen as made up of many of these flamelets) [35], but the models do not require that the flamelets remain thin.

3.3.   Combustion modeling

A direct approach to describe turbulent combustion is first discussed in this section. As already mentioned, the filtered reaction rate closure is going to be addressed here.

Direct closure of the filtered reaction rate: Taylor's expansion

This simple formalism [18], based on series expansion, illustrates the difficulties arising from the non-linear character of the chemical sources $\dot{\omega}_k$.

Consider a simple irreversible reaction between fuel (F) and oxidizer (O):

$$F + sO \longrightarrow (1 + s)P \tag{3.24}$$
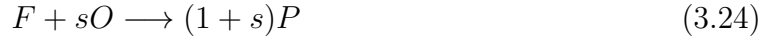
where the fuel mass reaction rate $\dot{\omega}_F$ is expressed from the Arrhenius law as:

$$\dot{\omega}_F = -A\rho^2 Y_F Y_O T^b exp(-T_A/T) \tag{3.25}$$

where b is a constant, A is the pre-exponential constant, and T_A is the activation temperature. The filtered reaction rate cannot be simply described as a function of the filtered mass fractions $\tilde{Y}_F$ and $\tilde{Y}_O$, the filtered density $\bar{\rho}$, and the filtered temperature $\tilde{T}$ since the reaction rate is extremely non-linear. The first straightforward approach is to disregard subgrid-scale fluctuations and assume perfect mixing at the subgrid-scale level. Thus, the filtered reaction rate is expressed as:

$$\overline{\dot{\omega}_F} = -A\bar{\rho}^2 \tilde{Y}_F \tilde{Y}_O \tilde{T}^b exp(-T_A/\tilde{T}) \tag{3.26}$$

This expression implicitly presupposes that all chemical time scales τ_c are longer than the turbulent subgrid time scale τ_t (i.e. $\tau_t << \tau_c$), which results in $Da << 1$. However, this

assumption is not valid in most combustion applications. For this reason, combustion models have been developed. Typical combustion models, that are used for the closure of the filtered reaction rate, are [37]: conditional moment closure (CMC) method, transported probability density function (TPDF) method, Thickened Flame (TF) method and the Flamelet model (FM). In this work, the latter is going to be used, while the first three models are explained in depth in [19]. The CMC and flamelet-based models are conserved scalar-based methods, and use a presumed PDF approach to describe the mixture fraction distribution. The flamelet model that is used in this work is also based on the progress variable, whose sub-grid scale distribution is described using the presumed beta PDF as well. The progress variable is not a passive scalar but rather a reactive scalar since it has a source term. The [18] explains in depth all the details of the existing combustion models.

3.3.1. Flamelet model with presumed PDF

The particular Flamelet model used in this work is now going to be introduced [38, 39]. Two control variables are included for the chemistry representation: the progress variable c and the mixture fraction Z. They are sufficient since it is assumed adiabatic combustion (hence the extensive enthalpy, and not the specific enthalpy, is conserved in the combustion chamber), whereas in presence of heat losses also the enthalpy needs to be used to take this aspect into account. The interaction between chemistry and turbulence is considered through a presumed beta-shaped probability density function (PDF) approach, which is considered for the progress variable and mixture fraction and results in two extra control variables: progress variable variance and mixture fraction variance. The resulting turbulent manifold is four-dimensional, in which the dimensions are progress variable, mixture fraction, progress variable variance and mixture fraction variance. The Flamelet model has also the objective of chemistry reduction, which means not solving all the filtered species equations and not considering the complete chemical scheme, which reduces the computational effort and solves the stiffness problem related to the reaction rate. OpenFOAM simulations will be performed for a turbulent swirling flame in a gas turbine combustor by means of the present 4-D Flamelet model implementation coupled to an LES turbulence model (One-equation model), and the results will be compared with experimental PIV data. The inclusion of heat loss would enhance the temperature predictions in the whole burner and improve the NO predictions. The use of a similar 5-D combustion model, that considers also enthalpy, shows these improvements and that combustion features at gas turbine conditions can be satisfactorily reproduced with a reasonable computational effort [20]. The reason why this Flamelet combustion model is

used in this work is that it retains most of the physical accuracy of a detailed simulation while drastically reducing its computational time, paving the way for new developments of alternative fuel usage (e.g. hydrogen) in a cleaner and more efficient combustion.

Due to existing and upcoming computational power restrictions, it is not possible to simulate a whole practical combustion equipment in detail, resolving every scale of aerodynamic motion and chemistry (DNS with complete chemistry).

Applying LES can theoretically reduce computation by a factor of 10 or more. However, considering the significant reduction in equations (i.e. species balance equations) that must be solved at runtime for the chemistry alone, the amount of computational effort reduction that the chemistry model gives is also quite relevant.

Flamelet model (FM)

The description of the flame is approached differently by laminar flamelet models. These approaches make the assumption that the turbulent flame brush is made up of a collection of discrete, laminar, one-dimensional flames known as flamelets, as previously mentioned in this chapter. According to this assumption, it is possible to isolate thin, quasi-one-dimensional flame structures in multi-dimensional flames and, as a result, identify the main direction of the gradients of the thermochemical variables. This assumption can be expanded to include turbulent flames using a scale analysis [23]. When turbulent eddies are unable to enter and modify the inner reaction zone, quasi-one-dimensional flame formations do in reality exist [23] (i.e. in the flamelet region previously identified in the Borghi diagram).

In the FM, in a pre-processing stage, a database of thermochemical variables is created for a set of initial conditions and stored as a function of a select few controlling factors [20]. Only the transport equations for the control variables must be solved during the flame simulation; the pre-calculated chemistry manifold can be used to retrieve all of the dependent thermochemical variables. Detailed solutions of 1-D laminar premixed flames with complex chemistry are used as the basis of this tabulation, and can be easily computed using already existing 1D flame codes (e.g. CHEM1D [40], Cantera, etc) coupled with chemical schemes (e.g. GRI-Mech 3.0 kinetic mechanism [41], Burke mechanism [42]). The model used in this work uses CHEM1D coupled with the GRI-Mech 3.0 complex chemistry mechanism for the computation of the 1-D laminar premixed flamelets with complex chemistry to build the 2-D manifold. The steps of the FM are going to be addressed.

Step 1. FM database generation

The first step is to generate the database of thermochemical quantities starting from a laminar 1-D premixed flame (i.e. one of the generic flamelets).

A linear combination of species mass fractions defines the progress variable, where the weighting coefficients are arbitrarily chosen to ensure a monotonic profile of c along the 1-D laminar flame. The progress variable quantitatively characterizes the transition from fresh gases to burnt gases. Additionally, fuel and oxidizer are not completely blended before combustion, but the premixed flame mode is maintained (i.e. partially premixed flame). In order to consider these two aspects, it is necessary to solve a collection of laminar flamelets (i.e. solve the flamelet equations, which are the laminar transport equations: mass, momentum, species, energy) for various values of progress variable c and mixture fraction Z. This passage introduces Z and c as two control variables. The solutions, as above mentioned, are computed with the aid of codes and kinetic schemes. At first, the flamelets are computed as steady, fully premixed, flat flames, for a given pressure, composition and temperature of the inlet mixture. Figure 3.5 shows the resulting laminar manifold, which is again two dimensional at this point: the different scalars { Y_k, T, mixture c_p, mixture density ρ, the reaction rate of the species k $\dot{\omega}_k$, source term of c ω_c, kinematic viscosity, etc } are depicted as a function of the equivalence ratio (that can be considered equivalent to the mixture fraction) and progress variable.

(a) equivalence ratio.

(b) source term of the progr. var.

(c) temperature.
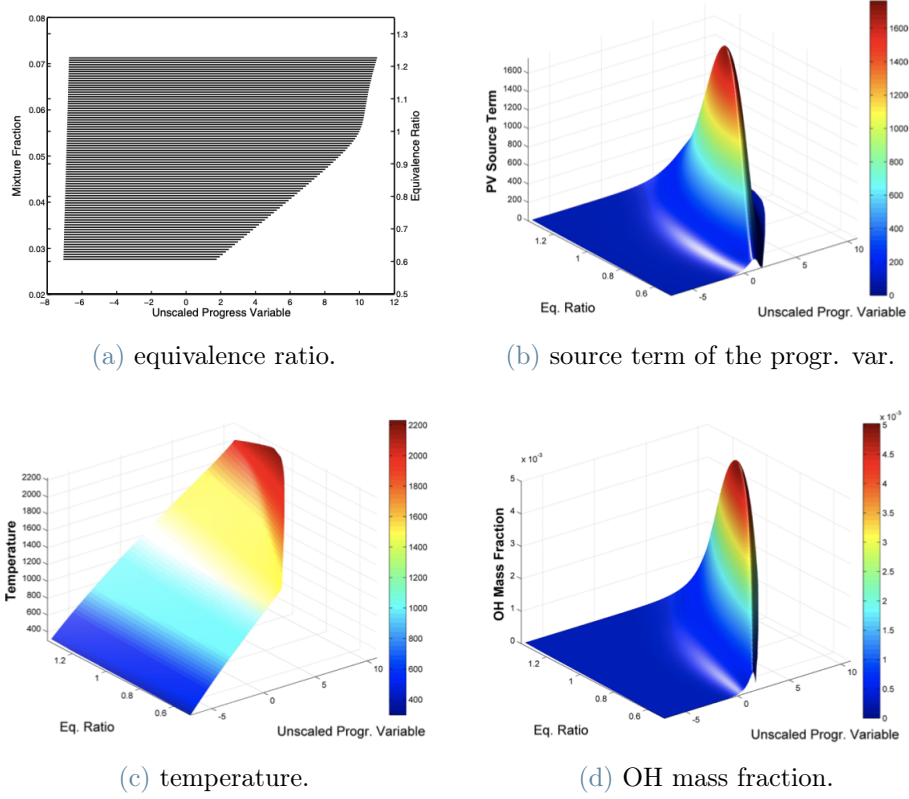
(d) OH mass fraction.

Figure 3.5: Representations of the laminar manifold. (a) equivalence ratio along the flamelets composing the manifold. (b) source term of the progress variable along the manifold. (c) temperature along the manifold. (d) mass fraction of OH along the manifold. [20]

The range in which Z varies is given by the flammability limits while c can take values between zero and one.

Step 2. Address the turbulence-chemistry interaction

In this step, the tabulated values of step 1. must be integrated with the joint PDF of Z and c, $\tilde{P}(Z,c)$ to take into account the statistical properties of small scales of the simulated field in a LES (or in other words, presumed subgrid-scale PDF takes into account the turbulence-chemistry interaction for the progress variable and mixture fraction). Assuming that the progress variable and the mixture fraction are statistically independent in the flame, that allows to say $\tilde{P}(Z,c) \simeq P_\beta(Z; \tilde{Z}, \widetilde{Z''^2}) \times P_\beta(c; \tilde{c}, \widetilde{c''^2})$ as further explained in [22, 38], the filtered source term of the progress variable is calculated as [20]:

$$\overline{\dot{\omega}_c} = \int \int \dot{\omega}_c(c, Z) P(c; \tilde{c}, \widetilde{c''^2}) P(Z; \tilde{Z}, \widetilde{Z''^2}) dc dZ \tag{3.27}$$

where the PDF used are both presumed β-PDF and account for the subgrid-scale statistical properties of the turbulent flame (e.g. the position of the flame inside a cell of the grid, that can modify values of the thermochemical quantities and is treated from a statistical point of view through PDF).

On the interval $0 \leq x \leq 1$, the two-parameter family of beta distributions is given by [22]:

$$P(x; a, b) = x^{a-1}(1-x)^{b-1}\frac{\Gamma(a+b)}{\Gamma(a)\Gamma(b)} \tag{3.28}$$

where the distribution's mean and variance (μ, σ^2) are related to the parameters a and b by:

$$a = \frac{\mu(\mu - \mu^2 - \sigma^2)}{\sigma^2}, \quad b = \frac{(1-\mu)(\mu - \mu^2 - \sigma^2)}{\sigma^2}. \tag{3.29}$$

When applied to the progress variable then $x \longmapsto c$, $\mu \longmapsto \tilde{c}$, and $\sigma^2 \longmapsto \widetilde{c''^2}$; whereas when applied to the mixture fraction then $x \longmapsto Z$, $\mu \longmapsto \tilde{Z}$, and $\sigma^2 \longmapsto \widetilde{Z''^2}$.

This β-PDF approach as a model for subgrid mixture fraction and progress variable fluctuations in LES has been successfully applied in a number of previous studies: in the context of the fast chemistry model in homogeneous turbulence, Cook and Riley [43] tested the β-PDF with good results. Jimenez [44] used data from a highly intermittent, incompressible, turbulent mixing layer to show the β-PDF model's strong performance. On top of that, β-PDF was put to the test in the presence of heat release by Wall and Moin in 2000 [45]. Additionally, it has been demonstrated [43, 45] that predicting the subgrid variance accurately is the key to using the β-PDF effectively.

The manifold gains two additional dimensions as a result of this convolution procedure, eventually reaching a total of four dimensions: the filtered progress variable $\tilde{c}$, the filtered mixture fraction $\tilde{Z}$, the variance of the filtered progress variable $\widetilde{c''^2}$, and the variance of the filtered mixture fraction $\widetilde{Z''^2}$. Obviously, all the filtered quantities { $\tilde{Y}_k$, $\tilde{T}$, mixture density $\overline{\rho}$, mixture $\tilde{c}_p$, the reaction rate of the species k $\overline{\dot{\omega}_k}$, source term of c $\overline{\dot{\omega}_c}$, etc } values can now be computed with the use of the PDFs (i.e. integrating the laminar manifold with the PDFs, hence obtaining the filtered-quantities 4-D manifold) for different values of the control variables and then stored, for subsequent retrieval, in a 4-D manifold. In the end, this "look-up table" method allows for the computation of the reactive part (i.e., chemical species mass fractions and energy equations), which makes it different from a non-reactive problem.

Step 3. The storage of the 4-D manifold

The tabulation technique consists of discretizing the 4-D ($\tilde{c}, \tilde{Z}, \widetilde{c''^2}, \widetilde{Z''^2}$)-space and storing the desired filtered thermochemical variables ($\overline{f}$ and/or $\tilde{f}$) in a tabulated form in that four-dimensional grid. Due to the typically steeper gradients in this area, a quadratic spacing could be chosen for the two variances ($\widetilde{c''^2}, \widetilde{Z''^2}$).

Step 4. Solution stage

Now, the tabulated FM database may be connected to the OpenFOAM CFD solver. In addition to the momentum and mass balance equations, the CFD solver also solves the transport equations for $\tilde{c}, \tilde{Z}, \widetilde{c''^2}, \widetilde{Z''^2}$ as in [38]:

Mass

$$\frac{\partial \overline{\rho}}{\partial t} + div(\overline{\rho}\tilde{\boldsymbol{u}}) = 0 \tag{3.30}$$

Momentum

$$\frac{\partial \overline{\rho}\tilde{\boldsymbol{u}}}{\partial t} + div(\overline{\rho}\tilde{\boldsymbol{u}}\tilde{\boldsymbol{u}}) + \nabla \overline{p} - div\left(\underline{\overline{\boldsymbol{\tau}}} - \overline{\rho}(\widetilde{\boldsymbol{u}\boldsymbol{u}} - \tilde{\boldsymbol{u}}\tilde{\boldsymbol{u}})\right) = 0 \tag{3.31}$$

Filtered mixture fraction

$$\frac{\partial \overline{\rho}\tilde{Z}}{\partial t} + div\left(\overline{\rho}\tilde{\boldsymbol{u}}\tilde{Z}\right) = div\left(\overline{\rho}D_{\text{eff}}\nabla\widetilde{Z}\right) \tag{3.32}$$

(Subgrid) Variance of the mixture fraction

$$\frac{\partial \overline{\rho}\widetilde{Z''^2}}{\partial t} + div\left(\overline{\rho}\widetilde{\boldsymbol{u}}\widetilde{Z''^2}\right) = div\left(\overline{\rho}D_{\text{eff}}\nabla\widetilde{Z''^2}\right) - 2\overline{\rho}\tilde{\chi}_{Z,\text{sgs}} \\ + 2\overline{\rho}\frac{\nu_t}{\text{Sc}_t}|\nabla\widetilde{Z}|^2 \tag{3.33}$$

Filtered progress variable

$$\frac{\partial \overline{\rho}\tilde{c}}{\partial t} + div\left(\overline{\rho}\tilde{\boldsymbol{u}}\tilde{c}\right) = div\left(\overline{\rho}D_{\text{eff}}\nabla\tilde{c}\right) + \overline{\dot{\omega}_c^*} \tag{3.34}$$

(Subgrid) Variance of the progress variable

$$\frac{\partial \overline{\rho}\widetilde{c''^2}}{\partial t} + div\left(\overline{\rho}\widetilde{\boldsymbol{u}}\widetilde{c''^2}\right) = div\left(\overline{\rho}D_{\text{eff}}\nabla\widetilde{c''^2}\right) - 2\overline{\rho}\tilde{\chi}_{c,\text{sgs}} \\ + 2\overline{\rho}\frac{\nu_t}{\text{Sc}_t}|\nabla\tilde{c}|^2 + 2\left(\overline{c\dot{\omega}_c^*} - \tilde{c}\overline{\dot{\omega}_c^*}\right) \tag{3.35}$$

where ν and ν_t are the filtered molecular and subgrid-scale viscosities respectively (the former retrieved from the 4-D manifold and the latter computed with the One-Equation model). D_{eff} is the effective mixture diffusivity modelled as $D_{eff} = \tilde{D} + \nu_t/Sc_t$, where Sc_t is a turbulent Schmidt number and $\tilde{D} = \tilde{\nu}/Sc$ is the filtered molecular diffusivity. The subgrid-scale scalar dissipation rate (SDR) of the mixture fraction is modeled as $\bar{\rho}\tilde{\chi}_{Z,\,\text{sgs}} = C_Z\bar{\rho}\,(\nu_t/\Delta^2)\,\widetilde{Z''^2}$ where C_Z is a constant and Δ is the LES-filter width. As explained in [38], this model is inadequate for the progress variable hence the one presented in [38] is used. The same work [38] explains in detail also the modeling of $\overline{\dot{\omega}_c^*}$.

In the present work, also the total enthalpy (i.e. sensible + formation) is transported through solving the balance equation (3.36) (together with equations (3.30), (3.31), (3.32), (3.33), (3.34), (3.35)), and not retrieved from the look-up table, in order to have better estimations:

$$\frac{\partial \bar{\rho}\tilde{h}}{\partial t} + div(\bar{\rho}\widetilde{\boldsymbol{u}}\tilde{h}) = div\left[\bar{\rho}\left(\frac{\tilde{v}}{\text{Pr}} + \frac{\nu_t}{\text{Pr}_t}\right)\nabla\tilde{h}\right] + \frac{\overline{Dp}}{Dt} \tag{3.36}$$

Note that in order to include the compressibility effects in the simulation, the Favre-filtered transport equation for the total enthalpy including the pressure effect is considered. Pr and Pr_t are the laminar and turbulent Prandtl numbers (both set to 0.7) and $\dfrac{\overline{Dp}}{dt}$ is the filtered substantial derivative of pressure, given by: $\dfrac{\overline{Dp}}{dt} \simeq \dfrac{\partial\overline{p}}{\partial t} + \tilde{\boldsymbol{u}}\cdot\nabla\overline{p}$.

The remaining term $\overline{c\dot{\omega}_c}$ and other thermochemical quantities, such as $\tilde{Y}_k$, the mixture-averaged $\tilde{c}_p$, and enthalpy of formation $\tilde{h}_f^0$, are retrieved from the look-up table (i.e. the 4-D manifold). The temperature is calculated using $\tilde{T} = T_0 + (\tilde{h} - \tilde{h}_f^0)/\tilde{c}_p$ where $T_0 = 298.15[K]$ and $\tilde{h}$ (sensible plus formation) is obtained from equation (3.36). that takes into account compressible effects.

The CFD solver will numerically solve the above-mentioned ten equations (instead of the filtered N+6: mass 1x, momentum 3x, species Nx, energy 1x and equation of state 1x): (3.30), (3.31), (3.32), (3.33), (3.34), (3.35), (3.36), and the equation of state (2.51); where the turbulence model used is the One-Equation model previously analyzed (for the closure of $\overline{\rho}(\widetilde{\boldsymbol{u}\boldsymbol{u}} - \tilde{\boldsymbol{u}}\tilde{\boldsymbol{u}})$).

Tetra-linear interpolation on the tabulated values is used to retrieve the data from the manifold for certain values of the four control variables [46]. Moreover, two additional (filtered) transport equations are solved for CO and NO in order to improve the prediction of their mass fractions, which are slower to produce and consume than those of the other species. Their filtered source term is obtained from the FM database, for example,

for nitric oxide: $\overline{\dot{\omega}_{NO}} = \dot{\omega}_{NO}(\tilde{c}, \tilde{Z}, \widetilde{c''^2}, \widetilde{Z''^2})$. In this way, the manifold only provides information on the production and consumption of these species; the total amount of these species, instead, is calculated using all of the transport events. This strategy has produced better forecasts of the nitric oxide mass fraction [47].

4 | Swirl-flows and Emissions

Swirling flows find extensive utilization across a diverse spectrum of industrial applications [48]. In instances when there is no chemical reaction occurring, notable uses may be observed in various equipment such as heat exchangers and cyclone separators. Swirlers are extensively employed in combustion systems, including but not limited to gas turbines, industrial furnaces, boilers, and several other practical heating devices, to facilitate the process of combustion. The use of swirl in flow and combustion processes produces notable and diverse effects that encompass several areas of interest, such as aerodynamics, mixing, flame stability, combustion intensity, and the emission of pollutants.

Regarding combustion, the geometric approaches to flame stabilization rely on enhancing the residence time of reactive gases. This may be achieved by the implementation of either a bluff-body burner, which exploits the wake effect, or a swirl burner, which utilizes the flow rotation of reactants. Alternatively, a mixture of these two processes can be employed.

The utilization of swirl generators has played a pivotal role in the development of novel apparatuses that effectively mitigate emissions, enhance stability, and expand the blow off limits. The utilization of swirling flows is a widely recognized method for enhancing turbulent flame speed, thereby reducing the size of the combustor while maintaining the same thermal power output. Additionally, swirling flows enhance the mixing of reactants, leading to reduced emissions and increased power density [27].

4.1. Swirl-flows

There exist several methods for generating the rotation of a fluid flow. There are three primary groups into which they might be classed:

- The implementation of fins that deflect the axial flow in a tangential manner, commonly referred to as a swirler, is being utilized. The utilization of this device is commonly observed in industrial systems due to its inherent simplicity, particularly in the context of gas turbines. Nonetheless, the use of fins in the design presents notable head losses, and the intensity of the swirl is limited (design of fins).

- Rotating mechanical devices that induce a rotating motion to the fluid as it traverses through them.

- Tangential injection refers to the introduction of a portion or the entirety of a fluid amount into a primary duct. The magnitude of the vortex is then ascertained by evaluating the proportionality between the tangentially injected flow and the axially injected flow.

The examined combustor incorporates the utilization of a swirler.

The rotating flow can be characterized by a dimensionless number, the Swirl number, that is defined as:

$$Sw = \frac{G_\theta}{RG_x} = \frac{\int_0^R (V_\theta r)(\rho U 2\pi r)dr}{R\int_0^R U(\rho U 2\pi r)dr} \tag{4.1}$$

where $G_\theta = \int_0^R (V_\theta r)(\rho U 2\pi r)dr$ is the axial flux of angular momentum and $G_x = \int_0^R U(\rho U 2\pi r)dr$ is the axial flux of axial momentum and R is the exit radius of the burner nozzle. The higher the Sw, the more intense the swirling of the flow.

4.1.1. Vortex Breakdown and Precessing Vortex Core

In order to demonstrate the influence of swirl number on the flow structure, the axial velocity distribution of two jets, one exhibiting a small swirl and the other a greater swirl, is depicted in Figure 4.1. The observation of a "wakelike" feature in the central region of the flow is significant in the case of the more intense swirl. The existence of swirling in a fluid flow gives rise to instability and mechanisms of disturbance propagation that are different from those caused by shear forces. Swirling flows display a diverse range of behaviors that are dependent upon factors such as geometry, swirl number, Reynolds number, and several other characteristics. It is important to note that the outcomes of these flows are extremely dependent on the exact configuration being considered.
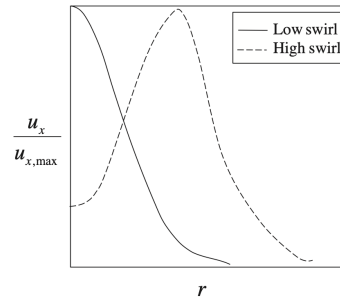
Figure 4.1: Qualitative depiction of radial variation in axial velocity profiles at low and high swirl numbers showing wakelike axial velocity profile at jet centerline that occurs at high swirl numbers [49].

Figure 4.2 shows the structure of a swirling flow in an annular combustor like the TUDelft's one:
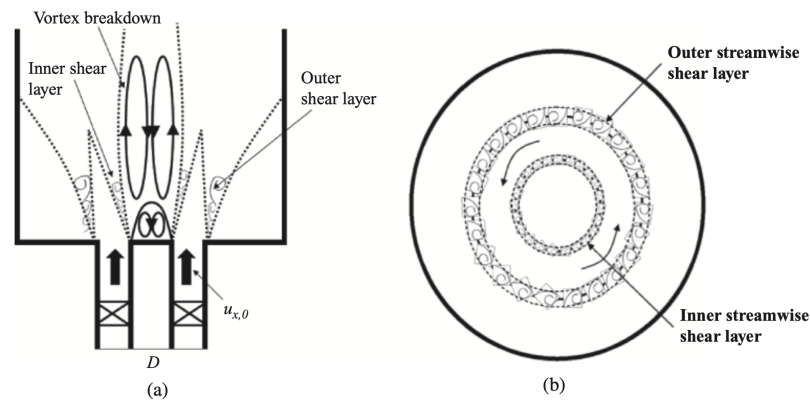
Figure 4.2: swirling structure in an annular combustor arrangement viewed from the (a) side and (b) top [49].

The flow structure is significantly influenced by the degree of swirl, denoted as Sw. Quantitative distinctions may be observed between non-swirling flows and flows with low swirl numbers. For instance, a rise in the spreading rate can be observed as the swirl number increases. Nonetheless, their time-averaged characteristics exhibit analogous quantitative features. The primary characteristic linked to low swirl flows is the presence of an azimuthal velocity component. As the swirl number grows, a range of helical instabilities manifest, with their shape and topology being dependent upon the Reynolds number [50].

The presence of vortex breakdown (VB) is a notable characteristic in high swirl number flows, where it is observed as a stagnation point inside the flow. The stagnation point is then succeeded by a zone characterized by reverse flow, as seen in Figure 4.3. The

outside flow, which is not included into the recirculating bubble, undergoes acceleration as it moves around the bubble. Indeed, from the perspective of the remaining flow, this recirculating bubble resembles an obstruction in the time-averaged flow to some degree. The phenomenon of vortex breakdown may be anticipated by the examination of a rotating, axisymmetric fluid using a steady state analysis. The flow below a certain swirl number, denoted as Sw_A, exhibits only one steady state solution characterized by a unidirectional axial flow. The vortex breakdown state occurs when the flow holds a single, stable steady solution with a negative flow velocity on the flow axis, specifically when the swirl number exceeds a certain threshold, denoted as $Sw > Sw_B$. The flow can in an intermediate hysteresis regime $Sw_A < Sw < Sw_B$, depending on initial conditions.
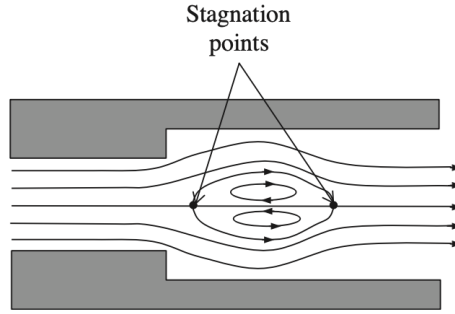
Figure 4.3: Schematic of the time-averaged flow field in a bubble type vortex breakdown field [49].

To provide an illustration, let us consider these boundaries for the velocity profile of the "Q-vortex" as outlined by the study [51].:

$$\frac{u_{x,0}}{u_{b,0}} = 1 + \frac{2\chi}{1-\chi} \exp\left(-\frac{5}{4}\left(\frac{r}{a_{\text{core}}}\right)^2\right) \tag{4.2}$$

and

$$\frac{u_{\theta,0}}{u_{b,0}} = \frac{S_V}{(r/a_{\text{core}})} \frac{\left(1 - \exp\left(-\frac{5}{4}\left(\frac{r}{a_{\text{core}}}\right)^2\right)\right)}{(1 - \exp(-5/4))} \tag{4.3}$$

where the 'backflow ratio' is defined as $\chi = \frac{u_{a,0} - u_{b,0}}{u_{a,0} + u_{b,0}}$, where $u_{a,0}$ and $u_{b,0}$ represent the axial velocities at the centerline and at large r, respectively. The parameter a_{core} is used to represent the radial position at which the angular velocity $u_{\theta,0}$ reaches its maximum value, hence determining the radius of the vortex core. Figure 4.4 depicts several velocity profiles as examples.
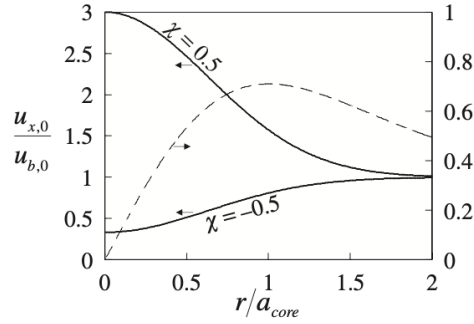
Figure 4.4: Axial and azimuthal velocity profiles used for vortex breakdown calculation, using $S_V = 0,71$ for $u_{\theta,0}$ plot [49].

The computed vortex breakdown boundaries are shown in figure 4.5, [51]. These limits are displayed as a function of velocity-based swirl number, Sw_V, although lines of constant momentum-based swirl number, Sw_m, are shown for reference. For jet flows and flows with smaller vortex cores, vortex breakdown occurs with lower swirl numbers. Wake flow breakdown requires higher swirl numbers.
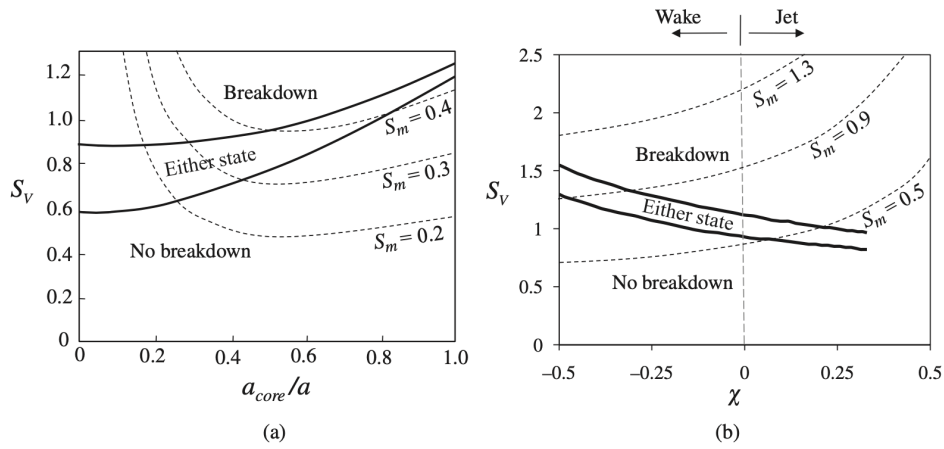
Figure 4.5: Dependence of vortex breakdown boundaries upon (a) the ratio of vortex core to pipe radius, a_{core}/a for jet flow where $\chi = 1/3$ and (b) backflow ratio, χ, at a fixed value of $a_{core}/a = 0,56$ [49].

The bifurcation in time-averaged flow characteristics with increasing swirl number may be explained by examining the dynamics of the azimuthal flow vorticity (see figure 4.6).
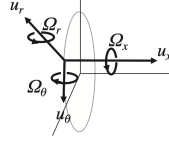
Figure 4.6: Coordinate system used in the discussion of vortex break-down mechanisms.

The azimuthal vorticity, Ω_θ, is of relevance since it may create a velocity with a negative axial component. Summary of the concept: A swirling flow with axial vorticity, Ω_x, is affected by radial flow disturbance, u_r, which stretches and tilts the axial vorticity, resulting in negative azimuthal vorticity, Ω_θ.

This causes the on-axis flow, u_x, to decelerate, being $du_x/dx < 0$. Flow continuity causes a positive du_r/dr, a bigger radial velocity, u_r, and a stronger expansion effect. This interaction may result in a stagnation point and reversal of flow along the vortex axis.

The formation of the central recirculation zone could also be explained from the angular momentum conservation's perspective. In particular, centrifugal forces associated with the rotational motion of the fluid generates a radial pressure gradient of the form (4.4):

$$\frac{\partial p}{\partial r} = \frac{\rho V_\theta^2}{r} > 0 \tag{4.4}$$

This implies the existence of a region of significantly low pressure along the central axis of the swirling flow within the mixing tube. Upon reaching the inlet of the combustion chamber, the jet is inclined to undergo expansion due to sudden increases in the area of the cross section. Nevertheless, as the flow continues to rotate, the non-zero radial pressure gradient stil exist. The tangential velocity along the centerline of the jet will decrease linearly with the radius due to the conservation of angular momentum. This conservation is expressed by the equation $\mathbf{L} = \mathbf{r} \times (\rho dV \cdot \mathbf{U}) = \rho dV \cdot rV_\theta = const$, where $\mathbf{L}$ represents the angular momentum of a fluid element volume relatively to a pole on the centerline. This implies (4.5):

$$\frac{\partial}{\partial x}\left[\frac{\partial p}{\partial r}\right] = \frac{\partial}{\partial x}\left[\frac{\rho V_\theta^2}{r}\right] < 0 \tag{4.5}$$

This indicates that the low pressure along the centerline is decreasing moving towards further axial locations, since the pressure at the boundary of the jet is predetermined and remains constant. As a consequence, the negative axial component of the pressure gradient, namely $\dfrac{\partial p}{\partial x}$, generates a reverse flow, which pushes gases towards the burner.

In general, the structure that is generated can be described as a toroidal recirculation zone, wherein two stagnation points serve as boundaries for the enclosed reverse flow. It is evident that an increased swirl number, while maintaining the same axial momentum, leads to higher tangential velocities, thereby resulting in a more intense recirculation zone. This can be attributed to the fact that the azimuthal component of the velocity is squared in equation (4.4).

Vortex breakdown is influenced by several factors, including Reynolds number, swirl number, upstream velocity profile, geometry, pressure gradient, and upstream and downstream boundary conditions. The flow structure in swirling flows is significantly influenced by downstream flow properties, for example the nozzle contraction ratio [49]. In addition, area expansions, like the step area variation in fig.4.3, significantly impact swirling flows. An example of this phenomenon is the non-continuous relationship between the spreading angle of the flow and the area expansion ratio while passing around the breakdown bubble.

It is important to acknowledge that combustion triggers the vortex breakdown: Combustion-induced vortex breakdown (CIVB) refers to a particular vortex breakdown that arises as a consequence of the thermal energy release resulting from combustion. The heat release may induce the expansion and acceleration of the fluid, resulting in the development of a low-pressure zone in the core of the vortex. Subsequently, the presence of this zone of reduced pressure has the potential to initiate the phenomenon known as vortex breakdown.

Next, we proceed to examine the dynamic nature of the area where the flow recirculates, referred to as central recirculation zone (CRZ). As previously mentioned, a prominent characteristic of vortex breakdown is the existence of a flow stagnation point located at the beginning of the bubble. The stagnation point has the potential to remain at the flow centerline, which is known as axisymmetric breakdown. Alternatively, it may deviate from the centerline and undergo rotational movement around it, which is referred to as spiral breakdown. Within the CRZ, the fluid motion exhibits characteristics of both non-steadiness and non-axisymmetry. The fluid that is entrained into the bubble undergoes an emptying and filling process of the bubble, that takes place in its downstream region. Furthermore, it should be noted that the rotational motion does not occur instantly around the geometrical centerline. In contrast, the location with zero azimuthal velocity is situated away from the center, and this particular point undergoes rotational motion around the geometric center, as seen in figure 4.7. The location at which the azimuthal velocity is zero is often known as the precessing vortex core (PVC).
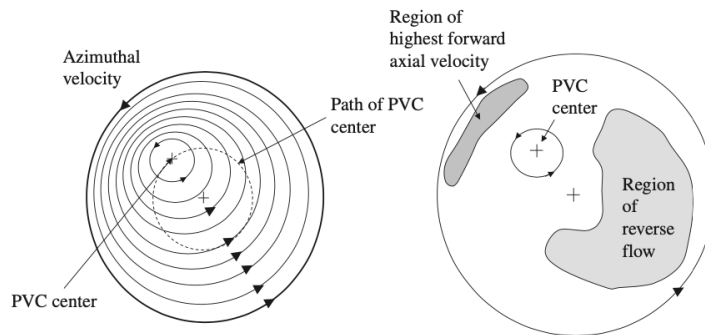
Figure 4.7: Sketch of instantaneous (a) azimuthal and (b) axial velocity inside the vortex breakdown bubble showing precessing vortex core (PVC) [49].

The rotational frequency of the PVC scales with a Strouhal number, which is calculated based on the axial flow velocity and the diameter of the pipe. The alignment of the positive and negative axial flow velocity areas in the center of the PVC, as shown in the figure, may not always be opposed to each other. Additionally, the degree of offset between these regions changes along the axial direction. As a consequence, a helical pattern emerges in the instantaneous axial flow velocity. In conclusion, it is crucial to distinguish the PVC from other helical shear flow patterns that may coexist, such as those arising from shear layer instabilities.

A significant modification of these flow characteristics may be seen in swirling flows with combustion. The zone of vortex breakdown undergoes changes in its shape and size, resulting in substantial effects on the spreading angle and velocity of the outer flow circumnavigatin the bubble. The observed discrepancies are frequently credited to the influence of gas expansion on the inner vortical structures. Due to the expansion of gas inside the flame, the flowfield situated downstream of the flame exhibits elevated axial velocities, while experiencing little changes in azimuthal velocity. This translates into a significant decrease in the swirl number.

The presence of a central recirculation zone may provide significant advantages in terms of enhancing the mixing and preheating of fuel and air. However, it is important to note that this phenomenon can also lead to equipment damage due to the resonances generated by the interplay between the coherent structures formed and natural system resonances and combustion induced oscillations. These instabilities include PVC.

4.2. Swirl effects on flames

Based on the findings of Beèr and Chigier (Beer, n.d.), it has been shown that flows characterized by a low swirl number ($Sw = 0.6$) do not exhibit any recirculation of the flow (see figure 4.8).

(1) − Low   (2) − Intermediary S_n (3) − High S_n
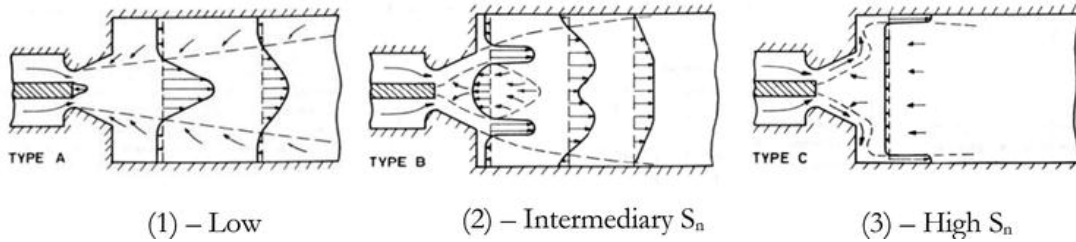
Figure 4.8: Swirl effect on flames. (1) Low Sw, (2) Intemediary Sw, (3) High Sw.

The swirl increases ambient fluid entrainment and decreases flow axial velocity. Axial velocity radial profiles remain Gaussian when Sw is below 0.5 (1), lifting the flame behavior. When approaching $Sw = 0.6$ (2), where the flame is stabilized closer to the burner in the recirculation zone rich in fresh gases, velocity maximum deviates from the axis and turbulence increases. With increasing swirl number (3), jet opening and entrained mass flow rise continually.

A recirculation zone appears in the main flow at 0.6 swirl intensity. The swirl intensity affects the size and location of the recirculation zone [52, 53].

Fresh and flue gases mixes in the recirculation zone. In addition, swirl enhances gas entrainment and raises flame blow-off limit [54, 55].

The interaction of hot products and active chemical species with entering fresh gases (air and fuel) in this zone helps sustaining the flame. Fresh gases in the center recirculation zone stabilize the flame next to the burner outlet due to their low speed [54, 56]. A corner external recirculation zone may be created downstream of the backward-facing step [27].

Swirling reacting flows have numerous benefits that are well-known and investigated, including improved flame stabilization through vortex breakdown, due to central recirculation zone (CRZ), and enhanced turbulent mixing through precessing vortex core (PVC) [54, 55, 57]. Cozzi et al. [58] used stereo-particle image velocimetry (S-PIV) to study the initial region of a swirling gas jet on a model burner in isothermal air jets. The objective of their research was to investigate the occurrence of vortex breakdown, the central recirculation zone (CRZ), and the precessing vortex core (PVC).

4.3.　Swirl effects on pollutant emissions

As previously stated, the use of swirlers in the combustion chamber serves to augment turbulence and promote the thorough mixing of fuel and air. This, in turn, results in improved combustion efficiency and a subsequent decrease in emissions. Consequently, this phenomenon may have an impact on the temperature of the flame and result in a decrease in the release of harmful substances, particularly in scenarios that need minimal levels of nitrogen oxide (NOx) emissions.

Schmittel et al. [59] demonstrated that the use of swirl in non-premixed combustion has the potential to effectively mitigate the release of pollutant emissions, namely nitrogen oxides. The introduction of a swirling motion and subsequent enhancement of reactant mixing results in a reduction in flame temperature, thus leading to a decrease in the generation of nitrogen oxides (NOx) through the Zeldovich mechanism. Furthermore, when the strength of the swirling is significant, augmenting the Sw leads to a decrease in the amount of time spent in high-temperature regions, which has the consequence of restricting the generation of nitrogen oxides (NOx). Nevertheless, it is vital to identify an optimal swirling intensity that strikes a balance between mitigating pollutant emissions and maintaining a safe distance between the flame burner in order to prevent the occurrence of flashback. The research conducted by Coghe et al. [60] examined the performance of a lean natural gas burner with a fuel-air equivalence ratio of 0.69. The findings revealed that the reduction of nitrogen oxides (NOx) may reach up to 30% within a range of swirl numbers between 0.7 and 0.82.

The impact of the swirl number on the emissions of NO_x and CO was investigated by Boushaki et al. [61] and Nazim et al. [62] as documented in their respective studies. It was discovered that when the swirl number is 1.4, the EICO rate (i.e. CO emission index, indicating the ratio of CO mass exiting the engine to the mass of fuel intake) is marginally lower compared to a swirl number of 0.8. The researchers observed that the intensity of the swirl may have the tendency to augment the mixing process and prolong the duration of stay inside the reaction zone. This, in turn, facilitates the conversion of CO to CO_2. With regards to the emissions of nitrogen oxides, the researchers observed that an increase in the swirl number has a tendency to decrease the creation of EINOx, especially when the oxygen rate is below 27

In their study, Burguette and Costa [63] conducted an assessment of the impact of swirl intensity on NO_x emissions by examining the angle of the blades that make up the swirler. The researchers discovered that the NO_x rate is the highest at an angle of 45°, whereas NO_x emissions fall when the angle deviates from 45°, either lower or higher. The

authors provide an explanation for these findings based on the observation that a recirculation zone starts at a 45° angle. This leads to an increase in residence time in proximity to the burner, where the temperature is higher, with a subsequently higher generation of NO_x. Cozzi and Coghe [64] conducted a study on the emissions of nitrogen oxides (NOx) in a coaxial swirling flame fueled by natural gas. According to their findings, the intensity of swirl significantly impacts non-premixed flames, resulting in greater amounts of NO_x reduction at increased swirl levels.

Swirlers have the potential to enhance the overall efficiency of a combustion system. Enhancing flame stability and combustion quality may result in increased thermal efficiency and reduced operational expenses.

4.4. An operating limit of Swirl-combustors - Flashback

The use of premixed combustion has the benefit of attaining much reduced levels of nitrogen oxides (NO_x) compared to non-premixed flames. This is mostly due to the considerably lower flame temperature resulting from a significantly reduced local equivalency ratio. Nevertheless, premixed flames are prone to a phenomenon known as flashback, when the fresh mixture velocity has a component normal to the flame front which is below the turbulent flame speed, resulting in the propagation of the flame in the upstream direction ([65], see figure 4.9. This phenomenon may lead to the deterioration and subsequent shutdown of the burner.
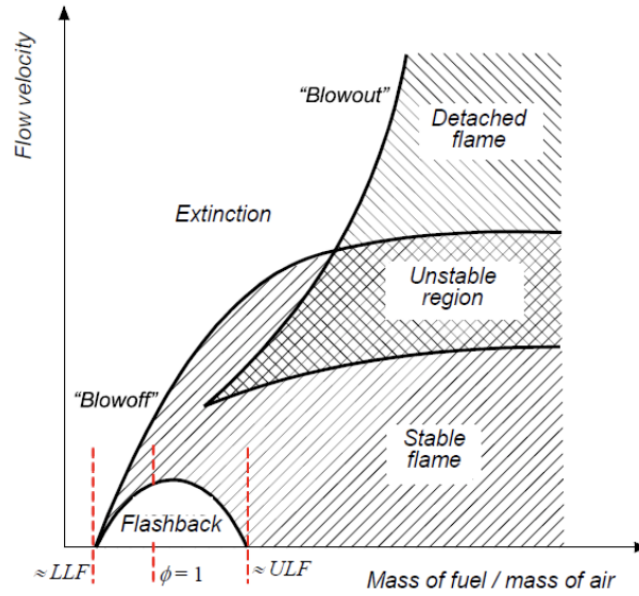
Figure 4.9: Flame stability diagram for different equivalence ratios, with the Lower and Upper limit Flashback (LLF and ULF) indicated.

Hydrogen exhibits a flame speed that is approximately five times greater than that of methane. While this mitigates the likelihood of flame blowoff, it concurrently elevates the potential for flasbback. Four different types of flashback are possible; they are described in detail below:

- *Flashback in the turbulent core.* As the turbulent flame velocity S_T surpasses the component of the flow velocity normal to the flame front, an upstream movement of the flame front occurs. S_T/S_L^0 is an increasing function with respect to the turbulent intensity u/S_L^0, where S_L^0 is the laminar flame speed and u is the rms velocity fluctuation. Additionally, as pressure and temperature rise, the value of S_T/S_L^0 rises as well. On the one hand, it is therefore preferable to conduct operations at low pressures, on the other hand, higher pressure allows for smaller combustors. When utilizing highly reactive fuels, such as hydrogen, a low-swirl burner operating at low pressures is preferred in order to decrease the turbulent flame speed. Conversely, this contradicts the criteria for sequential combustors, which habitually function under elevated pressures accompanied by substantial turbulence. One potential resolution entails diminishing the pressure and swirl in order to significantly increase the axial velocity above the turbulent flame speed. Nonetheless, such an outcome would result in diminished operational efficiency, compromised mixing, and a heightened propensity for autoignition and instability. As illustrated in figure 4.10, Eichler [66] explains that this particular form of flashback can be disregarded during typical gas

turbine operations due to the fact that the free stream velocity is typically greater than the flame speed.
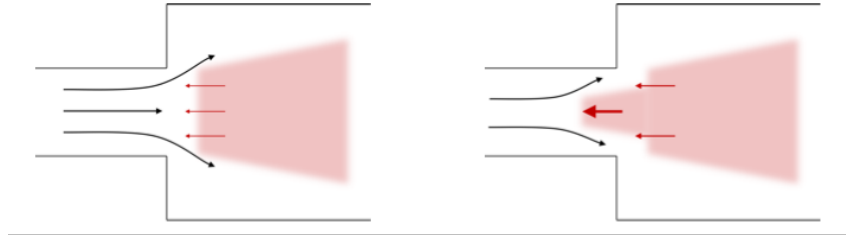
Figure 4.10: Flashback in the core flow. The red shaded area indicates the region of burned gases, red arrows correspond to flame propagation and black arrows to the flow. The size of the arrow is drawn relative to the speed (flow or flame). [67].

- *Boundary Layer Flashback (BLF).* The boundary layer is characterized by a no-slip condition: velocity in the burner decreases to zero close to the wall. The formation of a boundary layer flashback occurs when local flow velocities fall below the S_T turbulent flame speed. This results in the initiation of upstream flame propagation (refer to figure 4.11). Nevertheless, this issue is mitigated by the heat discharge from the flame towards the wall, which effectively suppresses it (i.e., the heat discharge locally reduces the flame temperature, thereby diminishing its reaction rate to the point where it ceases to exist; in other words, the combustion reactions decelerate to the extent that they cease to exist and the flame quenches). This type of flashback is more prevalent in hydrogen owing to its elevated flame velocity and reactivity, which leads to an exceptionally small quenching distance (i.e. flame sustains without quenching even in pipes with small diameters, where heat dissipation becomes more important with respect to heat release). This is the primary flashback mechanism for low-turbulence and low-swirl flows, described in more details in [68].
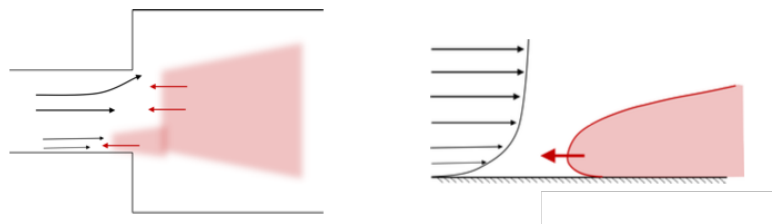
Figure 4.11: Boundary-layer flashback. The shading and arrows are the same as in figure 4.10. [67].

- *Flashback due to combustion instabilities.* The flashback in question causes both boundary layer and core layer flashbacks, as illustrated in figure 4.12. These flashbacks are caused by fluctuating pressure pulsations resulting from unsteady heat release rates of the mixture, an lead to periodic occurrences of the flashback itself [69]. Typically, they result from two mechanisms: fluctuations in the local equivalence ratio and vortex shedding. Acoustic oscillations in the mixing tube are the source of local equivalence ratio fluctuations. Vortex shedding occurs when rotating flows generate large coherent vortical structures through vortex breakdown. Alterations in heat release result from both mechanisms, which subsequently generate oscillations in flow velocity and culminate in the formation of flashbacks at low frequencies. In order to mitigate this form of flashback, the elimination of low-frequency pressure fluctuations is imperative. Flashback can therefore be eliminated through the use of active control that impedes thermoacoustic oscillations [70].
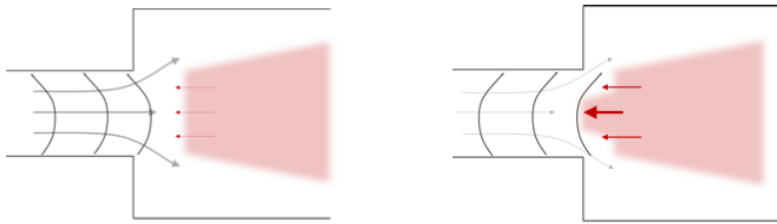
Figure 4.12: 1.6: Flashback - combustion instability-induced. The shading and arrows are the same as in figure 4.10. [67].

- *Flashback due to Combustion Induced Vortex Breakdown (CIVB).* Flashback may occur along the centerline of a swirl-stabilized burner, which is typical of gas turbines burners. This can be attributed to the upstream propagation of the recirculation zone, as illustrated in figure 4.13. This flashback mechanism is more hazardous in the case of hydrogen as a result of the increased flame speed and chemical kinetics, which increase the likelihood of this type of flashback. Locally quenching the flame prevents it from propagating upstream, despite the movement of the recirculation zone, which proves to be a crucial aspect of this mechanism. Hydrogen's elevated resistance to quenching, because of its small quenching distance, indicates an increased likelihood of experiencing this form of flashback. Also influencing this is the swirl number, as a lower swirl number is more effective at preventing this instability. CIVB flashback can be avoided through a proper aerodynamic burner design [11].
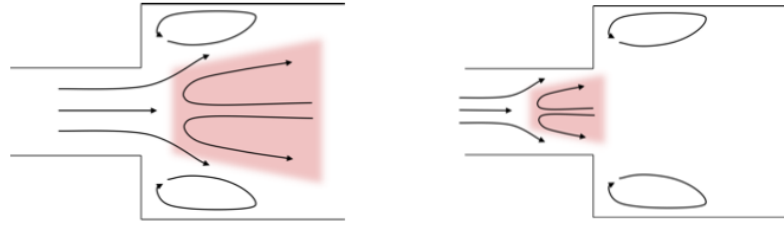
Figure 4.13: 1.5: Flashback - combustion-induced vortex breakdown (CIVB).The flow enters from the mixing tube on the left into the combustion chamber. The shading and arrows are the same as in figure 4.10. [67].

In summary, a number of factors contribute to the facilitation of flashback, which includes elevated swirl number, high fuel reactivity, high equivalence ratio, and low axial velocity.

Air injection provides great margins of operation stability due to the fact that the diameter of the air nozzles can be altered while the combustor is in operation in order to satisfy flame stabilization [69]. Specifically, the LLF is impacted by axial air injection, which modifies the flashback mechanism generated by induced vortex breakdown flashback (CIVB). The central air injection specifically enhances flame stability through its influence on the aerodynamic of the flow field located downstream of the burner mouth. It decreases the axial velocity defect at the recirculation zone's apex, which is one of the primary causes of CIVB flashback.

4.5. NO_x formation mechanisms and implementation in OpenFOAM

In this section, chemical routes of formation of NO_x are discussed. Furthermore, the implementation of the way the mass fraction of NO_x is calculated in this work is shown.

4.5.1. NO_x formation mechanisms

The issue of carbon dioxide (CO2) and pollutant emissions from combustion processes, including unburned hydrocarbons (UHCs), carbon monoxide (CO), and oxides of nitrogen (NOx), has become a growing concern in recent decades. NO_x is a contributor to stratospheric ozone depletion and a precursor to chemical pollution, whereas CO_2 is considered a significant greenhouse gas. The development of technologies that reduce the release of these critical species into the atmosphere necessitates comprehension and regulation over their formation mechanisms. Typically, the formation of NO_x occurs at a slower time

scale with respect to fuel oxidation reactions. Due to the combination of this slow forma-
tion process and the short residence periods encountered in modern combustion devices,
NO_x is typically emitted at concentrations well below equilibrium levels.

NO has the highest concentration at the end of combustion among the most prevalent
nitric oxides ($NO2$, NO, and N_2O), comprising around 90% of the total NO_x in natural
gas [71]. Additionally, N_2O is noteworthy for its powerful greenhouse effect. Effectively
reducing the formation of NO_x requires the application of premixed lean-burn technology,
which is stabilized by swirler. Certainly, emission abatement is imperative due to the
constantly growing restrictions established on pollutant emissions.

Nitric oxide is a significant minor species during combustion. The detailed nitrogen
chemistry implicated in methane combustion, incorporated in GRI-Mech 3.0, is available
in the reference [72].

When nitrogen-free fuels are burned, nitric oxide is produced through four chemical path-
ways involving N_2 from the atmosphere:

- *The Zeldovich (or thermal) mechanism.* This mechanism dominates at high temper-
  ature combustion, namely $1800[K]$ like happens in gas turbines, over a fairly wide
  range of equivalence ratios [72]. This mechanism is unimportant at temperatures
  below $1800[K]$, due to the fact that the rate-limiting reaction ($N + NO \longleftrightarrow N_2 + O$)
  has a large activation energy [16]. The thermal or Zeldovich mechanism consists of
  two chain reactions: $O + N_2 \longleftrightarrow NO + N$ and $N + O_2 \longleftrightarrow NO + O$, which can be
  extended by adding the reaction $N + OH \longleftrightarrow NO + H$. In general, this mechanism
  is coupled to the fuel combustion chemistry through the O_2, O, and OH species.
  However, in processes where the fuel combustion is complete before NO formation
  becomes significant, the two processes can be uncoupled. In this case, if the rel-
  evant timescales are sufficiently long, one can assume that the N_2 , O_2 , O, and
  OH concentrations are at their equilibrium values and N atoms are in steady state.
  These assumptions greatly simplify the problem of calculating the NO formation.
  If we make the additional assumption that the NO concentrations are much less
  than their equilibrium values, the reverse reactions can be neglected. This yields
  the following rather simple rate expression:

$$\frac{\mathrm{d}[NO]}{\mathrm{d}t} = 2k_f[O]_{eq} [\ N_2]_{eq} \tag{4.6}$$

  where $k_f = 1.8 \cdot 10^{11} \cdot exp(-38370/T[K])\ [m^3/(kmol \cdot s)]$ is a steeply increasing
  function of temperature when $T > 1750[K]$. An effective way of thermal NOx

reduction is water injection: the humidity promotes the reaction $O + OH \rightarrow OH + OH$, which suppresses the O atom concentration. This scarcity in turn reduces the production of NOx by this pathway as a complementary effect to the temperature reduction.

- *The Fenimore (or prompt) mechanism.* The Fenimore mechanism is connected to the chemistry of hydrocarbon combustion and is crucial in rich combustion due to the different behavior of hydrogen cyanide conversion (HCN). It contributes marginally to overall emissions and exhibits little dependence on temperature. The absence of CH radicals in the combustion of pure hydrogen makes this pathway inapplicable to hydrogen. *prompt NO* comes from the rapid formation of NO, which occurs primarily in the fuel-rich region of the flame, on time scales shorter than those of the Zeldovich mechanism.

- *The $N_2O - intermediate$ mechanism.* This pathway is critical for the production of NO in extremely lean, low-temperature combustion processes (beginning with equivalence ratios below 0.8). This mechanism assumes significance in NO control strategies employed by gas turbine manufacturers, which involve lean premixed combustion.

- *The NNH mechanism.* It has been demonstrated that this pathway is crucial for the combustion of hydrogen and hydrocarbon fuels containing a high carbon-to-hydrogen ratio. At $1800[K]$, this pathway can increase the production of NO by an order of magnitude for methane combustion.

The use of swirl-stabilized lean-premixed technology plays an important role in both abating NO_x emissions from N_2O mechanism, by combustion at low equivalence ratio, and from Zeldovich mechanism since the swirler guarantee a very good mixing prior combustion, thus avoiding hot spots at very high temperature that would detrimentally increase the NO production. Multiple investigations have demonstrated the comparative significance of the initial three mechanisms in premixed flames, as in [73]. [16] The Zeldovich mechanism is believed to be the primary source of NO during the combustion of nitrogen-free fuel and oxygen when the temperature is high enough.

In conclusion, NO_x production is affected in a complex way by pressure, fuel-to-air ratio, temperature, and residence time.

4.5.2.   Implementation in OpenFOAM

The slow formation and its strong dependence on the flame temperature represent major difficulties for the accurate prediction of NOx. In the work of Pitsch et al [16], a model for the prediction of the nitric oxide NO formation in turbulent non-premixed flames using flamelet formulation is developed. Its performance is proved for the three relevant NO formation mechanisms, namely, *thermal*, N_2O, and *prompt* mechanisms. In this flamelet model, an additional transport equation for the NO mass fraction is solved, and the chemical source term is obtained from a flamelet tabulation. Since the consumption rate is dependent on the NO mass fraction, this term requires modeling. In particular, the proposed approach splits the reaction rate for NO into a source and a sink term contributions, that are first implemented and then retrieved from the thermochemistry tabulation. This particular proposed NO model is integrated into the flamelet model used in the present work by solving the transport equation (4.7) (to be Favre-filtered), with the assumption of equal species diffusivities:

$$\rho \frac{DY_{\mathrm{NO}}}{Dt} = \nabla \cdot (\rho \alpha \nabla Y_{\mathrm{NO}}) + \rho \dot{\omega}_{\mathrm{NO}} \tag{4.7}$$

where $\dfrac{D}{Dt} = \dfrac{\partial}{\partial t} + \mathbf{u} \cdot \nabla$ is the substantial derivative. The tabulated estimation of NO is also retained in the code for comparison purposes. The obtained results in terms of NO emissions prediction are shown in section 6.3.

[16]

4.6.   Differential diffusion

4.6.1.   Hydrogen vs Methane - thermochemical properties

Hydrogen's high energy density, zero-carbon emissions, and ability to be produced from water electrolysis using renewable energy make it a viable clean energy carrier for long-distance flights. However, its high flame temperature may produce significant NO_x. Hydrogen is a complicated fuel with unique features. High gravimetric energy density distinguishes hydrogen. It has a greater heating value (HHV) of $142[MJ/kg]$ than natural gas ($54[MJ/kg]$). However, its volumetric energy density is low, with an HHV of $0.012[MJ/l]$ compared to $0.038[MJ/l]$ for natural gas under typical circumstances. This suggests that hydrogen storage facilities must be much bigger, unless liquid storage is employed, which would be costly.

Important combustion features of hydrogen include a large flammability range of $4 - 75\%$, compared to $4.3 - 15\%$ for natural gas. Premixed lean-burn technology reduces NO_x production by using hydrogen's broad flammability range to stabilize flames under the leanest circumstances (limit $\phi = 0.1$) with the aid of a swirler.

Additional design challenges include hydrogen's strong reactivity and diffusivity, which may cause flashback, and lean premixed combustion instabilities. Hydrogen has a faster laminar flame speed than natural gas or other fuels owing to quick reaction rate and higher adiabatic flame temperature. With a diffusivity of $0.61[cm^2/s]$, hydrogen transfers more radicals upstream of the flame than methane $(D_{CH_4} = 0.22[cm^2/s])$.

Hydrogen has a higher adiabatic flame temperature, which increases NO_x generation, however certain NOx routes are not viable (Fenimore and Fuel). Due to its faster flame speed, hydrogen has a narrower flame front than natural gas. The Lewis number of hydrogen is $Le_{H_2} \simeq 0.3$, much lower than natural gas. This low number negatively impacts flame stability, as stated in section 4.6.2.

4.6.2.   An overview on hydrogen's differential diffusion

Gaseous diffusion flame modeling often assumes equivalent Schmidt values for the species' molecular diffusivities. Furthermore, the Lewis number is usually assumed to be unity, meaning heat diffusivity equals molecular diffusivity. These assumptions create a conserved scalar, the mixture fraction z, which uniquely determines species mass fractions and enthalpy when Damkohler number is high enough [74]. However, in many real combustion challenges, molecular transport coefficients vary greatly. The preferred, or differential, diffusion of H_2 in hydrogen/oxygen combustion needs to be taken into account as it plays a crucial role. It is sometimes argued that differential diffusion influence on quantities of interest may be ignored if Re is big enough, since small and large scales of turbulence are well separated with high Re values. It is reasonable to suppose that the primary variables of interest, such as average temperature and concentrations, are largely related with large turbulent scales and not affected by differential diffusion, a small scale phenomena. Nonetheless, in flows with substantial heat release, the resulting temperature increase can significantly reduce Re due to thermal increase of dynamic viscosity, and effects due to differential diffusion can be expected, even on quantities associated with the large turbulent scales [75]. Drake et al. [76] found significant effects of differential diffusion at low Reynolds numbers by measuring temperature and species concentrations in a jet flame of H2 in air.

The incorporation of detailed chemical kinetics and the subsequent ability to precisely

represent the microstructure of a flame while minimizing computational expenses have established flamelet-based tabulation approaches, such as the flamelet-generated manifold (FGM), as a widely employed technique in turbulent combustion simulations. Nevertheless, there has been little attention given to the examination and evaluation of these models in the context of fuel mixtures, such as hydrogen. One factor contributing to this phenomenon is the complex integration of differential diffusion effects into FGM, which may be particularly significant when dealing with highly diffusive fuels like hydrogen.

However, the combustor at TU Delft is examined assuming a $Le = 1$ for H_2, hence neglecting preferential diffusion, being its modeling an open problem. This implies that the adopted thermochemistry tabulation does not include the effects of differential diffusion of hydrogen. The study conducted by [77], representing an attempt to model differential diffusion using flamelets, highlights the effects of taking into account the differential diffusion in H_2/CH_4 partially premixed flames.

4.6.3. Thermo-diffusive instability: a result of differential diffusion

The combustion process is significantly influenced by thermo-diffusive instability. The cause of this instability may be attributed to the differential diffusion for both heat and species participating in the combustion process. The presence of instability may be seen in figure 4.14, whereby the flame front exhibits many convex and concave bulges and cusps directed towards the unburned gases [78]. At the bulges, the flame area is considerably greater than that of the consumed gases, resulting in a substantial heat dissipation from the flame (propelled by orange arrows) and an introduction of new gases (propelled by blue arrows). On the contrary, the reactants are scarcer at the cusp, leading to a net increase in temperature due to the cusp getting surrounded by hot flue gases. The behavior of the flame front is influenced by the inherent characteristics of the Lewis number, which gives rise to three potential outcomes depending upon its numerical value:

- *Le > 1.* In the given situation, the bulges emit thermal energy at a higher rate compared to the influx of reactants, leading to a reduction in the velocity of the flame. Conversely, a contrasting phenomena takes place near the cusps, when the heat acquired surpasses the diffusion of reactants, resulting in an augmentation in flame velocity. The outcome is a consistent procedure that guarantees a linear flame.

- *Le < 1.* In this particular case, the bulges exhibit a quick acquisition of fresh reactants in comparison to the dissipation of heat, leading to an augmentation in the velocity of the flame. In contrast, the velocity of the flame exhibits a reduction near

the points of inflection. The present flame exhibits inherent instability, resulting in the development of curvature and self-induced wrinkling, as shown by Zhang et al. [78]. The aforementioned phenomena manifests in the context of hydrogen, hence indicating that flames fueled by hydrogen exhibit thermo-diffusive instability.

- $Le = 1$. A balance is maintained between heat release and diffusion in this scenario, thereby preserving the flame structure and its parameters.

To summarize, the impact of heat diffusion alone has a stabilizing effect on flames. It causes an increase in both the rate of reaction and the flame speed in concave regions, but a decrease in both of these parameters in convex regions. This effect prevents instability when $Le = 1$. An aspect that may contribute to instability in flames is the differential diffusion of reactants, which occurs when the diffusivities D_k of the reactants vary. Reactants possessing greater diffusivities have a tendency to diffuse convex regions preferentially in comparison to the other reactants. For example, convex flames exhibit a higher equivalence ratio of hydrogen, resulting in elevated flame temperature and velocity within these regions. On the contrary, concave regions experience a reduction in these values, which induces a perturbation and renders the flame unstable.

(a) $Le < 1$ (b) $Le = 1$ (c) $Le > 1$
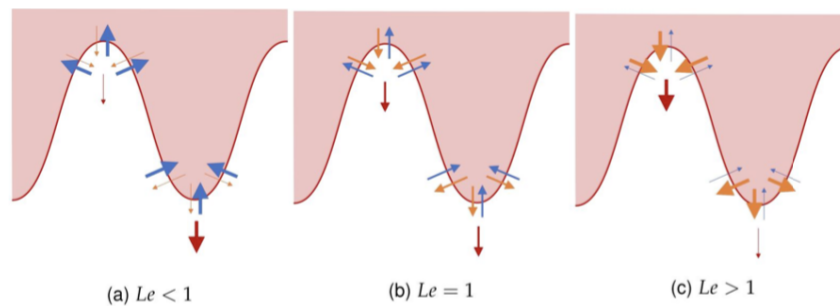
Figure 4.14: Effect of Lewis number on the flame stability. The red area represents the burned gases; the blue arrows the diffusion of species, the orange arrows the heat diffusion and the red arrows the flame propagation. The size is proportional to the importance. [67]

5 | Numerical modeling

OpenFOAM, an abbreviation for Open Field Operation and Manipulation, is a renowned open-source computational fluid dynamics (CFD) software that has been used for performing the simulations of this work. Given the high computational cost of LES, the computational resources of DelftBlue supercomputer [79], provided by Delft High Performance Computing Centre (https://www.tudelft.nl/dhpc), have been used. OpenFOAM is built upon the finite volume method (FVM), which endows it with the capability to effectively address fluid flow and heat transfer challenges through this numerical discretization approach. The finite volume method partitions the computational domain into discrete control volumes or cells, in which conservation equations are established for each.

5.1. Mesh and Choice of the grid size

TU Delft's combustor is studied numerically. Figure 5.1 shows its components:

- *Fuel ports*, allow the injection of fuel radially.

- *Air ports*, allow the radial injection of air that will reach the mixing tube either through the swirler and through the AAI, with a ratio depending on the chosen %AAI.

- *Swirler*, gives the azimuthal component to the velocity field in order to produce vortex breakdown and thus generating central recirculation zone, where the flame under lean condition can stabilize.

- *Axial Air Injection (AAI)*, for flashback prevention.

- *Mixing tube*, to enhance mixing before entering the combustion chamber.

- *Combustion Chamber*, in which lean partially premixed combustion occurs.
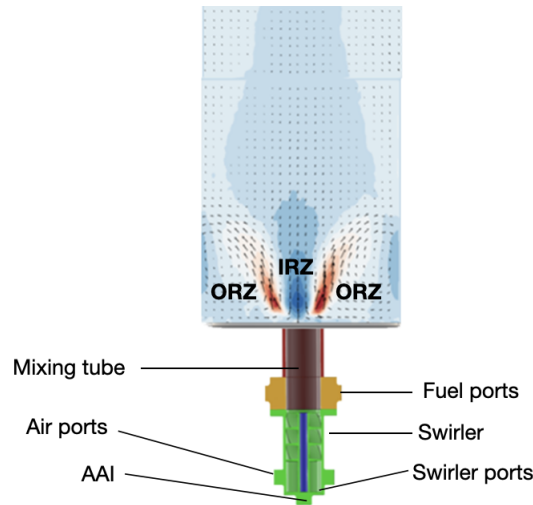
Figure 5.1: TU Delft combustor: components and sizes.

A previous work on this combustor showed that the inclusion of the swirler in the domain to simulate numerically raised unacceptably the computational time by limiting the timestep because of the fine cells that had to be used to mesh the swirler. Hence, in order to reduce the computational time without sacrifying accuracy, a turbulence inflow generator has been used to impose the flow field at the inlet of the mixing tube, thus enabling to cut the swirler out of the mesh. In particular, a LES with the swirler resolved has been performed and the flow field at the outlet of the swirler extracted. The turbulence inflow generator is able to impose a turbulent flow field at the inlet of the mixing tube respecting the statistics (i.e. average and rms) of the velocity field extracted without the need to numerically simulate the swirler. In particular, for what concern the unfueled non reactive simulations, the fluid is only air since no fuel is injected and it has been decided to start meshing from the mixing tube downstram the fuel ports, loosing accuracy because we are not solving the influence of the fuel ports on the flow field. The resulting 3D mesh, that has been previously built with Pointwise software, is shown in figure 5.2. In conclusion, the computational domain is made up of the combustion chamber and the part of the mixing tube downstream the fuel ports.
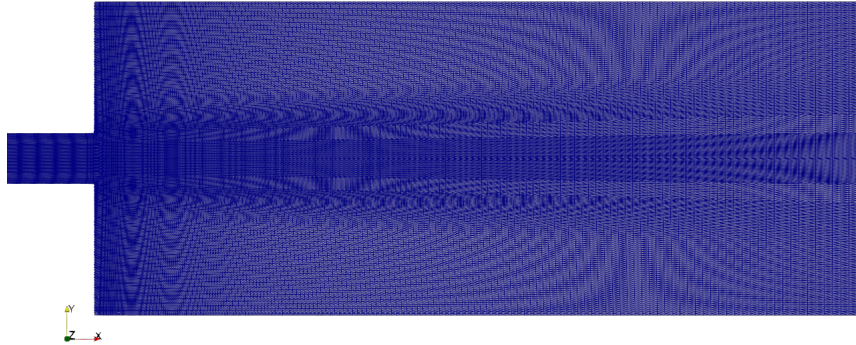
Figure 5.2: Diametral slice of the mesh.

The mesh is structured, allowing higher time steps and optimal values of both cell non-orthogonality and skewness, enhancing the accuracy of the simulations. An O-Grid is used to generate the cilyndrical geometry without retaining singularities in the domain (i.e. cells with extremely high skewness or zero volume). The level of refinement in the CRZ region is sufficient to ensure that a minimum of five cells will encompass the turbulent brush in the reactive scenario, thereby enhancing the effectiveness of the flamelet model in accurately representing the turbulent-flame interaction.

5.2. Validating mesh quality

The mesh seen in figure 5.2 consists of cells with a uniform length of $0.7[mm]$ along the x-direction in the mixing tube. In the combustion chamber, the length along the x-direction varies starting from $0.3[mm]$ at the inlet to $4[mm]$ at the outlet. The mixing tube is equipped with a highly refined mesh to effectively capture the flow field's characteristics and ensure accurate fuel and air mixing for future reactive scenarios. Additionally, the mesh is further refined at the entrance of the combustion chamber and on the corners to enhance the precision in capturing the characteristics of the central and outer recirculating zones.

The measurement of mesh quality is often assessed using the Pope criterion [17]. According to this requirement, a minimum of 80% of the kinetic energy should be resolved, often requiring the use of at least 4 to 5 cells within the integral length scale [19]. The criteria established by the Pope is computed in the following manner:

$$M(\boldsymbol{x}, t) \equiv \frac{k_r(\boldsymbol{x}, t)}{K(\boldsymbol{x}, t) + k_r(\boldsymbol{x}, t)} > 80\% \tag{5.1}$$

In the given context, K represents the turbulent kinetic energy associated with the resolved motions, k_r denotes the residual kinetic energy that is computed through solving a transport equation for the turbulence modeling, and M is measure of the turbulent resolution. It is noteworthy to emphasize that residual motion refers to the motion that occurs at a scale less than the filter-width, while sub-grid scale motion refers to the motion that occurs at a scale smaller than the grid size [19]. All these quantities are space and time dependent. According to [17], it is accepted a value of M smaller than 0.2 in order to achieve good accuracy. The variable M may take on values ranging from 0 to 1, where $M = 0$ represents the DNS (Direct Numerical Simulation) method and $M = 1$ corresponds to the RANS (Reynolds-Averaged Navier-Stokes) method. Lower values of the parameter M are indicative of a higher level of resolution for the turbulent movements. To evaluate $M(\boldsymbol{x}, t)$, it is necessary to determine the turbulent kinetic energy of the resolved movements locally in space and time, as in equation 5.2.

$$K(\boldsymbol{x}, t) = \frac{1}{2}\langle(\tilde{\boldsymbol{U}}(\boldsymbol{x}, t) - \langle\tilde{\boldsymbol{U}}(\boldsymbol{x}, t)\rangle) \cdot (\tilde{\boldsymbol{U}}(\boldsymbol{x}, t) - \langle\tilde{\boldsymbol{U}}(\boldsymbol{x}, t)\rangle)\rangle \tag{5.2}$$

and that of the residual motions $k_r(\boldsymbol{x}, t)$.

In the context of equation 5.2, the notation $\langle \cdot \rangle$ represents the operation of time-averaging. Therefore, the expression $\tilde{\boldsymbol{U}}(\boldsymbol{x}, t) - \langle\tilde{\boldsymbol{U}}(\boldsymbol{x}, t)\rangle$ corresponds to the vectorial difference between the instantaneous velocity field and the time-averaged velocity field, referred to as the fluctuating velocity field.

The distribution of variable M over the domain used for the non-reactive unfueled LES is shown in Figure 5.3. The specific LES that will be selected as best fit to experimental data in chapter 6 and retained for further analysis is shown at a time of 1.99 seconds.
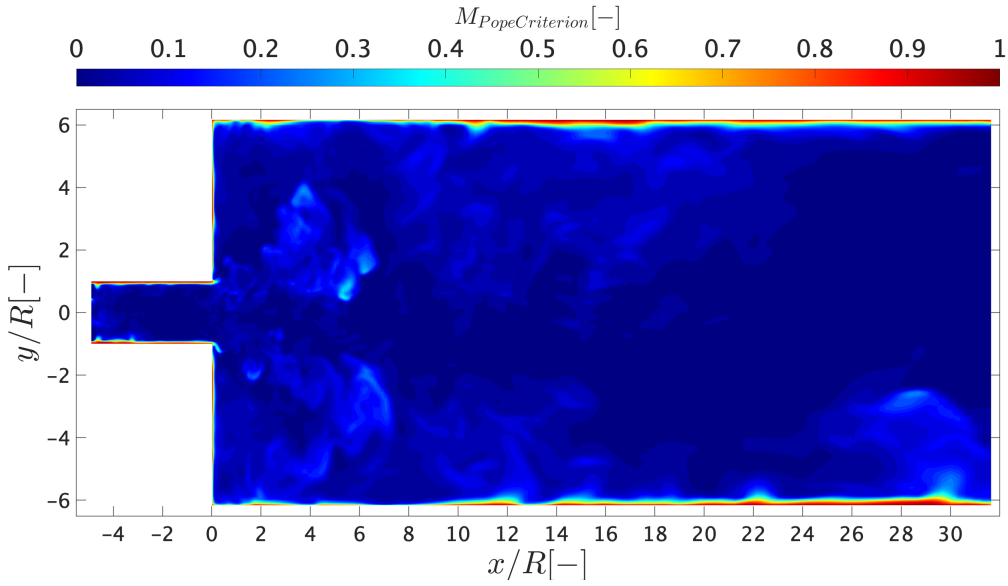
Figure 5.3: Contour of the measure of the turbulent resolution M for the $LES50\%$ that will be selected as best-fit in the chapter 6.

It is evident that over the whole domain, outside the regions where wall functions are used, the Pope requirement is reasonably fulfilled. The mesh refinement should be considered, particularly in regions where vortex breakdown occurs, in order to resolve smaller scales of turbulence. Consequently, the time step used may be constrained to maintain a Courant number below a certain threshold, as elaborated upon in section 5.7, thus adversely impacting the computational time needed for the LES.

The same considerations apply to the non-reactive and reactive methane cases, of which the measure of turbulent resolution M is shown in figure 5.4. Furthermore, it is important to think about the refinement of fuel ports, while also considering the trade-off associated with the implications on the Courant number, given the high bulk velocities resulting from the small cross-sectional area.

(a) Non-reactive methane case   (b) Reactive methane case
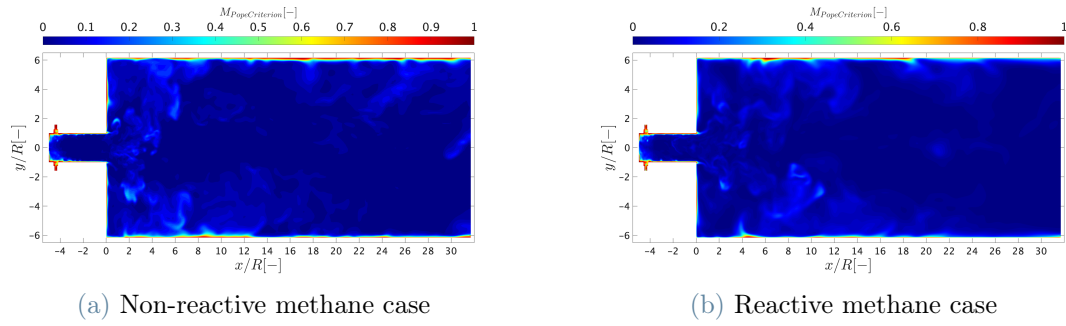
Figure 5.4: Contour of the measure of the turbulent resolution M for the a) non-reactive and b) reactive methane cases.

5.3.   Boundary conditions

Setting up a computational fluid dynamics (CFD) simulation involves a particularly challenging task, namely the specification of boundary conditions (BC). The potential applications and physics encompass a vast array of possibilities, resulting in an extensive range of potential boundary conditions. A fundamental specification employing the fixed value (Dirichlet) and fixed gradient (Neumann) conditions directs the process of establishing boundary conditions, which is not an exact science. Special attention should be given to the boundary conditions (BC) for the variables p and $\mathbf{U}$, as they are coupled [80]. In contrast, the other transported scalar fields, such as k_r, T, ν_t, etc., have independent boundary conditions.

5.3.1.   Non reactive unfueled LES

The set of these non-reactive LESs are meant to be used for validation purposes and they are run with only air as working fluid. The geometry and the patches are shown in figure 5.5.
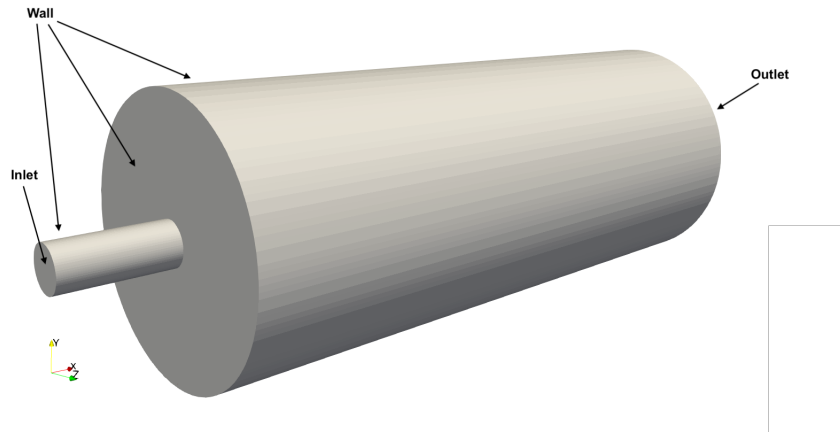
Figure 5.5: Geometry of the domain and patches for the unfueled non-reactive LESs.

Inlet

At the inlet, the swirl-flow of air coming from the swirler enters the domain. The boundary conditions are imposed as specified in table 5.1.

property	dimension	type	value
c	[-]	fixedValue	uniform 0.0
cv	[-]	fixedValue	uniform 0.0
z	[-]	fixedValue	uniform 0.0
zv	[-]	fixedValue	uniform 0.0
k_r	$[m^2/s^2]$	fixedValue	uniform 0.01
ν_t	$[m^2/s]$	calculated	uniform 1e-06
p	[Pa]	zeroGradient	-
T	[K]	fixedValue	uniform ambient temperature
U	[m/s]	decayingTurbulenceInflowGenerator	-
LT	[s]	fixedValue	uniform 0.0

Table 5.1: Boundary condition set at the inlet of the domain.

In particular, in order to impose the velocity field at the inlet, a turbulence inflow generator has been used that produces a transient boundary condition with a flow field that has the same statistics (average and rms) of the velocity field extracted from the LES with the swirler resolved. The extraction has been made at the same position in the mixing tube corresponding to the inlet of the LES without the swirler resolved, in order to reproduce accurately the development of the velocity field. Furthermore the tuning of the tangential velocity of the flow field imposed at the inlet is made, as discussed in detail in section 6.1.1, with the purpose of performing a sensitivity analysis on the swirl number.

Outlet

The boundary conditions at the outlet, where the air is exiting the domain, are imposed as specified in table 5.2.

property	dimension	type	value
c	[-]	zeroGradient	-
cv	[-]	zeroGradient	-
z	[-]	zeroGradient	-
zv	[-]	zeroGradient	-
k_r	$[m^2/s^2]$	zeroGradient	-
ν_t	$[m^2/s]$	calculated	uniform 1e-06
T	[K]	zeroGradient	-
LT	[s]	zeroGradient	-
U	[m/s]	pressureInletOutletVelocity	uniform (0 0 0)

property	dimension	type	rho	psi	gamma	p0	value
p	[Pa]	totalPressure	rho	none	1.4	uniform 101325	uniform 101325

Table 5.2: Boundary condition set at the outlet of the domain.

Wall

The observation can be made, based on the boundary conditions specified in table 5.3, that the Neumann boundary condition applied to the temperature at the wall implies that the combustor is being modeled as adiabatic. Consequently, our chemistry tabulation is limited to four dimensions (4D) rather than five dimensions (5D), as it does not incorporate the specific enthalpy variable, as elaborated upon in section 3.3.1. The imposition of the Dirichlet boundary condition on the function U at the walls may be seen as an expression of the no slip condition, which is used in fluid dynamics to represent the interaction between the fluid and the solid boundary. The turbulent viscosity, denoted

as ν_t, and the residual kinetic energy, denoted as k_r, are represented via the use of wall functions. The parameters pertaining to the turbulent viscosity, ν_t, may be found in table 5.3.

property	dimension	type	value
c	[-]	zeroGradient	-
cv	[-]	zeroGradient	-
z	[-]	zeroGradient	-
zv	[-]	zeroGradient	-
k_r	$[m^2/s^2]$	kqRWallFunction	uniform 0.01
p	[Pa]	zeroGradient	-
T	[K]	zeroGradient	-
U	[m/s]	fixedValue	uniform (0.0 0.0 0.0)
LT	[s]	zeroGradient	-

property	dimension	type	C_μ	k	E	value	nut
ν_t	$[m^2/s]$	nutUSpaldingWallFunction	0.09	0.41	9.8	uniform 0.0	nut

Table 5.3: Boundary condition set at the walls of the domain.

The term "fixedValue" denotes a boundary condition of the Dirichlet type, which enforces a constant value for the associated property. In contrast, the *zeroGradient* boundary condition may be classified as a Neumann condition, since it enforces the gradient of the property it is applied to, specifically setting this gradient to zero. Furthermore, the term *calculated* indicates that the property in question is completely determined by the other specified boundary conditions and properties indicated in the constant folder. The variable nu_t is determined by the turbulence model (i.e., one equation model), specifically by the parameter k_r. The specified value is optional for this type of boundary condition. Accurate specification of boundary conditions is crucial in the context of solving partial differential equations (PDEs), as they play a pivotal role in establishing the unique solution within

the given domain. The *pressureInletOutletVelocity* type enables the maintenance of a defined outlet pressure and permits the flow to exit the computational domain without prescribing the outlet velocity. For outgoing fluxes, this type of boundary condition is equivalent to the *zeroGradient* one. Finally, the type *totalPressure* is used to enforce the total pressure according to the equation $p_p = \frac{p_0}{\left(1+\frac{\gamma-1}{2\gamma}\psi|\mathbf{u}|^2\right)^{\frac{\gamma}{\gamma-1}}}$, where γ represents the ratio of the specific heats.

5.3.2. Wall functions

Residual kinetic energy wall function

For the modeling of the residual kinetic energy close to the walls, the *kqRWallFunction* has been adopted. This boundary condition provides a simple wrapper around the zero-gradient condition, which can be used for the turbulent kinetic energy (i.e. k), square-root of turbulent kinetic energy (i.e. q) and Reynolds stress symmetric-tensor fields (i.e. R) [81].

Turbulent viscosity wall function

The modeling of the turbulent viscosity close to the walls, is dealt with the adoption of *nutUSpaldingWallFunction*. This boundary condition provides a wall function for the turbulent viscosity (i.e. nut) based on velocity (i.e. U). Using Spalding's law gives a continuous nut profile to the wall [81].

Both of the implemented wall functions are capable of handling the buffer layer and are therefore y^+-insensitive. The hystogram of y^+ and its cumulative function are illustrated in figure 5.6.

(a) y^+ hystogram   (b) Cumulative y^+ hystogram
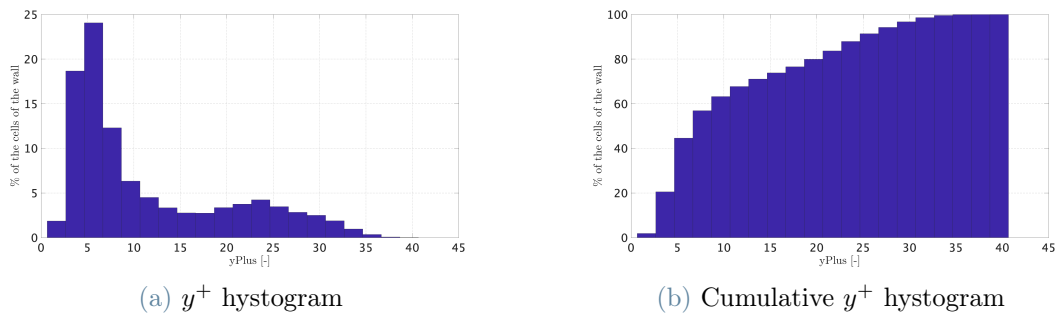
Figure 5.6: Hytogram of a) y^+ and b) Cumulative function of y^+ for the cells belonging to the wall.

It is evident that approximately 75% of the cells contain a $y+$ positioned within the range of 5 to 30, that represents the buffer layer.

5.3.3. Methane non-reactive and reactive LESs

The two LESs are operated using both air and methane. The air enters the computational domain through the *INLET* patch, which represents the outlet of the swirler. On the other hand, the methane enters the computational domain through the *INLET_FUEL* patch. The figure 5.7 displays the geometry and patches.

(a)   (b)
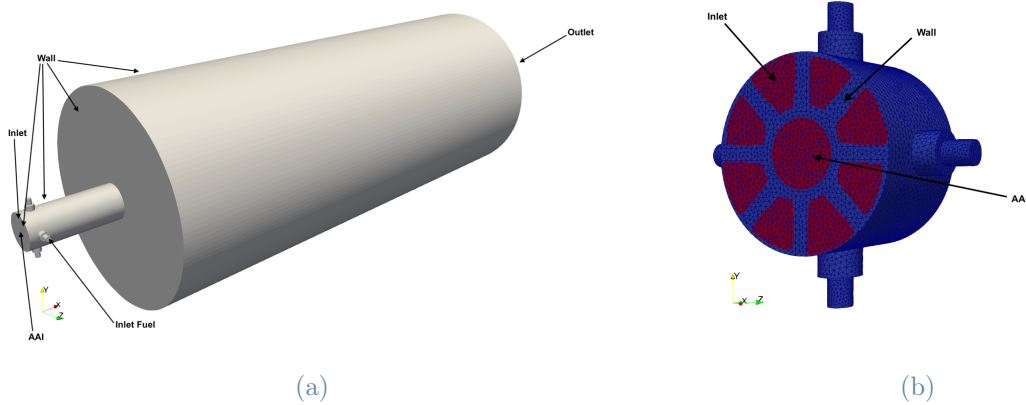
Figure 5.7: a) Geometry of the domain and patches and b) detail of the inlet section; for the methane non-reactive and reactive LESs.

Inlet

The air with a swirling motion, originating from the swirler, enters the domain at the inlet. The boundary conditions are applied according to the specifications provided in the table 5.4. It should be noted that the boundary condition for NO is only utilized in the reactive scenario.

property	dimension	type	value
c	[-]	fixedValue	uniform 0.0
cv	[-]	fixedValue	uniform 0.0
z	[-]	fixedValue	uniform 0.0
zv	[-]	fixedValue	uniform 0.0
k_r	$[m^2/s^2]$	fixedValue	uniform 0.01
ν_t	$[m^2/s]$	calculated	uniform 1e-06
p	[Pa]	zeroGradient	-
T	[K]	fixedValue	uniform ambient temperature
U	[m/s]	decayingTurbulenceInflowGenerator	-
LT	[s]	fixedValue	uniform 0.0
NO	[-]	fixedValue	uniform 0.0

Table 5.4: Boundary condition set at the inlet of the domain.

Inlet Fuel

The fuel is injected downstream of the swirler at the fuel ports. The boundary conditions applied at this particular patch are explicitly defined in table 5.5.

property	dimension	type	value
c	[-]	fixedValue	uniform 0.0
cv	[-]	fixedValue	uniform 0.0
z	[-]	fixedValue	uniform 1.0
zv	[-]	fixedValue	uniform 0.0
k_r	$[m^2/s^2]$	fixedValue	uniform 0.01
ν_t	$[m^2/s]$	calculated	uniform 1e-06
p	[Pa]	zeroGradient	-
T	[K]	fixedValue	uniform ambient temperature
U	[m/s]	flowRateInletVelocity; massFlowRate	$\dot{m}_{fuel}$
LT	[s]	fixedValue	uniform 0.0
NO	[-]	fixedValue	uniform 0.0

Table 5.5: Boundary condition set at the fuel ports.

Axial Air Injection

A non-swirling airflow is introduced into the pipe for axial air injection. The boundary conditions are enforced according to the specifications outlined in table 5.6.

property	dimension	type	value
c	[-]	fixedValue	uniform 0.0
cv	[-]	fixedValue	uniform 0.0
z	[-]	fixedValue	uniform 0.0
zv	[-]	fixedValue	uniform 0.0
k_r	$[m^2/s^2]$	fixedValue	uniform 0.01
ν_t	$[m^2/s]$	calculated	uniform 1e-06
p	[Pa]	zeroGradient	-
T	[K]	fixedValue	uniform ambient temperature
U	[m/s]	flowRateInletVelocity; massFlowRate	0
LT	[s]	fixedValue	uniform 0.0
NO	[-]	fixedValue	uniform 0.0

Table 5.6: Boundary condition set at the inlet of the axial air injection pipe.

Since the Reynolds number for the cylindrical internal geometry of the patches *INLET_FUEL* and *AAI* is below the threshold for laminar-turbulent transition, the flow in this region is characterized as laminar and non-swirling. As a result, the boundary conditions for velocity can be imposed as a mass flow rate condition.

Outlet

The prescribed boundary conditions at the outlet, where the mixture of air and fuel is being discharged from the computational domain, are enforced according to the specifications outlined in table 5.7.

property	dimension	type	value
c	[-]	zeroGradient	-
cv	[-]	zeroGradient	-
z	[-]	zeroGradient	-
zv	[-]	zeroGradient	-
k_r	$[m^2/s^2]$	zeroGradient	-
ν_t	$[m^2/s]$	calculated	uniform 1e-06
T	[K]	zeroGradient	-
U	[m/s]	pressureInletOutletVelocity	uniform (0 0 0)
LT	[s]	zeroGradient	-
NO	[-]	zeroGradient	-

property	dimension	type	rho	psi	gamma	p0	value
p	[Pa]	totalPressure	rho	none	1	uniform 101325	uniform 101325

Table 5.7: Boundary condition set at the outlet of the domain.

Wall

The boundary conditions that have been specified at the patch *WALL* are provided in table 5.8.

property	dimension	type	value
c	[-]	zeroGradient	-
cv	[-]	zeroGradient	-
z	[-]	zeroGradient	-
zv	[-]	zeroGradient	-
k_r	$[m^2/s^2]$	kqRWallFunction	uniform 0.01
p	[Pa]	zeroGradient	-
T	[K]	zeroGradient	-
U	[m/s]	fixedValue	uniform (0.0 0.0 0.0)
LT	[s]	zeroGradient	-
NO	[-]	zeroGradient	-

property	dimension	type	C_μ	k	E	value	nut
ν_t	$[m^2/s]$	nutUSpaldingWallFunction	0.09	0.41	9.8	uniform 0.0	nut

Table 5.8: Boundary condition set at the walls of the domain.

5.4. Initial conditions

In order to speed up the convergence until the achievement of a steady case, the whole domain is initialized with the conditions specified in table 5.9. NO is specified only for the reactive LES.

property	dimension	internalField
c	[-]	uniform 0.0
cv	[-]	uniform 0.0
z	[-]	uniform 0.0
zv	[-]	uniform 0.0
k_r	$[m^2/s^2]$	uniform 0.01
ν_t	$[m^2/s]$	uniform 0.0
p	[Pa]	101325
T	[K]	uniform ambient temperature
U	[m/s]	uniform (0.0 0.0 0.0)
LT	[s]	uniform 0.0
NO	[-]	uniform 0.0

Table 5.9: Initial conditions.

5.5. Numerical schemes

The following numerical schemes were implemented in order to solve the equations:

- Temporal derivatives - $\dfrac{\partial \phi}{\partial t}$. In order to discretize the temporal derivatives, a first-order implicit Euler scheme was chosen.

- Gradient schemes $\nabla \phi$. Regarding the gradients, a Gauss scheme with linear interpolation between cell centers and face centers was used.

- Convective terms schemes - $div\phi$. The numerical schemes that have been used are:

Gauss LUST (i.e. Linear-Upwind Stabilised Transport) for the velocity field, *Gauss linear* for the pressure field and *Gauss limitedLinear 0.5* for all the other properties.

- Laplacian schemes - $\nabla^2 \phi$. The scheme used for the Laplacian terms is *Gauss linear corected*, the correction method has been employed to account for the error introduced by non-orthogonality of the mesh on diffusive terms.

- Interpolation schemes - $\phi|_f$. A *linear* interpolation scheme has been adopted.

- Surface-normal gradient schemes - $\nabla_{\perp A} \phi$. The *corrected* scheme has been selected for the same rationale as Laplacian schemes, namely to address the inaccuracy arising from the non-orthogonal mesh in diffusive terms.

5.6. Algorithm and numerical solvers

5.6.1. Numerical solvers

The equation solvers and tolerances are illustrated in table 5.10.

property	solver	tolerance	smoother
U	GAMG	1e-07	GaussSeidel
P	GAMG	1e-07	GaussSeidel
rho	GAMG	1e-08	GaussSeidel
he	GAMG	1e-07	GaussSeidel
R	PBiCG	1e-05	-
k	PBiCG	1e-06	-
c|cv|z|zv|LT|NO	GAMG	1e-07	GaussSeidel
$\overline{\overline{\omega}}$	GAMG	1e-08	GaussSeidel

Table 5.10: Equaton solvers and tolerances.

5.6.2. PIMPLE algorithm

The PIMPLE algorithm, which integrates the advantages of the PISO (Pressure-Implicit with Splitting of Operators) and SIMPLE (Semi-Implicit Method for Pressure-Linked

Equations) algorithms, has been used to solve the governing equations and establish the pressure-velocity coupling.

The inclusion of the PIMPLE loop, as seen in figure 5.8, facilitates the solution of equations by using variables that are updated inside each time step. Consequently, this approach enhances accuracy by ensuring the matrix coefficients are appropriately updated.

START $t = t_{start}$ ──── **WHILE** $t < t_{end}$

$t = t + \Delta t$

Energy $\partial T / \partial t + \nabla \cdot (\mathbf{u}T) - \nabla \cdot (\alpha \nabla T) = r$

under-relax, solve for T

Momentum matrix $\mathbf{A} \cdot \mathbf{u} - \mathbf{b}$ Eq. (5.21)

under-relax matrix eqn

Momentum predictor $\mathbf{A} \cdot \mathbf{u} - \mathbf{b} = -\nabla p$ **PIMPLE loop**

solve for $\mathbf{u}$

Pressure equation $\nabla \cdot \dfrac{1}{A} \nabla p = \nabla \cdot \left[\dfrac{\mathbf{H(u)}}{A} \right]$

solve for p

Flux corrector $\phi_f := \mathbf{S_f} \cdot \left(\dfrac{\mathbf{H(u)}}{A} \right)_f - \left(\dfrac{|\mathbf{S_f}|}{A} \right)_f \nabla_n p_f$

PISO loop

under-relax p

Momentum corrector $\mathbf{u} := \dfrac{\mathbf{H(u)}}{A} - \dfrac{1}{A} \nabla p$

$p, \mathbf{u}, \phi_f, T$

ENDWHILE
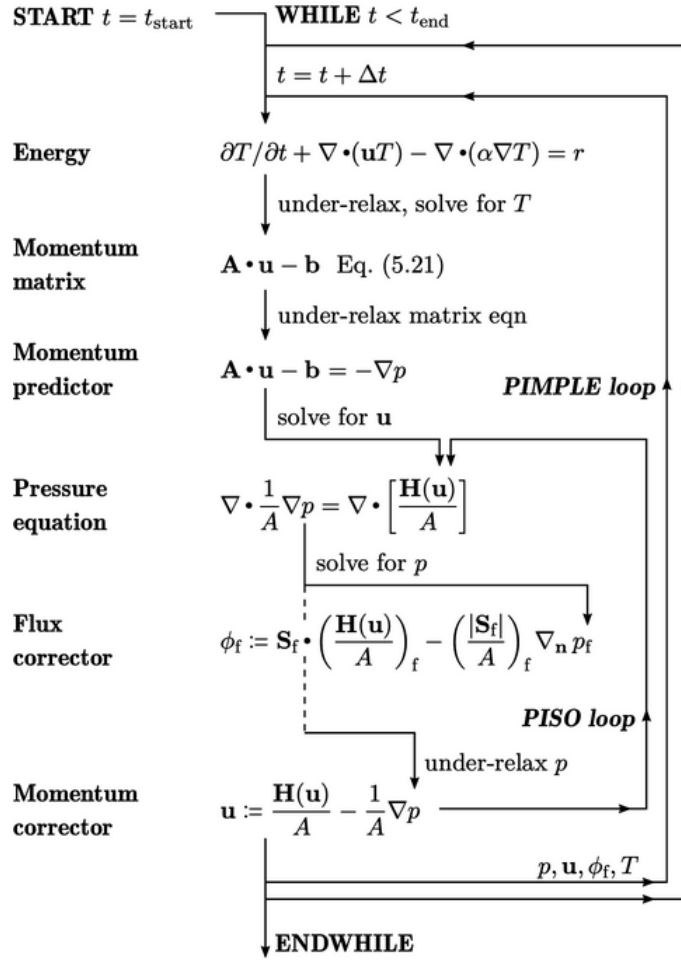
Figure 5.8: Scheme of the PIMPLE algorithm [80]

The PIMPLE algorithm has two distinct loops: an inner loop known as PISO, which repeatedly solves the pressure equation, and an outer loop referred to as PIMPLE, which solves the momentum equation alongside other transport equations. Specifically, the method used for the Large Eddy Simulation in this study executes two iterations of the outer loop and three iterations of the inner loop. The residual control strategy used for the PIMPE loop relies on the momentum equation that solves for U. The specified tolerance for this control strategy is set at $1e - 04$, while the relative tolerance is established at $1e - 03$.

The PIMPLE method used in this study solves the pressure and density equations inside the inner PISO loop. Additionally, it solves the transport equations for various variables in the outside PIMPLE loop, namely, velocity denoted as U, subgrid-scale kinetic energy referred to as k (which may be considered equivalent to the residual kinetic energy [19]), progress variable denoted as c, variance of the progress variable referred to as cv, specific enthalpy denoted as he, mixture fraction referred to as z, variance of the mixture fraction denoted as zv, local flow age referred to as LT, and nitric oxide mass fraction denoted as NO.

The use of relaxation factors is employed to enhance the stability of equation resolution, as seen in table 5.11. This is especially crucial when addressing reactive scenarios. Unfortunately, this always comes with a longer computational time.

equation	relaxation factors
U	0.5
p	0.3
k	0.5
zv	0.7
cv	0.7
c	0.7

Table 5.11: Relaxation factors adopted.

5.7. CFL number

The Courant–Friedrichs–Lewy number (CFL) is formally defined as in equation (5.3) for the one-dimensional scenario.

$$CFL \doteq \frac{u\Delta t}{\Delta x} \tag{5.3}$$

where u is the magnitude of the velocity, Δt is the time step and Δx is the dimension of the cell we are referring to. For the multi-dimensional case, the definition is represented in equation (5.4):

$$CFL = \Delta t \left(\sum_{i=1}^{n} \frac{u_i}{\Delta x_i} \right) \tag{5.4}$$

with $i = \{1, 2, 3\}$ being the three directions in space.

In order to ensure temporal accuracy in transient simulations using PIMPLE algorithm, it is possible to maintain a Courant number larger than one by using a second order time scheme, as suggested in [80]. Nevertheless, given the use of a first-order numerical scheme for temporal discretization in the present work, it is advisable to maintain a Courant number below unity in order to enhance stability. Specifically, the CFL number will be maintained at values around 0.7 for non-reactive simulations and below $0.3 - 0.4$ for reactive simulations by varying the time step. In the case of non-reactive simulations including just air, a time step of $3.5e - 06[s]$ was used. However, for non-reactive full methane simulations, a smaller time step of $0.85e - 06[s]$ was employed owing to the implementation of a finer mesh. Conversely, in the case of reactive full methane simulations, a time step of $0.4e - 06[s]$ was necessary. The objective of this is to maintain an appropriate temporal discretization in relation to the spatial discretization provided by the mesh. This relation enhance the lower is the value of the Courant number.

6 | Results

This chapter provides an examination and evaluation of the outcomes, beginning with a discussion on the sensitivity analysis conducted to construct the final Large Eddy Simulation (LES) model. The model's validity is assessed by comparing it to Particle Image Velocimetry (PIV) data. This analysis is presented in section 6.1. Furthermore, in section 6.2, we examine the non-reactive full CH_4 LES, focusing on the clarification of the impact of density on vortex breakdown. The accuracy of the utilized reactive Large Eddy Simulation model in forecasting nitric oxide emissions is shown in section 6.3 via the analysis of reactive full CH_4 simulation. This analysis highlights the superiority of the reactive LES model, with the transport equation developed in the work [16] implemented, over the less accurate retrieval from tabulation.

6.1. Sensitivity Analysis on the Swirl Number

6.1.1. Methodology

Firstly, it is important to notice the manner in which the boundary condition for the velocity field has been established. As elucidated in chapter 5, the flow field can be extracted at the same location from a Large Eddy Simulation that encompasses the swirler, serving as the inlet for the LES domain. This approach is used to effectively capture the physics of the swirling flow. This approach is also used to avoid the need of simulating the swirler, which requires cells of such small size that the time step must be limited in order to maintain the Courant-Friedrichs-Lewy (CFL) condition below the predetermined threshold. Consequently, this leads to an unacceptably long simulation time. To achieve this objective, an inflow turbulence generator is used in order to generate a flow field that has the same mean and variance as the extracted field. The flow field obtained is post processed using Matlab, enabling the scaling of both the bulk velocity, and as a consequence the axial component of velocity, and the azimuthal component of the velocity. The adjustment of the tangential velocity is achieved by the implementation of a scaling factor, which then alters the swirl number of the fluid as it exits the swirler

and enters the mixing tube. As elucidated in chapter 4, the swirl number is characterized as the dimensionless ratio between the axial flow of angular momentum and the axial flux of axial momentum. It is further normalized using a reference radius, which in this study corresponds to the radius of the mixing tube. The relationship shown by Equation (4.1) illustrates that the axial and azimuthal components of velocity constitute the primary factors governing the swirl number. The findings indicate that the bulk velocity is adjusted to enforce the nominal mass flow rate, resulting in a fixed value. Consequently, the only determining factor for altering the swirl number (4.1) is the azimuthal velocity.

The altered flow field is now enforced at the inlet of the domain as a boundary condition.

The generation of the inlet flow field is a crucial step in cases where the swirler is not being solved. This is due to the turbulent nature of the flow, characterized by a Reynolds number of around 6000 in the analyzed combustor under the set conditions. It is important to note that this value is much higher than the laminar-turbulent transition threshold of 2300 for the internal pipe's shape. Additionally, the flow exhibits swirling motion. Due to this rationale, both the boundary conditions of mass flow rate and bulk velocity are deemed unsuitable since they would enforce a non-swirling laminar flow.

At present, the ability to manipulate the swirl number by adjusting the azimuthal component allows for a sensitivity analysis on the Swirl number. This analysis is facilitated by the reduction in computational costs achieved through the elimination of the swirler from the simulated domain. This elimination is accomplished by imposing the inlet's boundary condition for velocity in this specific manner. The computing cost of LES is quite high and, despite using this technique, each non-reactive LES for the full-air case was executed in parallel on 320 processors for a duration of 80.5 hours, resulting in an overall computational cost of 25760 CPU hours for each simulation. The duration of the simulation is determined by the need to simulate two flow through time: the first to achieve a steady flow within the combustor, and the second to conduct a time-averaging on the Favre-filtered quantities that are not significantly impacted by the transient. The calculation of the time needed by a fluid particle to travel from the inlet to the outlet of the domain, referred to as the flow through time, has been performed by solving a transport equation for the local flow age. This approach offers improved accuracy compared to estimating the flow through time solely based on geometric considerations, such as the ratio between the length of the combustor and a characteristic velocity (e.g. bulk velocity). Figure 6.1 illustrates the flow through time, which result to be approximately $900[ms]$ in the non-reactive full air case inside the TUDelft combustor, which turned out to be the time after which the flow within the combustor became statistically stationary by examining the flow field's evolution in time.
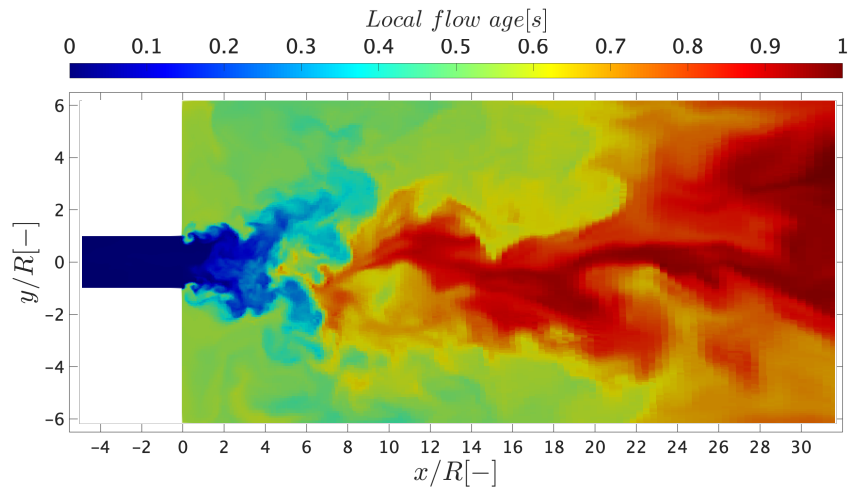
Figure 6.1: Contour plot of the local flow age within the combustor.

The duration of the simulated time for each Large Eddy Simulation (LES) is around 1.8 seconds. The decision about the number of processors to be used for parallel execution of the LESs is determined by balancing the queuing time required for cluster usage and the execution time of each iteration. The former and the latter correspondingly exhibit an upward and downward trend as the number of processors increases. The graph shown in figure 6.2a illustrates the relationship between the execution time per iteration and the number of processors used for the parallelization of the instances. It is worth noting that as the number of processors increases, a point of saturation is reached. This occurs when the increase in processing speed is offset by a decrease in communication efficiency among the processors. Increasing CPU time per iteration, as depicted in figure 6.2b, further illustrates this loss of efficiency as the number of processors increases.

(a)

(b)
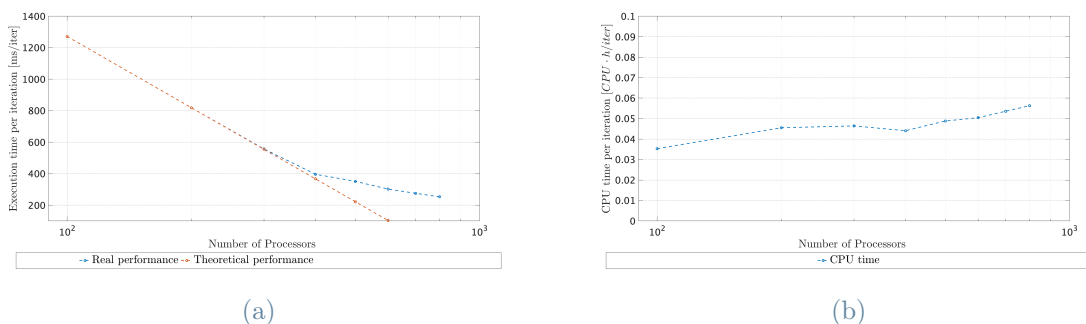
Figure 6.2: a) Execution time per iteration and b) CPU time per iteration against number of processors for the non-reactive full-methane LES that has run on DelftBlue supercomputer [79].

Given the number of LESs conducted for the purpose of sensitivity analysis, it was seen that a decrease in queuing time had a more pronounced effect. Consequently, a decision was made to choose for the use of 320 processors, taking into account the reduced cell count of the non-reactive unfueled Large Eddy Simulations (LESs). The crucial factor for determining the appropriate scaling of the graph 6.2a in a domain with fewer cells is the execution time per iteration relative to the number of cells per processor. A larger quantity of processors, namely 800, were used to execute the non-reactive and reactive full methane scenarios. This decision was made due to the intention of conducting just one Large Eddy Simulation (LES) for each case. Consequently, the primary objective in these two situations was to minimize the execution time each iteration.

Regarding the sensitivity analysis, a variation of the swirl number is conducted in order to get a satisfactory agreement with the Particle Image Velocimetry data accessible inside the research facility. This enabled the validation of the non-reactive LES model via experimental data, providing a deeper understanding of the behavior of swirl flow inside the TUDelft combustor for future research purposes.

The resulting changes of the swirl number for various values of tangential velocity used by LESs is shown in Figure 6.3.
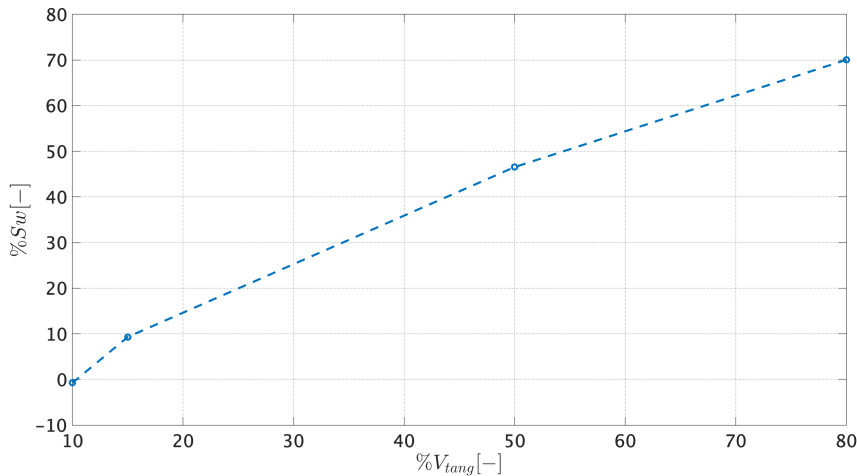
Figure 6.3: Swirl number percentage variation for varying percentage variation of the tangential velocity.

The integral operator's linearity implies that any multiplication applied to the azimuthal component of the velocity will provide an equivalent multiplication for the swirl number, as expressed in equation (4.1). It can be observed that this is reasonably respected for the tuning made, with the swirl number variation obtained underestimated for each of the four cases. It is evident from figure 6.3 that the $LES10\%$ case does not exhibit the

anticipated 10% increase in swirl number. Consequently, at the inlet of the mixing tube, there is minimal disparity in swirl number between the $LES0\%$ and $LES10\%$ cases, as depicted in figure 6.6.

The velocity field imposed at the inlet for the situations with 0% and 50% modification of the tangential velocity is shown in figure 6.4 as a representative example. The axial velocity field remains constant, whereas the tangential velocity field exhibits an increase, as desired.
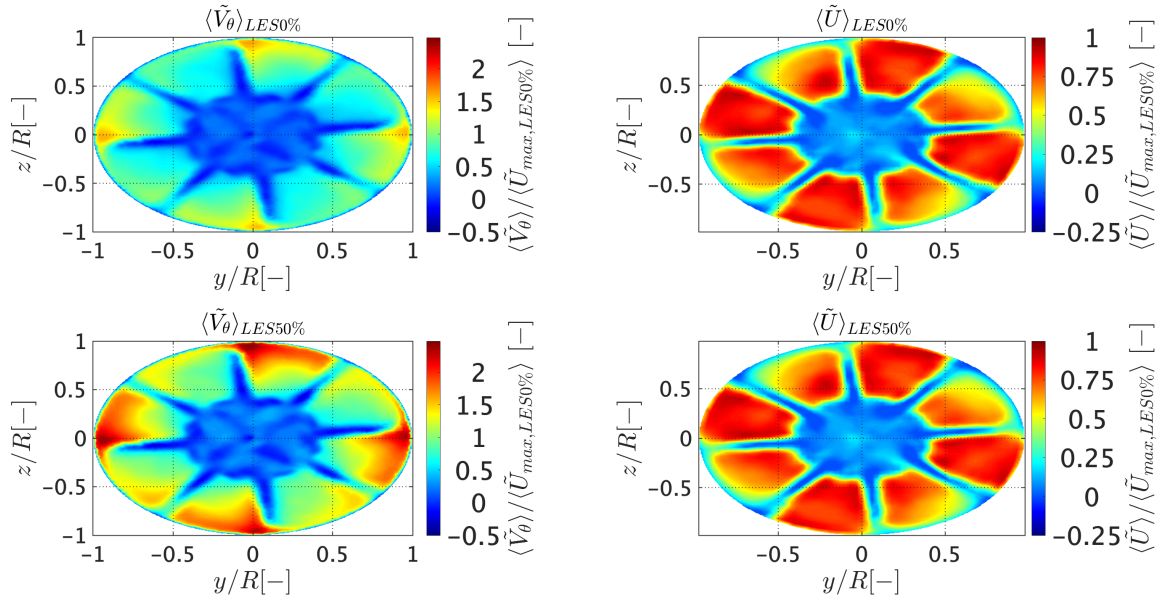
Figure 6.4: Tangential and axial component of the velocity field imposed at the inlet of the domain as boundary condition. Adjustment of the tangential component (first column) and axial component (second column) for the 0% LES (first row, coincides with the extracted flow field) and the 50% LES (second row).

It is worth mentioning that the axial velocity inside the axial air injection pipe is around zero, which aligns with the use of 0% axial air injection (AAI) and the extraction of the slice in close proximity to the swirler outlet for all the large eddy simulations (LESs) conducted in this study. The results of the reactive full methane studies indicate the absence of flashback, hence overcoming the need for axial air injection. The non-zero deviation seen in the axial velocity profile at AAI may be attributed to the incomplete development of the extracted profile. Consequently, there has been prior momentum transport towards the motionless center zone.

6.1.2. Sensitivity analysis

This paragraph presents the findings of the sensitivity analysis. A total of five cases were simulated, as illustrated in Table 6.1. In these cases, the tangential velocity increase serves as a factor by which each tangential velocity profile of the base case is multiplied to obtain the tuned LES. Mathematically, the tuned LES tangential velocity profile at a given location $\boldsymbol{x}$ and time t^* is expressed as $V_{\theta,LESX\%}(\boldsymbol{x}, t^*) = (1+X/100)\cdot V_{\theta,LES0\%}(\boldsymbol{x}, t^*)$. The variable denoted as t^* represents the specific moment in time of the extraction of the flow field from the LES that resolves the swirler.

LES	Tangential velocity increase	Axial velocity increase
LES 0% (Base Case)	0%	0%
LES 10%	10%	0%
LES 15%	15%	0%
LES 50%	50%	0%
LES 80%	80%	0%

Table 6.1: Overview of non-reactive full air LESs.

Initially, a verification of the mass flow rate along the mixing tube is conducted, as depicted in figure 6.5, in order to ascertain that the prescribed flow field at the inlet adheres to the nominal mass flow rate and that mass conservation is maintained for the LESs throughout the mixing tube. Thirteen slices are taken from the mixing tube, and the mass flow rate through each slice is calculated by adding the contributions of all the cells inside the slice. This calculation is performed using time-averaged Favre-filtered values, as described by equation (6.1):

$$\langle \dot{m} \rangle = \sum_i \langle \tilde{\rho}_i \rangle \langle \tilde{U}_i \rangle A_i \tag{6.1}$$

where i is the i-th cell of the slice and $\langle \cdot \rangle$ stands for the time-averaging.
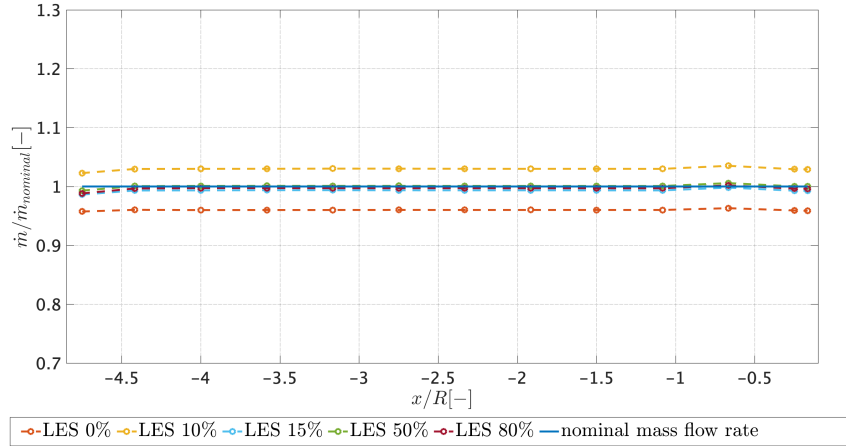
Figure 6.5: Mass flow rate along the mixing tube varying V_{tang}.

It is evident that the basic scenario, whereby the flow field is extracted and imposed without any modifications, exhibits an underestimation of the mass flow rate by 4%. With the exception of $LES10\%$, which exhibits an inaccuracy of around 3%, all other LESs provide reliable predictions of the nominal value of the mass flow rate, with errors below 0.7%. Additionally, it is evident that the mass flow rate remains constant throughout the mixing tube, since all the LESs exhibit a consistent $\dot{m}$ value relative to the dimensionless axial locations x/R inside the mixing tube. The disparity in mass flow rate between the $LES0\%$ and the other LESs can be ascribed to the employment of the low Mach approximation in the adjusted LESs. It is worth mentioning that the oscillations observed in the mass flow rate can be attributed to the interpolations conducted by Paraview, the software utilized for visualizing the solutions of the LESs. These oscillations arise when extracting streamwise slices. Indeed, the check on continuity equation error is performed through the log file and it is always limited below 1e-06. Indeed, the verification of continuity equation error is conducted by examining the log file, with a maximum threshold of 1e-06.

The Swirl number is graphically shown throughout the length of the mixing tube for all five situations as seen in figure 6.6. The observed trend exhibits a decline as the axial position increases, which may be attributed to the presence of the viscous dissipation factor in the momentum equation. As anticipated, the swirl number exhibits an increase proportionate to the magnitude of the modification made to the tangential velocity.
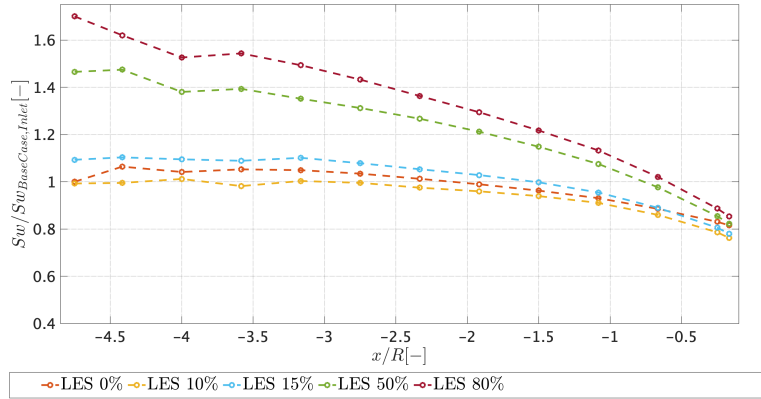
Figure 6.6: Swirl number along the mixing tube varying V_{tang}.

The swirler has a certain geometrical swirl number, given by the shape of its blades. Additionally, it is observed that the maximum normalized swirl number at the inlet of the mixing tube in the LESs is 1.7 times greater than the aforementioned geometric swirl number (referred to as the swirl number of the base case). This indicates that the relevant portion of figure 6.6 is located at the inlet of the combustion chamber (specifically, when the dimensionless axial distance, x/R, is equal to 0). The upstream trends depicted in the figure are not representative of actual conditions, but rather are generated by the sensitivity analysis. These values are higher than what is necessary for a certain level of vortex breakdown intensity to occur in the combustion chamber. In essence, due to the inadequate predictive capability of the base case in relation to the CRZ and the jet's aperture within the combustion chamber, it is necessary to validate the LES model through tuning. This validation process should primarily focus on replicating the swirl number obtained at the outlet of the mixing tube, as it plays a crucial role in accurately reproducing the physics of the swirling flow inside the combustion chamber. The tuning is made upstream, the interested result is observed downstream.

The adjustments made to the Swirl number at the outlet of the mixing tube, compared to the base case, are presented in table 6.2. The impact of these adjustments is then illustrated in figures 6.7, 6.8, 6.9, 6.10, and 6.11, which depict the comparison of the radial profile of the time-averaged Favre-filtered axial velocity along the combustion chamber for all five Large Eddy Simulations. The radial profile is obtained by calculating the azimuthal average of the time-averaged Favre-filtered axial velocity, as represented by equation (6.2):

$$\langle \widetilde{U} \rangle (x, r) = \frac{1}{2\pi T} \int_0^{2\pi} \int_t^{t+T} \tilde{U}(t, x, r, \varphi) dt d\varphi, \tag{6.2}$$

where the cylindrical coordinates (x, r, ϕ) have been employed. The radial profile are then mirrored to show the profile in the diametral slices of figures 6.7,6.8,6.9, 6.10 and 6.11.

LES	Tuning Sw in $x/R = 0$
LES 0% (Base Case)	0%
LES 10%	-6.55%
LES 15%	-4.33%
LES 50%	0.85%
LES 80%	4.60%

Table 6.2: Obtained tuning of the Swirl number at the outlet of the mixing tube, with respect to the base case.

The beginning point is shown in figure 6.7, This figure illustrates the base case in comparison to the PIV data for six different streamwise locations inside the combustion chamber. The agreement demonstrates satisfactory performance across all axial positions, with the exception of the initial position. In this particular instance, the model fails to adequately describe the central recirculation zone and the aperture of the jet. Specifically, a greater swirl number is required at the entrance of the combustion chamber in order to provide a broader aperture for the jet. Additionally, an increased swirl number would result in the production of a more intense vortex breakdown, characterized by a a stronger axial component of the pressure gradient along the centerline. Consequently, the presence of a greater reverse flow would result in lower negative velocities along the centerline. As previously mentioned in chapter chapter 4, the precise estimation of the CRZ has great importance as it has a substantial impact on the processes of mixing and flame stabilization.
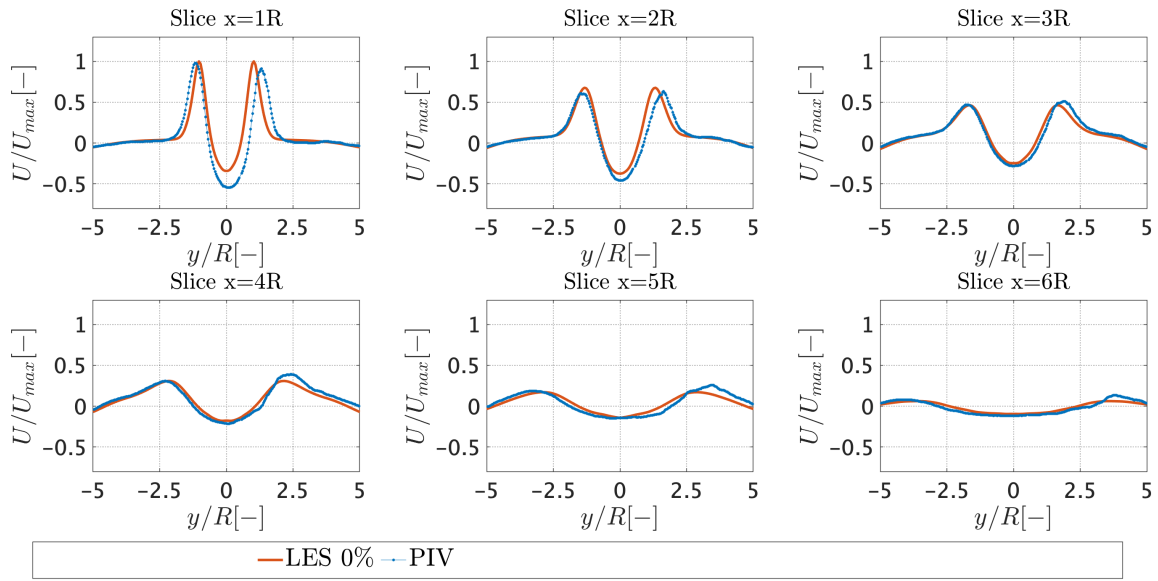
Figure 6.7: LES Favre-filtered time-averaged radial distribution of the axial velocity against PIV.

The data shown in Figure 6.8 indicates that, in relation to $LES10\%$, there is a decrease in the width of the jet's aperture beyond the location of $x/R = 2$. Coherently, the tuned swirl number is smaller compared to the base case.
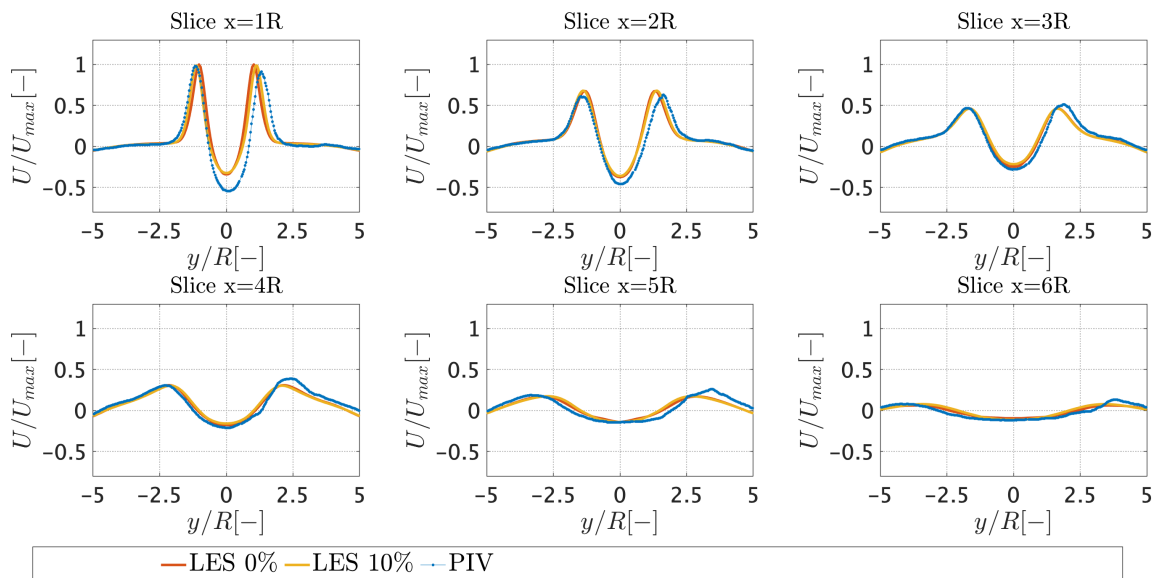
Figure 6.8: LES Favre-filtered time-averaged radial distribution of the axial velocity against PIV.

The aforementioned observation also holds true for the $LES15\%$ scenario. As shown in Figure 6.9, it can be seen that the peaks of velocity are situated at somewhat greater radial positions, which aligns with the larger swirl number that was achieved.
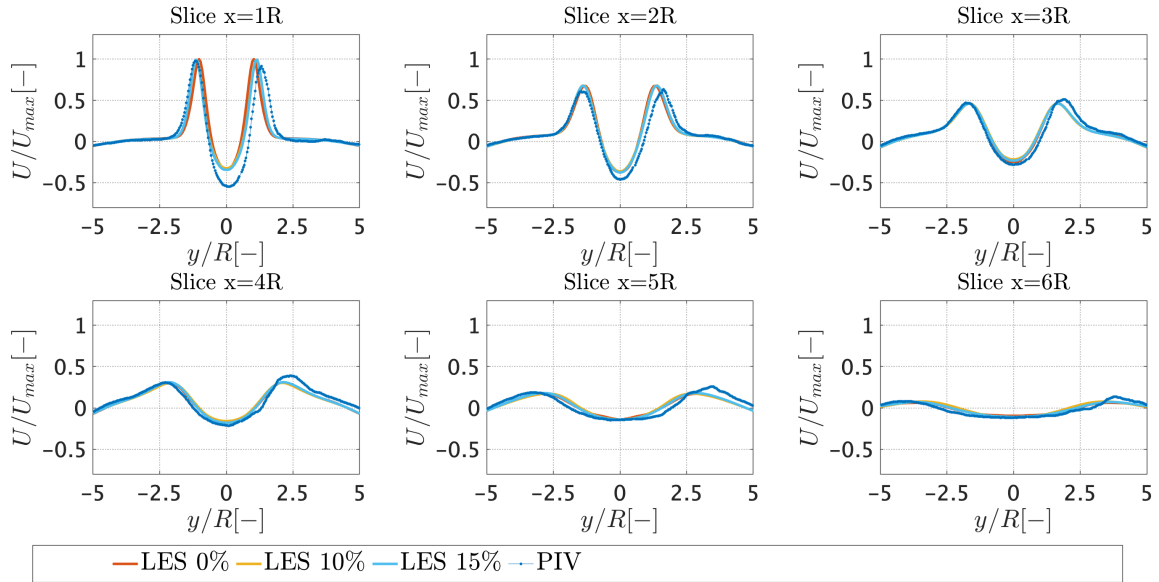
Figure 6.9: LES Favre-filtered time-averaged radial distribution of the axial velocity against PIV.

When the tangential velocity adjustment is increased by 50%, a high level of accuracy is attained for all streamwise locations. The cross-sectional slice denoted as $x/R = 1$ demonstrates a precise prediction of the central recirculation zone, while also exhibiting a consistent aperture of the jet with the experimental observations. The peaks of axial velocity exhibit greater magnitudes in comparison to earlier LESs, mostly due to the intensified reverse flow and the need for the mass to conserve. The LES model with a 50% adjustment has the highest level of agreement with the experimental PIV data, demonstrating a notable accuracy in its ability to forecast the flow field. Therefore, the adjustment of the azimuthal component of the velocity will be maintained for the further examination of TUDelft's combustor in this study. It is noteworthy that despite the significant multiplication factor used for the variable V_θ, the resulting percentage increase in the Swirl number at the entrance of the combustion chamber is only 0.85%. However, this increase is enough for correcting the flow field, leading to a very accurate alignment with experimental results.
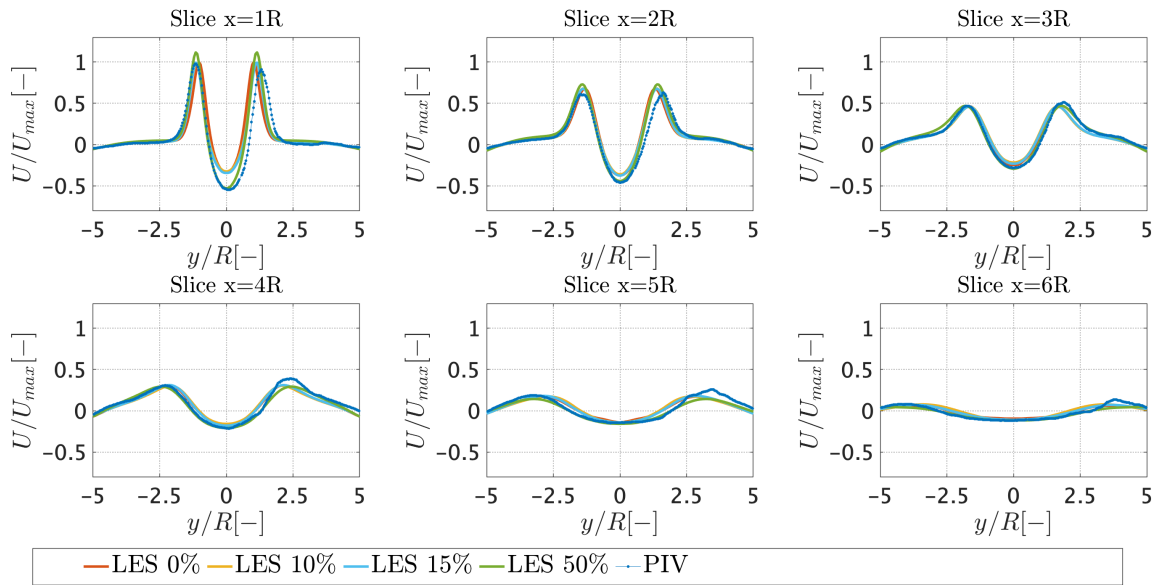
Figure 6.10: LES Favre-filtered time-averaged radial distribution of the axial velocity against PIV.

In order to ensure comprehensive analysis, the $LES80\%$ scenario is also included in the study. The radial distribution of the axial velocity aligns with the anticipated pattern, whereby a larger swirl number at the inlet of the chamber leads to a more pronounced axial component of the pressure gradient. Consequently, this results in a more intense central recirculation zone (CRZ) with greater velocity peaks. The aperture of the jet is broader.
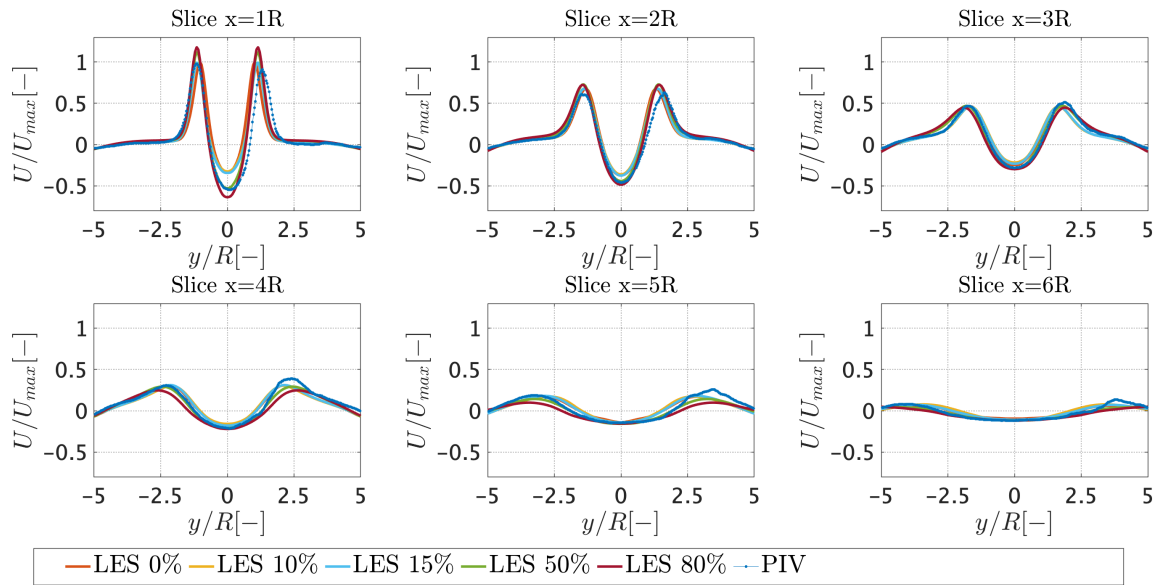
Figure 6.11: LES Favre-filtered time-averaged radial distribution of the axial velocity against PIV.

The axial velocity distribution in the first six radiuses of the combustion chamber for $LES50\%$ and PIV is shown in Figure 6.12. The agreement about the jet's aperture, strength of the CRZ, and the effectiveness of capturing the vorticity, especially in the outer recirculation zone, is remarkable.
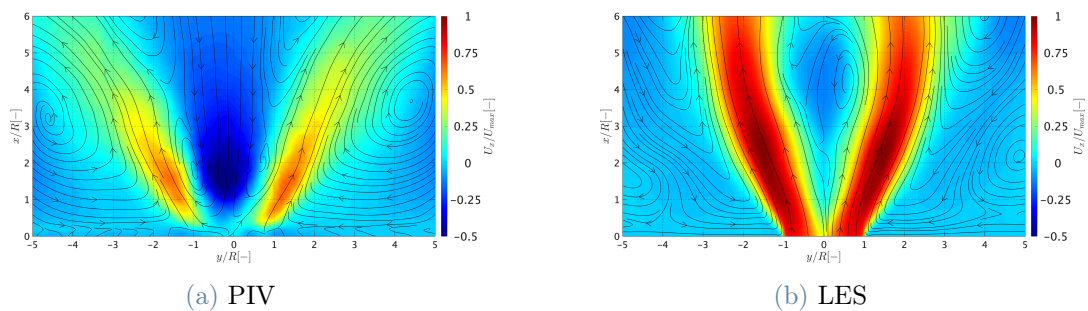

(a) PIV

(b) LES
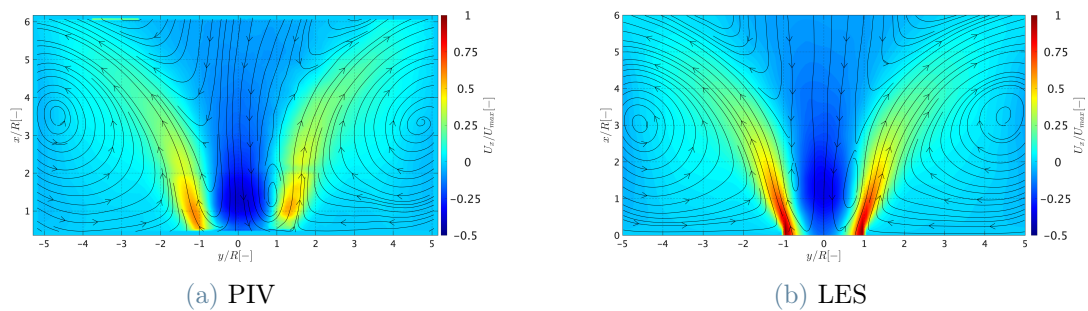
Figure 6.12: Colormap representing a) PIV axial velocity b) the axial velocity of the LES 50% in the combustion chamber. Streamlines are depicted for the velocity field.

The examination of the mass flow rate in the combustion chamber for the $LES50\%$ that is selected for further investigation is conducted, as shown in Figure 6.13.
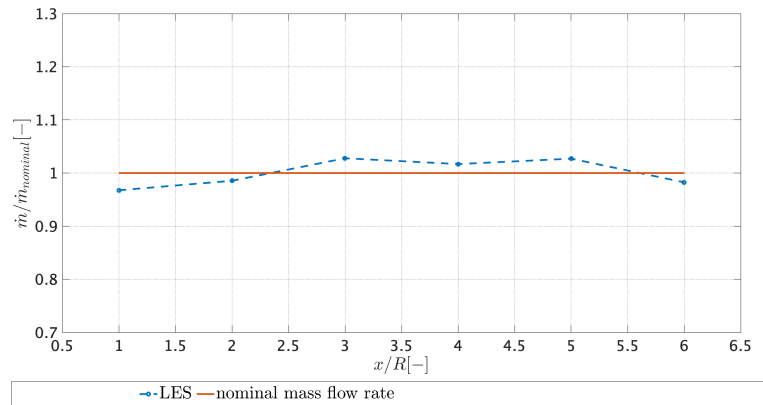
Figure 6.13: Mass flow rate in the combustion chamber of LES 50%, computed with time-averaged quantities.

6.2.   Non-reactive methane LES

This section employs a non-reactive full methane LES to investigate the impact of density fluctuation on the flow field generated by swirling flow, with the aim of enhancing our knowledge in this regard. The density of air is specifically modified by a 4% increment using the inflow turbulence generator, and the examination of the flow field involves a comparison between the findings obtained from the numerical simulation and the existing in-house Particle Image Velocimetry (PIV) data. The density of methane is kept unaltered due to its lack of influence, mostly attributed to the air-to-fuel ratio exceeding 20 on a mass basis at the specified equivalency ratio. Moreover, the characteristics of the fuel are determined by the comprehensive chemical data provided in tabular form, making it impractical to intervene in that regard.

Initially, a thorough examination of the mass flow rate is conducted throughout the combustion chamber to ascertain if the induced changes in density result in proportional variations in the mass flow rate.
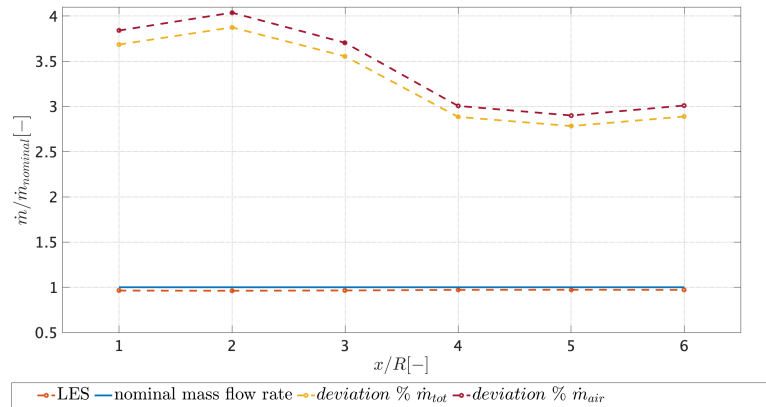
Figure 6.14: Mass flow rate in the combustion chamber.

The data shown in figure

Figure 6.15 presents a comparison of the radial profile of axial velocity between LES and PIV. On one hand, it is anticipated that the axial velocity would be comparatively lower than that of experiments as a result of the increased air density that is applied. In contrast, it can be shown from figure 6.15 that the LES method yields greater values for axial velocities.
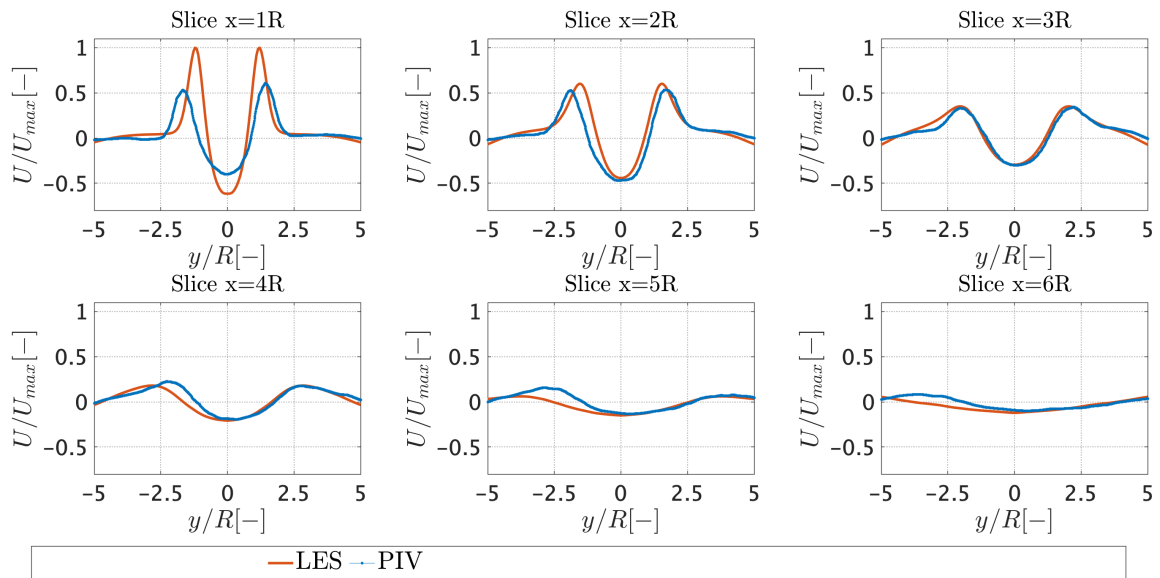
Figure 6.15: LES Favre-filtered time-averaged radial distribution of the axial velocity against PIV.

It is evident that downstream of $x/R = 1$, there is a notable level of agreement, since both the positioning of velocity peaks and the central recirculation zone are precisely

predicted. In relation to the streamwise axial position $x/R = 1$, a discrepancy is evident: the locations of the velocity peaks are quite well predicted, whereas the maximum and lowest velocities are much inaccurate.

The diagram illustrates the axial velocity distribution in the first six radii of the combustion chamber, comparing the numerical and the experimental results. The alignment between the jet's aperture and the CRZ downstream is remarkable. Nevertheless, it is worth noting that the axial velocity within the firts radius upon entering the combustion chamber exhibits a much greater magnitude compared to the experimental value.

(a) PIV   (b) LES
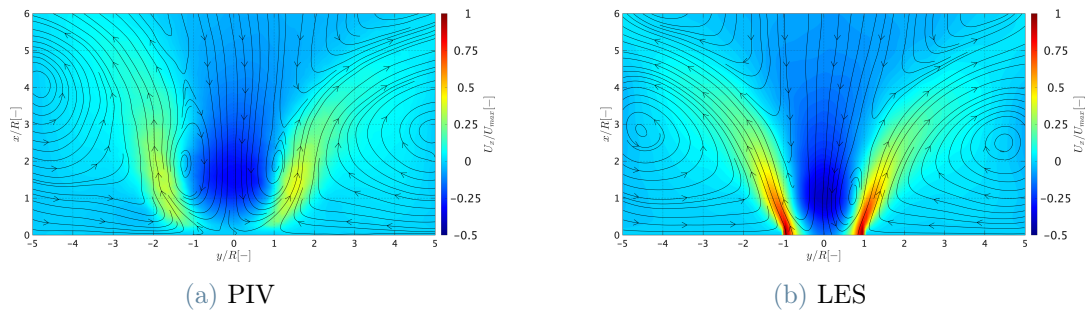
Figure 6.16: Colormap representing a) PIV axial velocity b) the axial velocity of the LES 50% in the combustion chamber. Streamlines are depicted for the velocity field.

Three causes have been identified to explain the discrepancy:

- The temperature field exhibits a value that surpasses the prescribed boundary condition, as seen in figure 6.17, despite the absence of any reactions (i.e., absence of heat release) and the adiabatic assumption of the case. Upon examination of the scatterplots depicting the enthalpy of formation obtained from the thermochemistry tabulation, it becomes evident that the observed trend within the flammability limits of methane is non-linear. This non-linearity indicates that the representation of the methane-air mixture is inadequate, leading to temperature oscillations. The elevated $\langle \tilde{T} \rangle$ inside the mixing tube, which attains a maximum value of 10% relative to the boundary condition, results in the expansion of the mixture, hence causing acceleration. However, the acceleration resulting from this expansion is insufficient to account for the observation that the velocity peak of the LES is twice as high as that of the PIV at $x/R = 1$. A 10% deviation in temperature would result in a 10% reduction in density according to the ideal gas equation of state. Consequently, the acceleration of the flow would increase by 10% in accordance with the principle of mass conservation. Hence, this discrepancy of 100% cannot be accounted for only by the aforementioned explanation.
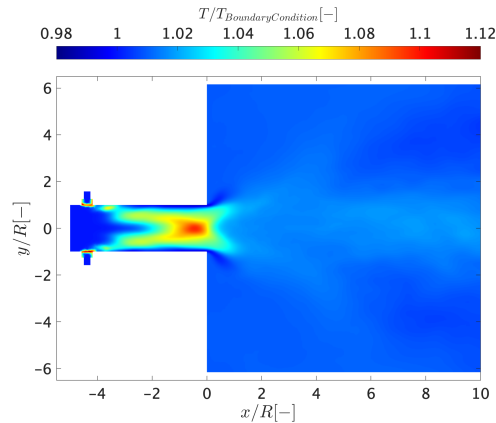
Figure 6.17: $\langle \tilde{T} \rangle$ field in the mixing tube and first portion of the combustion chamber.

- On one side, the introduction of a density augmentation would likely result in a reduction of the velocity peaks. Consequently, a reduction in the axial flow of axial momentum would occur, resulting in an augmentation of the swirl number at the inlet of the combustion chamber, so initiating a more intense vortex breakdown phenomenon. Consequently, an elevated axial component of the negative pressure gradient along the centerline would give rise to a stronger reverse flow, so mitigating the impact of increased density on the reduction in axial velocity, and possibly leading to a lower negative value for the axial velocity in the CRZ.

- It is possible that the radial component of the gradient of mixture fraction in the vicinity of $x = 1R$ exhibits an elevated value compared to the experimental observed behavior. Figure 6.18 represent the field of $\langle \tilde{z} \rangle$. The experimental findings indicate that the fuel-air mixture inside the center of the jet is leaner, while it becomes richer in the outer shear layer. This implies that the LES model would predict a less effective mixing compared to the actual observed mixing. Undoubtedly, a leaner mixture at the core of the jet would lead to higher density and consequently reduced axial velocity; conversely, a richer mixture at the outer shear layer would result in decreased density and increased axial velocity, since the density of methane is considerably lower than that of air.
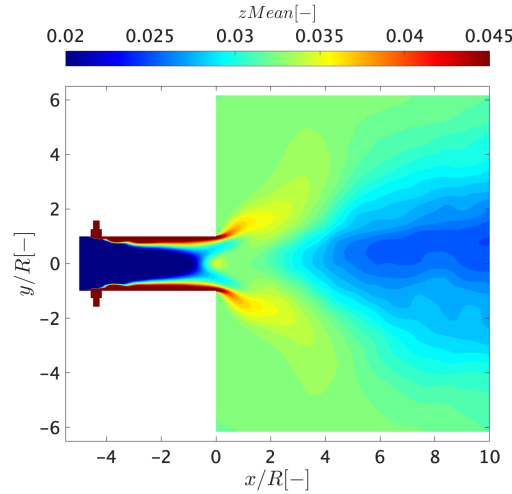
Figure 6.18: $\langle \tilde{z} \rangle$ field in the mixing tube and first portion of the combustion chamber.

In conclusion, due to the intricate nature of the phenomenon under investigation, the impact of density variations on swirling flow cannot be definitively ascertained using just a single Large Eddy Simulation (LES).

6.3.   Reactive full methane LES

In this section, we examine the analysis of the reactive full methane LES. The process of ignition is achieved by placing a cylindrical field at the entrance of the combustion chamber, where the progress variable is set to a value of 1 and the temperature is set to $1500[K]$. It is important to note that the flamelet model used in this study does not include autoignition. The validation of the LES involves a comparison between the flow field obtained from the simulation and the PIV data. Additionally, a preliminary analysis is conducted to assess the emission of nitrogen oxide (NO). This analysis includes a comparison between the experimental results, the estimated NO values from tabulated data, and the performance of an alternative model that incorporates an additional transport equation for the NO mass fraction and provide modeling for its reaction rate, which is splitted in a source and a sink term that depends on the concentration of NO itself and requires thus modeling. The methodology used in this is extensively described in the work conducted by Pitsch et al. [16].

6.3.1.   Validation against PIV

Initially, a reactive LES is conducted, using a 0% correction of tangential velocity in the inflow turbulence generator. The simulation is performed assuming perfect premixing

conditions, which serves as an initial step towards comprehensively analyzing the flow field and subsequently comparing it to the available PIV data. The mixture fraction is uniform, resulting in the flame burning homogeneously at the global equivalency ratio. The effect of this uniformity on the temperature field is important, as it leads to a pattern of flow field acceleration that is considerably distinct from real-world observations.

In reality, the process of combustion demonstrates variations in fuel-air mixture composition, characterized by a much leaner mixture at the jet's core and a richer mixture at the outer shear layer. These differences occur due to the non-instantaneous mixing process and result in substantial temperature fluctuations along the flame. As a result, the flow field demonstrates non-uniform acceleration due to expansion, which is lower when compared to the acceleration predicted by the LES. It is worth noting that, under the hypothesis of perfect premixing, this LES is not solving the mixing complexities and hence is not expected to precisely match PIV data, as shown in figure 6.19:

(a) PIV   (b) LES

Figure 6.19: Colormap representing a) PIV axial velocity b) the axial velocity of the LES 50% in the combustion chamber. Streamlines are depicted for the velocity field.

The LES flame demonstrates the absence of flashback and achieves stabilization inside the shear layers while maintaining attached to the burner. The phenomenon of vortex breakdown does not manifest, resulting in the absence of a central recirculation zone. The magnitude of velocity exhibits a significant disparity when comparing it to particle image velocimetry, with the jet's aperture being comparatively narrower.

It is evident that the assumption of perfect premixing is too strong, since the mixing process encompasses many length scales and temporal scales. The inclusion of fuel ports inside the domain facilitates the precise resolution of the mixing process and enables the prediction of a flow field that aligns more closely with experimental data.
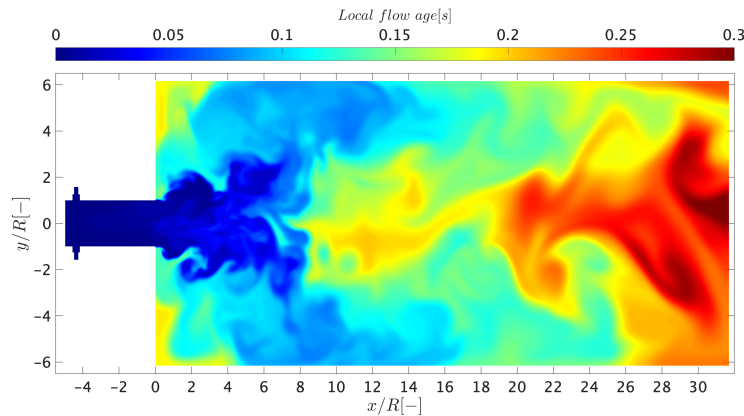
Figure 6.20: Contour plot of the local flow age within the combustor for the reactive methane case.

As seen in Figure 6.20, the observed residence time is roughly 300 milliseconds, which is notably lower than the corresponding value in the non-reactive scenario, amounting to approximately one third of the latter. The acceleration of the mixture occurs as a result of expansion inside the high-temperature flame zone, leading to a decrease in the overall flow age. This phenomenon is advantageous in terms of computing cost, since a lower flow through time results in a decreased simulation time. A single flow through time was sufficient to initiate the process of time averaging, and around 150 milliseconds were found to be enough for obtaining the averages (i.e., there was no significant change seen when extending the duration for which the time-averages were computed).

Figure 6.21 presents a comparative analysis of the axial velocity's radial profile at various streamwise positions within the combustion chamber. It is evident that the LES fails to properly estimate the velocity magnitude at any location inside the combustion chamber. However, the precise location of the peaks in the radial position of the axial velocity is captured quite accurately, particularly at initial axial locations. Furthermore, accurate prediction of the minimum velocity of the CRZ is seen downstream from the first axial position. The observed discrepancy between the reactive and non-reactive cases, where the PIV profiles where predicted very accurately by the LES, may be attributed to a variety of factors.
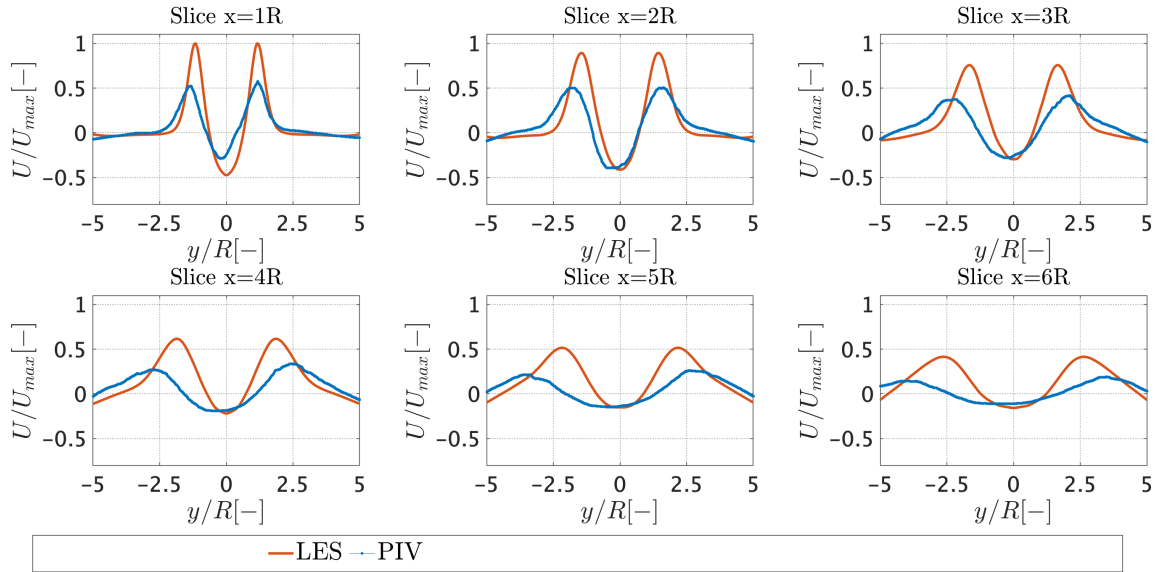
Figure 6.21: LES Favre-filtered time-averaged radial distribution of the axial velocity against PIV.

In the context of reactive systems, the interplay between chemistry and turbulent swirling flow is a complex phenomenon. The acceleration of the mixture across the turbulent flame brush is influenced by thermal expansion. This acceleration is dependent upon the temperature field, which in turn is affected by the distribution of mixture fraction, that is a determining factor in controlling the local heat release. The flow field, thus, plays a role in influencing combustion via the process of mixing and, at the same time, it is influenced by the flame itself through the increase of temperature, leading to thermal expansion. This expansion, in turn, causes a fall in the Reynolds number due to the increased viscosity, possibly provoking a relaminarization of the flow.

On top of this, the assumption of adiabatic walls plays a significant role in this context. It should be noted that the simulated temperature field tends to be higher than the experimental results due to the neglect of heat losses to the surrounding environment and, far more importantly, a less homogeneous mixture fraction field. These heat losses are particularly significant in magnitude when dealing with the elevated temperatures associated with methane combustion, even in a lean configuration. The unaccounted heat losses may provide a partial explanation for both the higher velocities seen in the combustion chamber and the fact that experimental observation show a lifted flame, whereas the LES predicts a flame attached to the burner 6.22. Indeed, thermal losses have the effect of reducing the temperature field, hence resulting in a decrease in the turbulent flame speed. The flame is forced to stabilize in a downstream region, where a reduced

flow velocity is seen as a result of the presence of the central recirculation zone. From this viewpoint, it may be deduced that the LES model is more prone to predict flashback occurrence than what happens in reality. One potential approach to improve the alignment with PIV is to implement a five-dimensional tabulation into the flamelet model. This tabulation would include the specific enthalpy, progress variable, mixture fraction, and their respective variances. This approach would enable the elimination of the assumption of adiabatic walls and include considerations for heat losses.

Nonetheless, the primary cause of the flow field misprediction is mainly attributed to the inadequate resolution of mixing: as illustrated in figure 6.18 an important amount of mixing occurs in the boundary layer, where it is not resolved but modeled using wall functions. This may result in a mixture fraction field that is more heterogeneous, producing zones that are richer and therefore higher in temperature. These zones have the dual effect of increasing the mixture's acceleration and shifting the stabilization position of the flame upstream as a result of the higher turbulent flame speed. One potential method for improving mixing within the boundary layer involves modifying the employed wall functions in a manner that results in an increased turbulent viscosity ν_t. This heightened turbulent viscosity serves to enhance the diffusion of various quantities, including momentum and species mass fraction.

| (a) PIV | (b) LES |
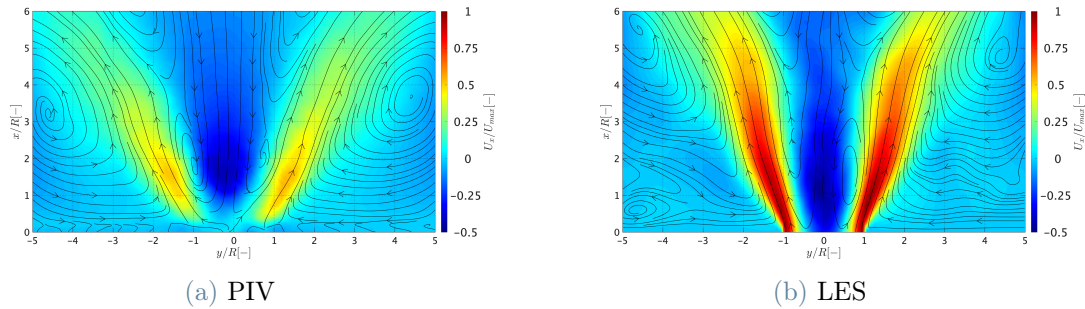
Figure 6.22: Colormap representing a) PIV axial velocity b) the axial velocity of the LES 50% in the combustion chamber. Streamlines are depicted for the velocity field.

However, the study conducted by Pitsch et al [16] show that by using Large Eddy Simulation on a Sandia flame D, and utilizing a flamelet model together with the assumption of adiabatic walls, it is possible to obtain good predictions of the flow field even without considering heat losses. This finding suggests that the adiabatic assumption does not have primary significance for what concern the prediction of the flow field, and it is essential to take into account other factors. The comparison of the mixture fraction field between LES and experimental data might provide valuable insights. This analysis would help de-

termine if the mixing process is correctly captured by the LES or whether the predicted mixing is worse, as previously shown in the analysis of the non-reactive full methane LES. In addition to density, the presence of a distinct mixture fraction in the reactive scenario would have a more pronounced negative impact due to its significant influence on heat release and subsequent flame stabilization. This influence is manifested by variations in the acceleration pattern of the flow field and the turbulent flame speed.

The reaction rate of the progress variable, temperature, and progress variable fields are shown in Figure 6.23a, Figure 6.23b, and Figure 6.23c, respectively. The reaction rate is higher in regions where the mixture is more concentrated, resulting in the attainment of elevated temperatures in localized areas. There are no discernible temperature peaks seen inside the combustion chamber, indicating that the anticipated mixing process did not facilitate the formation of localized regions with a high fuel concentration. Based on the analysis of the mean temperature field, it can be concluded that the LES predict no occurrence of flashback. This observation aligns with experiments using 0% axial air injection, where flashback was not detected.
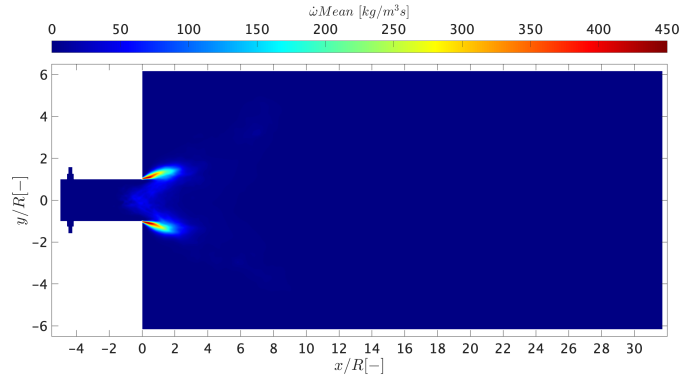
(a) Mean reaction rate of the progress variable $\langle \tilde{\dot{\omega}} \rangle$.
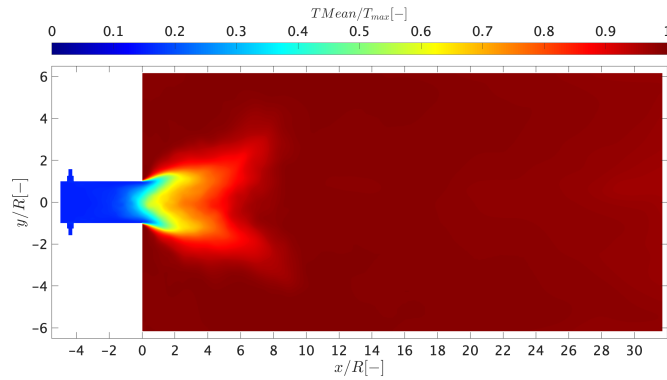
(b) Mean temperature field $\langle \tilde{T} \rangle$.
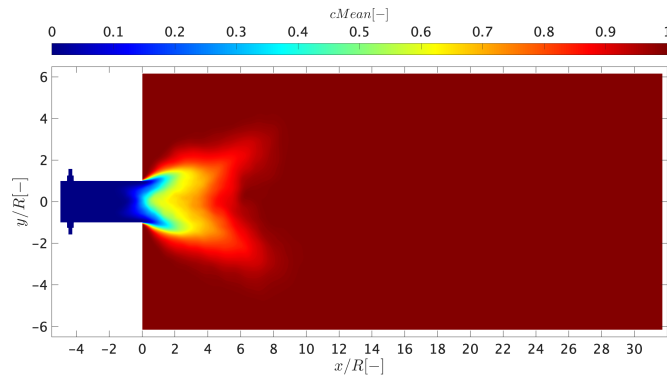
(c) Mean progress variable $\langle \tilde{c} \rangle$.

Figure 6.23: Contour of the mean reaction rate of the progress variable $\langle \tilde{\dot{\omega}} \rangle$, mean temperature field $\langle \tilde{T} \rangle$ and mean progress variable $\langle \tilde{c} \rangle$ within the combustor.

6.3.2. NO prediction

This section presents scatterplots of the source term of NO and the mass fraction of nitrogen monoxide Y_{NO} versus temperature, mixture fraction, and local flow age fields. These scatterplots aim to analyze the emissions in the TUDelft combustor under the set operat-

ing point and the performance of the model proposed in [16]. The substantial sensitivity of the source term with temperature is seen in Figure 6.24. This sensitivity arises from the exponential dependence of the forward rate constant in the Zeldovich mechanism. The scatterplot illustrates a correlation between the proximity to the adiabatic flame temperature and the increasing significance of nitric oxide formation. This observation serves as evidence supporting that the thermal route is the primary mechanism for the creation of NO if temperatures are high enough.

(a) (b)
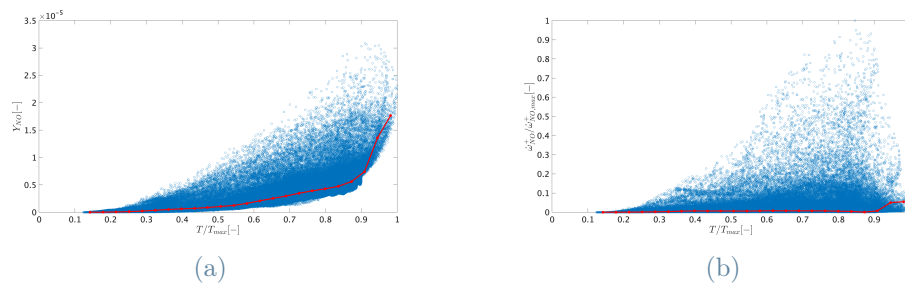
Figure 6.24: Scatterplot of a) mass fraction of nitric oxide $\tilde{Y}_{NO}$ and b) normalized source term of nitric oxide $\overline{\dot{\omega}}^{+}_{NO}$ against temperature $\tilde{T}$. The conditional mean over 25 bins is highlighted in red.

Figure 6.25 illustrates the correlation between the source term of NO and the mixture fraction, whereby the stoichiometric value is emphasized in the color black. The range of the x-axis has been restricted to include just the flammability range of methane when mixed with air. It is evident that not only the Zeldovich mechanism is important, as we can see from the lean-fuel part, but also the prompt mechanism is playing a role in the production of nitric oxides, as the source term is elevated also in the rich region near stochiometric.
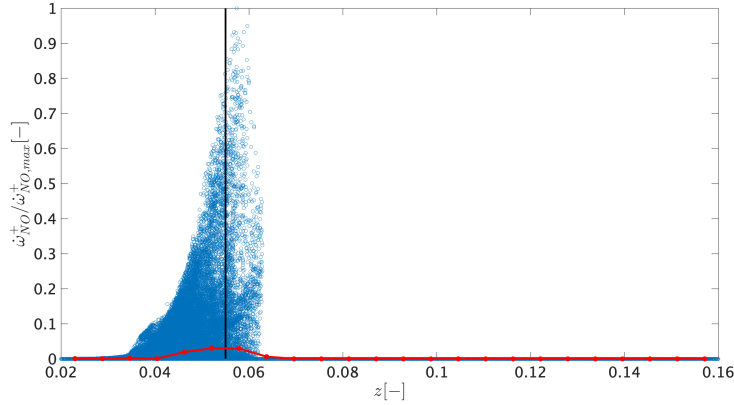
Figure 6.25: Scatterplot of normalized source term of nitric oxide $\overline{\dot{\omega}}^+_{NO}$ against mixture fraction $\tilde{z}$. The conditional mean over 25 bins is highlighted in red.

It is worth noting that achieving a fast transition between fuel-rich and fuel-lean regions is crucial for the reduction of NO_x emissions, as it helps prevent prolonged residence times near the stoichiometric condition. The attainment of this objective may be accomplished by the implementation of an efficient blending process, which is capable of achieving perfect premixing of the fuel and oxidizer prior to their introduction into the combustion chamber. The swirler serves a valuable function in this regard, as it contributes to the improvement of mixing.

Additionally, the analysis of figure 6.26 in conjunction with the contour plot depicting the local flow age shown in figure 6.20, provides valuable insights into the specific regions inside the combustion chamber where the generation of nitric oxides occurs. The production is effectively nonexistent until the fresh mixture reaches the combustion chamber, as shown by the first $20[ms]$ of observation, which is obvious given that no reactions are occurring. Subsequently, the emission formation begins next to the burner, where the flame achieves stability, and persists at heightened levels within the central recirculation zone and outer recirculation zone. This may be attributed to the combined effects of greater temperatures and prolonged residence time. In downstream areas characterized by a local flow age exceeding 180 milliseconds, the source term of NO diminishes significantly, resulting in a cessation of production.
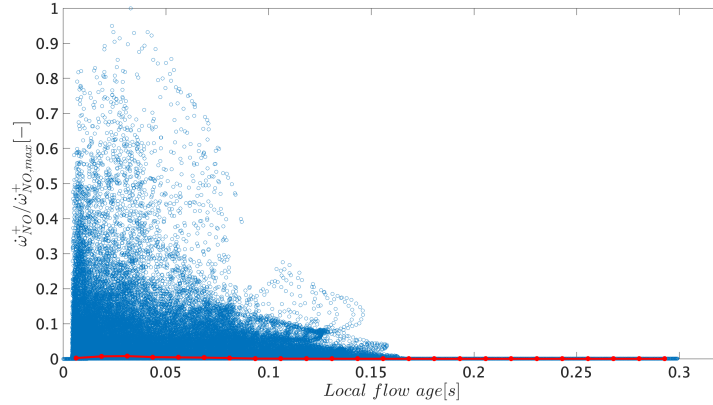
Figure 6.26: Scatterplot of normalized source term of nitric oxide $\overline{\dot{\omega}}_{NO}^{+}$ against local flow age. The conditional mean over 25 bins is highlighted in red.

The time-averaged field $\langle \tilde{Y}_{NO} \rangle$, as predicted using the methodology presented by Pitsch et al [16], is shown in Figure 6.27.

(a) Transport equation
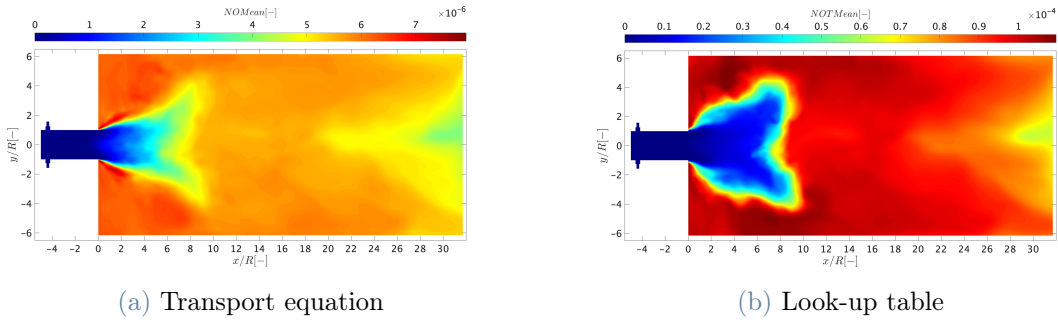
(b) Look-up table

Figure 6.27: Contours of a) time-averaged mass fraction of nitric oxide $\langle \tilde{Y}_{NO} \rangle$ computed with the method proposed by [16] and b) time-averaged mass fraction of nitric oxide $\langle \tilde{Y}_{NO} \rangle$ retrieved by the look-up table.

The predicted emissions of nitrogen oxide (NO) are about ten times lower than the expected values obtained from the retrieval from the look-up table. Specifically, when averaging throughout the outlet cross section, the former yields a value of $\langle \tilde{Y}_{NO} \rangle = 4.45e - 06[-]$, while the latter yields a value of $\langle \tilde{Y}_{NOT} \rangle = 6.91e - 05[-]$. The use of the transport equation technique demonstrates a significant improvement in the accuracy of the prediction, as shown by the comparison with the experimental value of $Y_{NO} = 3.7e - 06$. Specifically, the percentage of error decreased from 1767.57% to 20.33%. This reduction in error leads to a value which is quite close to the actual findings, despite the fact that the flow field does not align with the experimental data in the reactive

scenario. The use of pre-tabulated chemistry has dramatically limited effectiveness in accurately estimating emissions of nitric oxides. However, the research conducted in [16] significantly improves the flamelet model in addressing this issue.

The temperature sensitivity of NO, being most of it produced via the Zeldovich mechanism, suggests that the accurate modeling of the temperature by accounting for radiation and wall heat losses is of paramount importance for its prediction. Although the flamelet model used in this study does not include enthalpy as a fifth parameter and assumes adiabatic walls, the predictions obtained by large eddy simulation exhibit a good agreement with experimental findings. Figure 6.28 show the field of source and sink term that makes up the reaction rate of NO.

(a) Source of nitric oxides   (b) Sink of nitric oxides
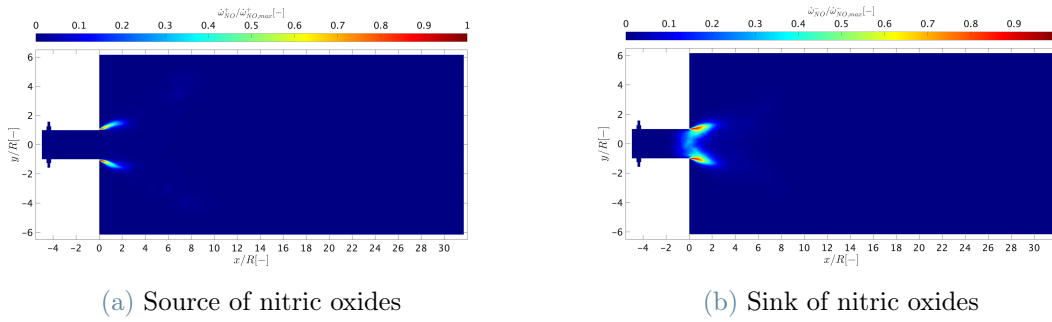
Figure 6.28: Contours of a) time-averaged normalized source term of nitric oxide $\langle \overline{\dot{\omega}}^{+}_{NO} \rangle$ and b) time-averaged normalized sink term of nitric oxide $\langle \overline{\dot{\omega}}^{+}_{NO} \rangle$.

7 | Conclusions and Future work

7.1. Conclusions

The prevailing emphasis on environmental concerns and the pursuit of sustainability has led to a notable transition away from traditional fossil fuel-based methods of power production towards more ecologically viable alternatives. Among the available options, hydrogen combustion in gas turbines emerge as a very promising solution. Hydrogen exhibits considerable appeal in terms of sustainability due to its capacity to facilitate the eradication of carbon emissions and the abatement of nitric oxide formation if used in lean-premixed technology thanks to the possibility to control the flame temperature. Moreover, the possibility to exploit hydrogen's wide flamability range in ultra-lean combustors makes it even more appealing. Nevertheless, the distinctive characteristics of hydrogen, including its reactivity and diffusivity, provide difficulties such as flashback [5–7], which impede the extensive use of this technology.

In the present context, the use of axial air injection is being acknowledged as a feasible approach to address the potential hazards associated with flashback [10, 11]. Additionally, the utilization of lean-premixed hydrogen flames is applied to control the upper limit of temperature, thus reducing the emissions of nitrogen oxides (NO_x). The use of this technologies enhances the feasibility of hydrogen combustion in gas turbines in their role in promoting a more environmentally sustainable aviation. The primary objective of this study is to examine the flow characteristics of a lean premixed combustor, which is stabilized using a swirler. The purpose of this investigation is to verify the in-house developed Large Eddy Simulation model, which will subsequently be used to analyze scenarios including methane-hydrogen blends and pure hydrogen. One additional aim of the study was to evaluate the efficacy and feasibility of using a novel flamelet-based approach for predicting NO_x emissions developed by Pitsch et al [16]. In order to examine the combustion system, the LES approach is used in conjunction with the flamelet model with beta presumed Probability Density Function (PDF). OpenFOAM software is used for conducting these lean-premixed combustion simulations, under atmospheric pressure, whereby tabulated chemistry is taken into account with GRI-Mech 3.0 [41]. The geometry

corresponds to the laboratory-scale combustor used at TUDelft. The primary objective is to calibrate the LES model for non-reactive simulations. This was achieved by doing a sensitivity analysis on the swirl number. Consequently, there was a notable alignment between the in-house Particle Image Velocimetry data and the predictions, resulting in accurate estimation of the jet's aperture and central recirculation zone inside the combustion chamber. These characteristics play a crucial role in precisely representing the flame stabilization process. Subsequently, an attempt was made to assess the impact of density variation on the flow field resulting from vortex breakdown. This was achieved by conducting a Large Eddy Simulation for a full methane non-reactive case. However, the desired inference could not be achieved owing to the reasons elaborated upon in this thesis. Finally, the present study conducted the reactive full methane case for validation purposed and to verify the accuracy of the LES model and evaluate the efficacy of the methodology proposed by Pitsch for predicting nitrogen oxide NO_x emissions. It has been determined that additional analysis is required to validate the reactive LES model from a flow-field perspective, likely due to the manner in which the mixing is resolved in the LES. However, the prediction of NO_x emissions demonstrated a high level of accuracy, and it was observed that the new approach for nitric oxides emissions prediction is significantly more effective compared to the tabulated method.

7.2.   Future work

This section presents recommendations for future endeavors that align with the objectives of the APPU projects. The subject matter can be categorized into two distinct areas: global sensitivity analysis and hydrogen LESs.

7.2.1.   Global sensitivity analysis

Global sensitivity analysis (GSA) refers to the investigation of how uncertainty in the output variable Y of a model, can be allocated to various sources of uncertainty in the input variables X_i of the model [82]. The various methods for conducting GSA are documented in [83]. These include the Fourier amplitude sensitivity test (FAST), Monte Carlo-based regression-correlation indices, and Sobol's variance-based method. The latter have been chosen due to its favorable characteristics [84]: the influence of the input incorporates the effect of the range of input variation (global SA instead of local SA) and its PDF evaluate the effect of a factor while all the others are varying as well; furthermore this method works regardless of the additivity or linearity of the model (i.e. model independency). Finally, it has the ability to catch the interaction between inputs (i.e. effect of changing two

factors is different from the sum of their individual effects), which is extremely important for a non-linear non-additive model like our reactive simulations. Monte Carlo integration enables the computation of Sobol indices S_i and S_T, which can be conveniently accomplished using the modular code 'SAFE' [85]. In conclusion, the objectives of a GSA are to identify the most important factors X_i (defined as the one that if fixed to its true, despite unknown, value would lead to the greatest reduction in the variance of Y) that deserves better experimental measurements or further optimization. Furthermore, an additional objective is to minimize the variance of the variable Y, denoted as $V(Y)$, such that it reaches a predetermined threshold value V_r, while simultaneously controlling the fewest possible number of factors.
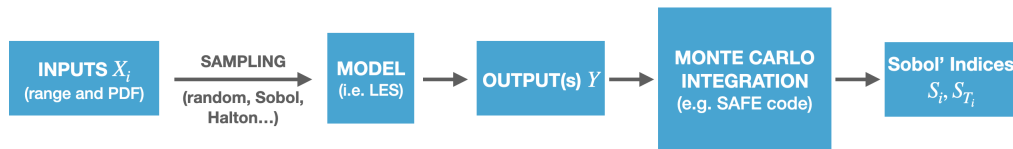
Figure 7.1: Scheme of the Variance-based Sobol' method for Global sensitivity analysis.

An issue may arise with very expensive models, such as LES. Therefore, it is necessary to identify a method for reducing the computational cost. The GSA is impracticable due to the fact that Saltelli's method [84] necessitates $N(k+2)$ iterations for a complete set of S_i and S_T, where N (the 'base sample') can range from a few hundred up to a few thousand. Utilizing an emulator, such as the Gaussian Process, which is a mathematical function whose behavior closely resembles that of the original model and would enable us to generate estimates of model output at untested points without rerunning the simulation model, is identified as a solution to this problem. One benefit is that the sample size required to fit a surrogate model to the original can be reduced to an order of tens. Subsequently, the Monte Carlo calculations can be performed on the surrogate model, which remains expensive but feasible.

The suggestion is to conduct a global sensitivity analysis in order to identify critical parameters for future optimization endeavors. The proposed work is to utilize $Y = \{Y_{NO}$ at the outlet of the combustion chamber, Δp across the combustion chamber, variance of mixture fraction in a selected cross section of the mixing tube$\}$ as model output and considering $X_i = \{Sw, p, \%AAI, \phi \text{ or } \dot{m}\}$ as model's input keeping a constant thermal power and fuel composition in terms of hydrogen/methane blend. By calculating the Sobol' indices S_i and S_T, the relative importance of the specified input parameters can be determined. This examination facilitates the identification of crucial parameters for

subsequent optimization.

7.2.2. Hydrogen LESs

An assumed probability density function is utilized to represent the flame-turbulence interaction in the current study, which employs LES with flamelets-based thermochemistry to examine the flow field and emissions within the swirled technically premixed laboratory combustor with AAI at TU Delft. The flamelets/PDF combustion closure has demonstrated efficacy when applied to hydrocarbon flames; however, its suitability for hydrogen remains uncertain, primarily attributable to differential diffusion effects. A further work is to conduct 100% hydrogen LESs to provide insights into the differential diffusion modeling that was developed within the research group of TU Delft. This investigation would focus on the modeling's capability to accurately predict the flow field in a swirled flow configuration under the assumption of PDF closure. The present study's analysis would be expanded to include H_2/air combustion at the identical power setting, although with an elevated AAI to prevent flashback. The objective would be to assess the effectiveness of the LES closure and determine how differential diffusion modeling affects the predicted mixing, temperature field, and NO emissions. Two models for differential diffusion would be tested and results would be compared against time-resolved flow field measurements obtained by Particle Image Velocimetry, OH^* chemiluminescence and exhaust gas composition in terms of CO, CO_2 and NO.

Experimental and numerical analyses demonstrate that the mixing of fuel and oxidizer is the most influential factor in flame stabilization, emission levels, and temperature. This provides the motivation for additional investigations into full hydrogen flames, where it is anticipated that axial air injection will significantly alter the swirling flow field in the mixing tube and, by extension, the conditions under which the flame burns. It has been previously observed that the incorporation of differential diffusion modeling improves mixing and influences the distribution of equivalence ratios at the combustion chamber's entrance. Furthermore, it was observed that the fluctuations in the local equivalence ratio on the flame front, as predicted by the model, have an impact on the location of flame stabilization, local temperature, and NOx emissions. A numerical investigation is conducted to gain a deeper comprehension of these behaviors and the characteristics of the hydrogen flame in relation to differential diffusion effects; the results are then compared with the experimental data.

Bibliography

[1] David Noble, David Wu, Benjamin Emerson, Scott Sheppard, Tim Lieuwen, and Leonard Angello. Assessment of current capabilities and near-term availability of hydrogen-fired gas turbines considering a low-carbon future. *Journal of Engineering for Gas Turbines and Power*, 143, 4 2021. `doi:10.1115/1.4049346`.

[2] Eun Seong Cho and Suk Ho Chung. Improvement of flame stability and nox reduction in hydrogen-added ultra lean premixed combustion. *Journal of Mechanical Science and Technology*, 23:650–658, 6 2009. `doi:10.1007/s12206-008-1223-x`.

[3] Gioele Ferrante, Lennard Doodeman, Arvind Gangoli Rao, and Ivan Langella. Les of hydrogen-enriched methane flames in a lean-burn combustor with axial air injection.

[4] Jadeed Beita, Midhat Talibi, Suresh Sadasivuni, and Ramanarayanan Balachandran. Thermoacoustic instability considerations for high hydrogen combustion in lean premixed gas turbine combustors: A review. *Hydrogen*, 2:33–57, 1 2021. `doi:10.3390/hydrogen2010003`.

[5] Ivan Langella, Johannes Heinze, Thomas Behrendt, Lena Voigt, Nedunchezhian Swaminathan, and Marco Zedda. Turbulent flame shape switching at conditions relevant for gas turbines. *Journal of Engineering for Gas Turbines and Power*, 142, 1 2020. `doi:10.1115/1.4044944`.

[6] Alessandro Soli and Ivan Langella. Numerical investigation of a coupled blow-off/flashback process in a high-pressure lean-burn combustor. *Journal of Engineering for Gas Turbines and Power*, 145, 2 2023. `doi:10.1115/1.4055483`.

[7] Thomas F. Fric. Effects of fuel-air unmixedness on no, emissions.

[8] Gorkem Oztarlik, Laurent Selle, Thierry Poinsot, and Thierry Schuller. Suppression of instabilities of swirled premixed flames with minimal secondary hydrogen injection. *Combustion and Flame*, 214:266–276, 4 2020. `doi:10.1016/j.combustflame.2019.12.032`.

[9] F. Kiesewetter, M. Konle, and T. Sattelmayer. Analysis of combustion induced

vortex breakdown driven flame flashback in a premix burner with cylindrical mixing zone. *Journal of Engineering for Gas Turbines and Power*, 129:929–936, 10 2007. `doi:10.1115/1.2747259`.

[10] G. Baumgartner and T. Sattelmayer. Experimental investigation on the effect of boundary layer fluid injection on the flashback propensity of premixed hydrogen-air flames.

[11] Thoralf G. Reichel, Katharina Goeckeler, and Oliver Paschereit. Investigation of lean premixed swirl-stabilized hydrogen burner with axial air injection using oh-plif imaging. *Journal of Engineering for Gas Turbines and Power*, 137, 11 2015. `doi:10.1115/1.4031181`.

[12] Thoralf G. Reichel, Steffen Terhaar, and Oliver Paschereit. Increasing flashback resistance in lean premixed swirl-stabilized hydrogen combustion by axial air injection. *Journal of Engineering for Gas Turbines and Power*, 137, 7 2015. `doi:10.1115/1.4029119`.

[13] C. Mayer, J. Sangl, T. Sattelmayer, T. Lachaux, and S. Bernero. Study on the operational window of a swirl stabilized syngas burner under atmospheric and high pressure conditions. *Journal of Engineering for Gas Turbines and Power*, 134, 2012. `doi:10.1115/1.4004255`.

[14] J. Sangl, C. Mayer, and T. Sattelmayer. Dynamic adaptation of aerodynamic flame stabilization of a premix swirl burner to fuel reactivity using fuel momentum. *Journal of Engineering for Gas Turbines and Power*, 133, 2011. `doi:10.1115/1.4002659`.

[15] Appu project.

[16] Matthias Ihme and Heinz Pitsch. Modeling of radiation and nitric oxide formation in turbulent nonpremixed flames using a flamelet/progress variable formulation. *Physics of Fluids*, 20:055110, 5 2008. `doi:10.1063/1.2911047`.

[17] Stephen B Pope. Ten questions concerning the large-eddy simulation of turbulent flows. *New Journal of Physics*, 6:35, 3 2004. URL: `https://dx.doi.org/10.1088/1367-2630/6/1/035`, `doi:10.1088/1367-2630/6/1/035`.

[18] Denis Veynante and Luc Vervisch. Turbulent combustion modeling. URL: `www.elsevier.com/locate/pecs`.

[19] Ivan Langella. Large eddy simulation of premixed combustion using flamelets, 2015.

[20] A. Donini, R. J. M. Bastiaans, J. A. van Oijen, and L. P. H. de Goey. A 5-d

implementation of fgm for the large eddy simulation of a stratified swirled flame with heat loss in a gas turbine combustor. *Flow, Turbulence and Combustion*, 98:887–922, 4 2017. `doi:10.1007/s10494-016-9777-7`.

[21] Fabio Cozzi. Slides of the course 'combustione e sicurezza'. 2023.

[22] Charles David Pierce. Progress-variable approach for large-eddy simulation of turbulent combustion, 2001.

[23] Poinsot, thierry and veynante, denis - theoretical and numerical combustion (2012).

[24] S. Mathur, P. K. Tondon, and S. C. Saxena. Thermal conductivity of binary, ternary and quaternary mixtures of rare gases. *Molecular Physics*, 12:569–579, 1967. `doi:10.1080/00268976700100731`.

[25] Stephen B Pope. Turbulent flows.

[26] Paul A. Libby and K. N.C. Bray. Countergradient diffusion in premixed turbulent flames. *AIAA Journal*, 19:205–213, 1981. `doi:10.2514/3.50941`.

[27] A. Valera-Medina. Coherent structures and their effects on processes occurring in swirl combustors. 5 2009.

[28] Wen huei Jou and Suresh Menon. Large-eddy simulations of combustion instability in an axisymmetric ramjet combustor. *Combustion Science and Technology*, 75:53–72, 1 1991. `doi:10.1080/00102209108924078`.

[29] S. Ghosal and P. Moin. The basic equations for the large eddy simulation of turbulent flows in complex geometry. *Journal of computational physics*, pages 24–37, 1995.

[30] Charles Meneveau and Joseph Katz. Scale-invariance and turbulence models for large-eddy simulation, 2000. URL: `www.annualreviews.org`.

[31] Benoît Fiorina, Denis Veynante, and Sébastien Candel. Modeling combustion chemistry in large eddy simulation of turbulent flames. *Flow, Turbulence and Combustion*, 94:3–42, 1 2015. `doi:10.1007/s10494-014-9579-8`.

[32] G. Lecocq, S. Richard, O. Colin, and L. Vervisch. Gradient and counter-gradient modeling in premixed flames: Theoretical study and application to the les of a lean premixed turbulent swirl-burner. *Combustion Science and Technology*, 182:465–479, 2010. `doi:10.1080/00102200903462920`.

[33] J. A. van Oijen, A. Donini, R. J.M. Bastiaans, J. H.M. ten Thije Boonkkamp, and L. P.H. de Goey. State-of-the-art in premixed combustion modeling using flamelet generated manifolds, 11 2016. `doi:10.1016/j.pecs.2016.07.001`.

[34] N. Peters. The turbulent burning velocity for large-scale and small-scale turbulence. *Journal of Fluid Mechanics*, 384:107–132, 4 1999. `doi:10.1017/S0022112098004212`.

[35] James F. Driscoll, Jacqueline H. Chen, Aaron W. Skiba, Campbell D. Carter, Evatt R. Hawkes, and Haiou Wang. Premixed flames subjected to extreme turbulence: Some questions and recent answers, 1 2020. `doi:10.1016/j.pecs.2019.100802`.

[36] R Borghi and M Destriau. *Combustion and flames: chemical and physical principles; La combustion et les flammes*. 1998.

[37] Matthias Ihme and Heinz Pitsch. Les of a non-premixed flame using an extended flamelet/progress variable model, 2005.

[38] Zhi X. Chen, Ivan Langella, Nedunchezhian Swaminathan, Michael Stöhr, Wolfgang Meier, and Hemanth Kolla. Large eddy simulation of a dual swirl gas turbine combustor: Flame/flow structures and stabilisation under thermoacoustically stable and unstable conditions. *Combustion and Flame*, 203:279–300, 5 2019. `doi:10.1016/j.combustflame.2019.02.013`.

[39] Zhi X. Chen, Ivan Langella, Robert S. Barlow, and Nedunchezhian Swaminathan. Prediction of local extinctions in piloted jet flames with inhomogeneous inlets using unstrained flamelets. *Combustion and Flame*, 212:415–432, 2 2020. `doi:10.1016/j.combustflame.2019.11.007`.

[40] Chem1d. a one dimensional laminar flame code, 2021. URL: `https://github.com/thijsa93400/TUe_chem1d`.

[41] P. Gregory Smith, David M. Golden, Michael Frenklach, Nigel Moriarty, Boris Eiteneer, Mikhail Goldenberg, T. Bowman, R.K. Hanson, Soonho Song, W.C. Gardiner, V.V. Lissianski, and Zhiwei Qin. Gri-mech 3.0. URL: `http://www.me.berkeley.edu/gri_mech/`.

[42] Michael P Burke, Marcos Chaos, Yiguang Ju, Frederick L Dryer, Stephen J Klippenstein, and Senior Chemist. Comprehensive h 2 /o 2 kinetic model for high-pressure combustion, 2011.

[43] Andrew W. Cook and James J. Riley. A subgrid model for equilibrium chemistry in turbulent flows. *Physics of Fluids*, 6:2868–2870, 1994. `doi:10.1063/1.868111`.

[44] Javier Jiménez, Amable Liñán, Michael M. Rogers, and Francisco J. Higuera. A priori testing of subgrid models for chemically reacting non-premixed turbulent

shear flows. *Journal of Fluid Mechanics*, 349:149–171, 10 1997. `doi:10.1017/S0022112097006733`.

[45] C. Wall, B. J. Boersma, and P. Moin. An evaluation of the assumed beta probability density function subgrid-scale model for large eddy simulation of nonpremixed, turbulent combustion with heat release. *Physics of Fluids*, 12:2522–2529, 2000. `doi:10.1063/1.1287911`.

[46] Advanced turbulent combustion modeling for gas turbine application. `doi:10.6100/IR773140`.

[47] A. W. Vreman, B. A. Albrecht, J. A. van Oijen, L. P.H. de Goey, and R. J.M. Bastiaans. Premixed and nonpremixed generated manifolds in large-eddy simulation of sandia flame d and f. *Combustion and Flame*, 153:394–416, 5 2008. `doi:10.1016/j.combustflame.2008.01.009`.

[48] Toufik Boushaki. *Introductory Chapter: Swirling Flows and Flames*. IntechOpen, 6 2019. `doi:10.5772/intechopen.86495`.

[49] Chris Lawn. Unsteady combustor physics, tim c. lieuwen. cambridge university press (2012). 424 pp., £75, isbn: 978-1-107-01599-9. *Journal of Sound and Vibration*, 10 2013. `doi:10.1016/j.jsv.2013.04.016`.

[50] J H Faler and S Leibovich. Disrupted states of vortex flow and vortex breakdown. *The Physics of Fluids*, 20:1385–1400, 9 1977. `doi:10.1063/1.862033`.

[51] Shixiao Wang and Zvi Rusak. Axisymmetric vortex breakdown in a pipe. *ESAIM: Proceedings*, 1, 10 1997. `doi:10.1051/proc:1996037`.

[52] H J Sheen, W J Chen, S Y Jeng, and T L Huang. Correlation of swirl number for a radial-type swirl generator.

[53] J and NA Beer Chigier. Combustion aerodynamics. *Combustion Technology: Some Modern Developments*, 61, 2012.

[54] S Yuasa. Effects of swirl on the stability of jet diffusion flames, 1986.

[55] Douglas Feikema, Ruey-Hung Chen, and James F Driscoll. Enhancement of flame blowout limits by the use of swirl, 1990.

[56] A R Masri, P A M Kalt, and R S Barlow. The compositional structure of swirl-stabilised turbulent nonpremixed flames. *Combustion and Flame*, 137:1–37, 2004. URL: `https://www.sciencedirect.com/science/article/pii/`

S0010218003003006, `doi:https://doi.org/10.1016/j.combustflame.2003.12.004`.

[57] Zakaria Mansouri, Aouissi Mokhtar, and Toufik Boushaki. Detached eddy simulation of high turbulent swirling reacting flow in a premixed model burner. *Combustion Science and Technology*, 188:1777–1798, 12 2016. `doi:10.1080/00102202.2016.1211888`.

[58] F. Cozzi, A. Coghe, and R. Sharma. Analysis of local entrainment rate in the initial region of isothermal free swirling jets by stereo piv. *Experimental Thermal and Fluid Science*, 94:281–294, 6 2018.

[59] P Schmittel, B Gu¨nther, Gu¨ Gu¨nther, B Lenze, W Leuckel, and H Bockhorn. Turbulent swirling flames: Experimental investigation of the flow field and formation of nitrogen oxide, 2000.

[60] Aldo Coghe, Giulio Solero, and Gianfranco Scribano. Recirculation phenomena in a natural gas swirl combustor. *Experimental Thermal and Fluid Science*, 28:709–714, 9 2004. `doi:10.1016/j.expthermflusci.2003.12.007`.

[61] Toufik Boushaki, Nazim Merlo, Christian Chauveau, and Iskender Gökalp. Study of pollutant emissions and dynamics of non-premixed turbulent oxygen enriched flames from a swirl burner. *Proceedings of the Combustion Institute*, 36, 6 2016. `doi:10.1016/j.proci.2016.06.046`.

[62] Nazim, Toufik Boushaki, Christian Chauveau, St{é}phanie de Persis, Laure Pillier, Brahim Sarh, and G Merlo. Experimental study of oxygen enrichment effects on turbulent non-premixed swirling flames. *Energy & Fuels*, 27, 9 2013.

[63] Burguette M and Costa M. Nox emissions from unconfined swirl flames. 2006.

[64] F. Cozzi and A. Coghe. Effect of air staging on a coaxial swirled natural gas flame. *Experimental Thermal and Fluid Science*, 43:32–39, 11 2012. `doi:10.1016/j.expthermflusci.2012.04.002`.

[65] Bernard Lewis and Guenther von Elbe. Stability and structure of burner flames. *The Journal of Chemical Physics*, 11:75–97, 12 2004. `doi:10.1063/1.1723808`.

[66] Christian Thomas Eichler, Thomas Sattelmayer, and Vince Mcdonell. Flame flashback in wall boundary layers of premixed combustion systems.

[67] James R Bailey. Analysis and modelling of boundary-layer flashback processes for hydrogen-rich gas-turbine combustion, 2021.

[68] Jassin Fritz, Martin Kröner, and Thomas Sattelmayer. Flashback in a swirl burner with cylindrical premixing zone. *Journal of Engineering for Gas Turbines and Power-transactions of The Asme - J ENG GAS TURB POWER-T ASME*, 126, 10 2004. `doi:10.1115/1.1473155`.

[69] By Fares Amer Hatem and Philip J Bowen Agustin Valera-Medina. Cardiff university school of engineering flashback analysis and avoidance in swirl burners.

[70] O Tuncer, S Acharya, and J H Uhm. Dynamics, nox and flashback characteristics of confined premixed hydrogen-enriched methane flames. *International Journal of Hydrogen Energy*, 34:496–506, 2009. URL: `https://www.sciencedirect.com/science/article/pii/S0360319908011956`, `doi:https://doi.org/10.1016/j.ijhydene.2008.09.075`.

[71] Ehsan Amani, M R Akbari, and Saeid Shahpouri. Multi-objective cfd optimizations of water spray injection in gas-turbine combustors. *Fuel*, 2018. URL: `https://api.semanticscholar.org/CorpusID:103908768`.

[72] Stephen R. Turns. An introduction to combustion, concepts and applications.

[73] Michael C Drake and Richard J Blint. Calculations of nox formation pathways in propagating laminar, high pressure premixed ch4/air flames. *Combustion science and technology*, 75:261–285, 1991.

[74] Stanley Corrsin. Turbulent reacting flows . topics in applied physics, vol. 44. edited by p. a. l ibby and f. a. w illiams . springer, 1980. 243 pp. dm84. 49.60. *Journal of Fluid Mechanics*, 121:530, 10 2006. `doi:10.1017/S0022112082212031`.

[75] R W Bilger. Molecular transport effects in turbulent diffusion flames at moderate reynolds number. *AIAA Journal*, 20:962–970, 1982. `doi:10.2514/3.51154`.

[76] M. Drake, M. Lapp, C. Penny, S. Warshaw, and B. Gerhold. Measurements of temperature and concentration fluctuations in turbulent diffusion flames using pulsed raman spectroscopy. 1981.

[77] H Nicolai, L Dressler, J Janicka, and C Hasse. Assessing the importance of differential diffusion in stratified hydrogen–methane flames using extended flamelet tabulation approaches. *Physics of Fluids*, 34:085118, 8 2022. `doi:10.1063/5.0102675`.

[78] Weijie Zhang, Jinhua Wang, Wenjun Lin, Runze Mao, Hao Xia, Meng Zhang, and Zuohua Huang. Effect of differential diffusion on turbulent lean premixed hydrogen enriched flames through structure analysis. *International Journal of Hydrogen Energy*, 45:10920–10931, 4 2020. `doi:10.1016/j.ijhydene.2020.02.032`.

[79] {D}elft {H}igh {P}erformance {C}omputing {C}entre ({DHPC}). {D}elft{B}lue {S}upercomputer ({P}hase 1), 2022.

[80] Christopher Greenshields and Henry Weller. *Notes on Computational Fluid Dynamics: General Principles.* CFD Direct Ltd, 2022.

[81] H G Weller, G Tabor, H Jasak, and C Fureby. A tensorial approach to computational continuum mechanics using object-oriented techniques. *Computer in Physics*, 12:620–631, 11 1998. `doi:10.1063/1.168744`.

[82] Andrea Saltelli, Stefano Tarantola, Francesca Campolongo, and Marco Ratto. Sensitivity analysis in practice : A guide to assessing scientific models.

[83] *Variance-Based Methods*, pages 155–182. 12 2007. Wiley Online Books. URL: `https://doi.org/10.1002/9780470725184.ch4`, `doi:https://doi.org/10.1002/9780470725184.ch4`.

[84] Andrea Saltelli. Sensitivity analysis for importance assessment. *Risk Analysis*, 22:579–590, 6 2002. URL: `https://doi.org/10.1111/0272-4332.00040`, `doi:https://doi.org/10.1111/0272-4332.00040`.

[85] Francesca Pianosi, Fanny Sarrazin, and Thorsten Wagener. A matlab toolbox for global sensitivity analysis. *Environmental Modelling Software*, 70:80–85, 2015. URL: `https://www.sciencedirect.com/science/article/pii/S1364815215001188`, `doi:https://doi.org/10.1016/j.envsoft.2015.04.009`.

List of Figures

List of Tables

Acknowledgements

I would like to express my deep gratitude to Prof. Dr. Ivan Langella, for having given me the opportunity to carry out this Master thesis work, and for his expertise and guidance during this journey. I grew a lot both from a personal and technical point of view during this period spent at the TU Delft.

I'm extremely grateful to Prof. Dr. Giacomo Bruno Azzurro Persico for the possibility to develop my Master thesis work, and for his invaluable guidance and support during the thesis period.

A special thanks should also go to my daily supervisor Gioele, who led me through this work with extreme patience, and from which I learned a lot.

I am grateful to my father, for his love, encouragement and the sacrifices he made to enable my studies. I thank my brother, my grandmother and my girlfriend's family for their love and support throughout my academic journey. Special thanks also to my close friends both in Italy and in the Netherlands, in particular Giovanni, for the good and bad moments shared during the past years.

Words cannot express my gratitude to my girlfriend, Hajar, for her love and for having always been the source of my strength. Without her, I wouldn't have been able to overcome difficult moments during my academic journey.

Giacomo Abbasciano
Delft, November 2023